Stimuli Responsive Polymers in Direct-Ink-Write Additive Manufacturing

Amrita Basu

A dissertation

submitted in partial fulfillment of the

requirements for the degree of

Doctor of Philosophy

University of Washington

2020

Reading Committee:

Alshakim Nelson, Chair

Ashleigh Theberge

Matthew Golder

Program Authorized to Offer Degree:

Chemistry

University of Washington

Abstract

Stimuli Responsive Polymers in Direct-Ink-Write Additive Manufacturing

Amrita Basu

Chair of the Supervisory Committee:
Dr. Alshakim Nelson
Department of Chemistry

Additive manufacturing (AM) has revolutionized the world of manufacturing. The potential of the technology to construct any arbitrary architecture, reduce material cost and the need for an inventory is being widely explored by industry and academia alike. However, AM is currently restricted to processing polymers of "*yester-years*" which were developed to be amenable to a different set of manufacturing practices. While there has been a dramatic improvement in the hardware aspect of AM, material development still lags behind, limiting the possibilities of the technology. There has been a great effort by scientists to bring forward new materials for additive manufacturing and enable the technology to have a broad scope. One such example is stimuli-

responsive polymers which respond to environmental cues. This thesis explores the development of new stimuli responsive materials for direct-ink write additive manufacturing, based on Pluronic F127, a commercially available triblock copolymer consisting of poly(ethylene oxide) and poly(propylene oxide). In the body of work reported here, the polymer has been used in combination with aqueous and ionic liquid solvents to form hydrogels and iongels which are used in direct-ink write 3D printing. The gels are shear responsive themselves and capable of undergoing photo-induced crosslinking to form a polymer network. The rheological requirements of inks for DIW 3D printing is studied in details and several parameters are identified to screen the 3D printability inks .The development of a new 3D printing technique called gel-in-gel printing is reported which facilitates using light sensitive and mechanically weak hydrogels for fabrication of complex architecture. To add functionality to 3D printable inks, the iongel inks are then combined with a spiropyran mechanophores to enable the development of force responsive inks which exhibit an optical signal when stressed. The viscoelastic properties of the gels and the mechanical properties of the final crosslinked network are investigated and conditions necessary for mechanochemical activation of embedded mechanophores are identified. In particular, a suite of inks with highly tunable final material properties were identified which could be used to enable multi-material 3D printing of dual shape morphing objects.

TABLE OF CONTENTS

LIST OF FIGURES

LIST OF TABLES

ACKNOWLEDGEMENTS

My own efforts would have been insufficient for the completion of this body of work in this dissertation. Short of writing another thesis, it would be difficult to thank the number of people who have helped me in countless ways throughout graduate school. For you all, I am grateful.

I would like to thank my graduate advisor Dr. Alshakim Nelson for his relentless encouragement and support throughout my tenure in the Nelson lab. Al's enthusiasm for science is infectious and makes me want to push myself every day for better quality in research. I am indebted to you for the opportunities you have presented me and for helping me grow into a better scientist. I hope that someday I can be as good of a mentor as you have been to be.

I would also like to thank my committee members Dr. Ashleigh Theberge, Dr. Matt Golder and Dr. Cole DeForest and my collaborators Dr. AJ Boydston (UW Madison), Dr. Nick Boechler (UC San Diego)and Dr.Stephen Craig (Duke University), who have all contributed to my scientific upbringing and helped me navigate my research. I am grateful for the opportunity to work as a part of the IDAMMM project team and have enjoyed contributing to the research.

A huge shout out to the Nelson lab crew for great discussions in research and otherwise. For the morning coffee rituals and the usual office banter. The five years of memories will be much cherished. Rob and Abhi (our ex-postdocs), thank you for being there for us in our very first years. Being in a new research group, it was extremely helpful to have two sources of knowledge and guidance within the lab. Trevor, Dylan, Ryan, started off with me in the lab and I will have special memories of putting together shelves and instruments around the lab. I owe a huge thank you to Chris, Patrick, Claudia and Cem and Jenn, Fang and Eva for being great colleagues and even better friends. You all have helped me improve my work, think critically, and shed new perspectives on my research whenever I needed them.

I owe my Seattle friends and family the most genuine thank you, especially Soumyadytui, Camille, Zhilmil, Amita and Sayantan, Avijit, Sudipto, Bindita, Rahul, Anindita and Navonil.

Graduate school would not have been the same without the weekend parties, dinners, and hiking adventures. You made the transition to a new continent away from my family so much better and I am truly grateful for the community I have found here. Special shoutout to Todd Anderson. Thank you for teaching me life skills like driving and everything about the USA. I would have a much harder time adjusting to life here without your help.

My friends from India have been important in my life. A huge shout out to Srjia, Rajashi, Sanchari Sohini, Arani, Samik, Chandrima, and Anwesha for staying in touch with me throughout the distance and time zone differences.

Finally, I would like to thank the people closest to my heart: my *mamma* (mother), for being the greatest mother and friend. She has selflessly encouraged me to explore new directions in life and she continues being the reason behind all achievements in life. Thank you *Didi* (elder sister and bestest friend) for everything we share, which is impossible to put into words, and *Saurav da* (brother-in-law) for your love, sunny disposition, and positive outlook. You all make up the greatest family one can ask for. Thank you for your continued love, support, and fun conversations. Last but not the least, Thank You Amartya for moving to a different continent to start graduate school together in the USA. You continue to make me a better person every day. I have loved our many adventures together and I look forward to a lot more in the years to come. Thank you, for your companionship.

DEDICATION

To my mother Dr. Atreyee Basu and
To the memory of my father Dr. Sumanta Basu

You taught me all about dream
And how to catch them.

"The secret of getting ahead is getting started. The secret of getting started is breaking your complex overwhelming tasks into small manageable tasks and getting started on the first one. "

Mark Twain

CHAPTER 1: **INTRODUCTION**

1.1 INTRODUCTION TO ADDITIVE MANUFACTURING:

Additive manufacturing (AM), also called 3D printing (3DP) is a relatively young industry which has emerged in the last 40 years as an advanced fabrication technique. The technology was first commercialized in the 1980s based on the UV light-assisted curing of liquid photopolymer resins by Charles Hull who later founded 3D Systems Inc, one of the most prolific 3D printing companies[1]. It was originally poised to be used as a rapid prototyping tool for manufacturers to assess designs quickly, however, AM has now reached the ability to manufacture end-use products[2]. Unlike traditional manufacturing like injection molding or CNC milling, AM constructs objects through layer-by-layer deposition of materials. This layer-by-layer addition allows for the creation of objects directly from a CAD file, removing surplus steps such as making molds. Currently, AM is a rapidly advancing field, having received significant attention from both academia and industry, and is predicted to reach $36 billion dollars in revenue by 2024[3]. AM has grown significantly in popularity due to its ability to build complex lattices and geometries, reduce material usage, and allow the creation of graded and multi materials[4-6]. Advances, both in materials and hardware development in additive manufacturing has led to its widespread application beyond rapid prototyping in expanding fields like tissue engineering,[7] patient specific implants,[8] and automotive and aerospace engineering.[9] The SARS-COV-2 pandemic of 2020 has highlighted many of the benefits of AM including on-demand supply of testing kits and production of personal protective[10,11] and medical equipment.[12]

All 3D printing (AM) methods involve: 1) designing a digital model; 2) single layer material addition; 3) post-processing. The digital model can be designed using a computer aided design (CAD) software or a 3D scanner which scans object features and creates a digital model. This is converted into a computer numerical programming language called GCODE using a "slicer" which controls the printer actions. The printing process can take anywhere between hours to days depending on the size and complexity of the model being created. After printing, the object is post-processed by exposure to thermal or photochemical irradiation in order to cure, or remove unbound resin or powder from, the body. After curing, the final construct can be used for its desired application.

According to American Society of Testing and Materials (ASTM), there are six different kinds of AM techniques available to be used with different materials as highlighted in Table 1.1.[13] It should be noted that several of the techniques mentioned in Table 1.1, including vat photopolymerization and powder-bed sintering, construct objects out of a vat which contains the material. This yields finished products which are homogenous in their composition within a single build. On the other hand, material extrusion techniques are very versatile platforms which can enable rapid switching between nozzles to facilitate freeform and multi-material 3D printed constructs. Direct-ink write (DIW) systems fall under the category of extrusion-based printing which can produce multi-material objects[14]. DIW is the most adaptable of the 3D printing techniques and can be used to process a wide variety of materials including polymers[15], ceramics[i], and composites[17,18]. The process takes advantage of the viscoelastic properties of materials such that the ink flows from a nozzle when pressure is applied using a pneumatic or screw driven system but can retain its shape once extruded[19]. DIW 3DP enables the development of new materials with

a breadth of functionality in them and the fabrication of spatially resolved multi-materials 3D printed objects, since different inks can be deposited in a pattern-wise manner. After printing, a variety of techniques like UV initiated free radical photopolymerization[20], hardening of ceramic pastes[21] due to drying or deposition of temperature responsive gels onto heated plates[22] have been demonstrated to initiate curing of precursor material. Another technique for curing inks is extruding the ink into a second support bath.[23]

1.2 STIMULI RESPONSIVE POLYMERS FOR DIW 3D PRINTING:

With the advent of digital technologies in AM, there has been a parallel increase in research which would improve the material platforms offered for 3D printers, with a focus on developing "smart" materials which can undergo a change in response to environmental cues. Smart materials can respond to environmental triggers like temperature[24], pH[25], light[24] and mechanical force[26,27] and exhibit a measurable response. The stimuli response of polymeric systems can either be inherent to the system or due to the presence of additives. The combination of smart materials with the freedom of geometry architecture afforded by extrusion-based AM makes it amenable to a range of application including soft robotics[28,29] biomimetic 4D printing[ii] and tissue engineering.[31,32]

There are two general strategies for 3D printing stimuli-responsive materials with DIW: in the first approach, low viscosity inks are deposited from a nozzle followed by immediate curing through a chemical, photochemical, or non-covalent method. Calcium alginate[33] or gelatin methacrylate[21] have been printed using these techniques, often with poor resolution. Alternatively, shear-thinning gels, similar to F127 based hydrogels, can be used which are extruded in layers

until the full structure is 3D printed followed by curing. Pluronic F127 is a commercially available triblock copolymer consisting of poly(*ethylene oxide*)-b-poly(*propylene oxide*)-b-poly(*ethylene oxide*) (PEO-b-PPO-b-PEO). At low concentrations, the polymer chains aggregate into spherical micelles with an inner core formed from the hydrophobic PPO units and an outer shell formed by the hydrophilic PEG blocks. At higher concentrations (~20 wt%) of polymer this leads to the micelles packing together in a body-centered cubic fashion to form a free-standing hydrogel as shown in Figure 1.1. The gel is temperature responsive: at low temperature, the PEO-PPO-PEO blocks are individually solvated as unimers and it behaves like a low viscosity liquid. At room temperature however, the unimers form micelles resulting in the formation of a shear thinning gel. It is to be noted that the enthalpy of micellization (ΔH) is positive, indicating that the conversion of unimers to micelles is unfavored. However, the free energy of the reaction (ΔG) is negative, driven by the entropic cost.[34] The packing shown by the micelles makes them able to slide past each other in the presence of a shear force, thus making it an extrudable material and an excellent polymer for DIW 3D printing[35]. Functionalizing the chain-ends with acrylates or methacrylates enables free radical polymerization to crosslink the micelles and afford a mechanically robust structure after 3D printing.

F127 has also been reported to dissolve in ionic liquids to form “iongels”. Ionic liquids are salts in which the ions cannot crystallize due to steric hinderance, making them a liquid below 100°C or even at room temperature. They are being explored within the context of DIW printing due to their highly conductive nature[36], thermal stability, and excellent tunability of mechanical properties from a tough thermoplastic to hydrogel like soft material.[37]

1.3 INTRODUCTION TO POLYMER MECHANOCHEMISTRY

Polymers, owing to their unique chain-like structures have a wide range of unique mechanical properties like elasticity, toughness and processability which makes them highly desirable for various applications in consumer products. These molecular chains can respond to the external mechanical perturbation applied on polymer materials, resulting in the scission or reconfiguration of the bonds. Historically, the combination of polymers and force results in undesirable bond cleavage, degradation of polymer materials or a compromise in their mechanical properties. However, the discovery of *mechanophores* and polymer mechanochemistry have successfully redirected the concept of mechanical energy from "destructive" to "productive".

The field of polymer mechanochemistry is an interdisciplinary success story with origins dating back to the early 1900s. A seminal report by Staudinger in 1934 described the reduction in molecular weight of polystyrene subjected to high speed ball milling or turbid flow, and ever since, bolstered by periodic infusions of creativity, the field has grown in alignment with advances in polymer synthesis, analytical techniques, and computational capabilities.[38] Now, polymer mechanochemistry has evolved into a high-precision tool for exacting molecular reconfiguration in response to macroscopic influences, and a design opportunity that attracts and inspires innovative approaches to responsive materials.

A critical moment for the field was a seminal report by Moore et al., which showed a mechanochemical reaction in violation of the fundamental Woodward-Hoffmann pericyclic selection rule.[39] It was the first example of the concept that the potential energy surfaces for mechanochemical reactions are fundamentally altered from those of the same reaction under, for comparison, solely thermal control. Depending on the location of, and the amount of force applied

to a mechanophore, the reaction pathway can be modified in ways that are not accessible from other energy inputs.[40] Investigation of other fundamentals of polymer mechanochemistry ushered in an era of discovery that helped establish a series of guiding principles.

Mechanophores can be grouped according to their responses as illustrated by the graphic in Figure 1.2. There is a plethora of mechanophores which have been developed, capable of self-strengthening[41], changing the Tg of materials[42] and releasing small molecules[43]. In this study, mechanophores showing an optical response (mechanochromophore) will be emphasized.

Mechanochromophores: Mechanochromophores change color upon application of mechanical stimulus, either by direct manipulation of chromophores as a result of a mechanochemical reaction, or by energy transfer, to produce optical responses indirectly. The stress (or strain) sensitivity and macroscopically observable visual output motivates development of mechanochromophores as damage sensors in polymeric materials and composites. For example, a color change in the material enables quick visual assessment of regions under high stress or that are experiencing high strain, such that they can be decommissioned and/or repaired before complete failure of the device. Similarly, load history and duty cycles can be logged by the material itself. A number of these mechanochromophores show color responses via the breaking of a labile bond followed by increase in conjugation or emission of light from the relaxation of intermediates. Depending on the reaction pathway, the optical signal can be either reversible or irreversible, offering a rich palette of functions that can be coupled to a comparably rich range of materials questions and applications.

Moore, Sottos, and co-workers made a major contribution in the field of mechanochemistry when they successfully incorporated spiropyran (SP) as a mechanochromophore within a

polymer.[44] They showed that tension applied through the material triggered a visual change from colorless to a pink, blue, or purple color (depending on the polarity of the environment) accompanied by a in photoluminescent response. The photophysical changes are the result of the mechanochemical electrocyclic 6π ring opening of the SP to the colored merocyanine form (Figure 1.3(a)). Reversibility results in gradual fading of the visual color and photoluminescence as the merocyanine form reverts to the SP. The timescale at which color fades in the SP derivatives reported to date ranges from "instantaneous" (ms or faster) to tens of minutes, depending on the environment and structural features of the SP. The reversion is accommodated by relaxation of tension within an activated polymer segment, and therefore SP's molecular response can be used to study a material's mechanical and rheological behavior. Quantification of color intensity upon activation and reversion of SP, whether absolute or relative, can be used to assess load history. The color changes are often readily observed by the naked eye, offering an easy visual cue of the early stages of mechanical damage or a critical strain being reached, but it can also be quantified by standard spectroscopic techniques or digital image analysis (including, in the case of fluorescence, high resolution confocal microscopy).[45,46]

The optical characteristics and ease of functionalization quickly appealed to several researchers, and SP has been used as a visual indicator of mechanical force in solution as well as a large number of matrices. For example, SP has been covalently incorporated into glassy polymers,[47] elastomers,[48] latexes,[49] and hydrogels,[50] each resulting in mechanochromic behavior. SP was also successfully incorporated into thermoplastic polycaprolactone (PCL)[51] and elastomeric silicone resins[52] to be used in the additive manufacturing of smart materials and strain sensors. Moreover, SP can be used in a range of soft device applications where reversible and

repeatable signaling is desired.[53,54] Most of the reversible mechanochromophores that have been reported to date are, like SP, adapted from known photochromic molecules. With this foundational knowledge, design scaffolds have expanded and become more deliberate. For example, mechanochromophores based upon naphthopyran activate (and de-activate) more slowly than their SP counterparts.[55] More complex molecular designs promise more sophisticated mechanochromic responses, such as a bis(naphthopyran) (BNP) mechanophore developed by Robb and co-workers for multicolored gradient response.[56] Sequential color changes are highly appealing targets that could enable, for example, high precision mechanochromic strain mapping to a color gradient rather than current approaches based on intensity. [46,47]

In addition to potential applications for strain mapping, the BNP mechanochromophore highlights an important fundamental aspect mentioned previously: the mechanical reaction pathway can be unique. The BNP system starts with each of the pyran rings in a "closed" configuration (denoted here as $BNP_{C\text{-}C}$). With photochemical activation, each pyran ring opens to give the doubly activated system ($BNP_{O\text{-}O}$) at the exclusion of the mixed open/closed intermediate $BNP_{O\text{-}C}$. Mechanochemically, the process unfolds in a stepwise manner, giving first an accumulation of $BNP_{O\text{-}C}$ at relative low strain, followed by high strain activation of the second pyran ring in each BNP to give $BNP_{O\text{-}O}$. The authors report a dynamic equilibrium between the $BNP_{O\text{-}O}$ and $BNP_{O\text{-}C}$ states that is force dependent, and as the applied load increases, a greater quantity of $BNP_{O\text{-}O}$ is generated.

Mechanochromophores with irreversible responses. The reversible response of SP and other photoswitch-based mechanochromophores is complemented by a number of irreversible, single-activation mechanophores, which offer additional sensing and reporting abilities. These

irreversible responses may be either transient or permanent, offering different advantages and opportunities. Transient response was first reported in 2012 by Sijbesma and co-workers reported that mechanical scission of the four membered ring in a bis-adamantyl dioxetane generates the nearly instantaneous (sub-ms) emission of visible light in either solution (via ultrasound) or bulk materials (via tensile load) (Figure 1.3(b)).[57] Mechanical scission of the dioxetane mechanophore gives two carbonyls, one of which is in an electronic excited state. The excited state species can relax to its ground state by emitting blue light (420 nm) or via energy transfer to an acceptor molecule. By varying the choice of acceptor, the emitted light can be tuned to other wavelengths in the visible spectrum. The dioxetane mechanophore can be used for real time monitoring of stress and failure in a polymer material due to its high temporal accuracy; photons are emitted only at the instant that mechanophore scission occurs. In addition, luminescence occurs without an external light source -- the energy required for photon emission is provided entirely by the mechanical event, meaning that it is relatively easy to employ conditions with negligible background signal and therefore achieve high sensitivity that can be used to detect small numbers of molecular events, despite the fact that, on average, just under a single photon is emitted per mechanophore activation. This contrasts to the reversible mechanochromophores described above, in which sensitivity is limited by background from an incident light source, the extinction coefficient (and, in the case of fluorescence, the quantum efficiency) of the activated chromophore, and often the presence of small equilibrium amounts of the "open" form of the probe. As a result of its sensitivity, the dioxetane mechanophore has been used to probe bond scission events with high spatiotemporal resolution as a function of polymer state (e.g., plastic vs. rubbery vs. glassy) and polymer network architecture (e.g., single vs. multi-networks).

Other irreversible mechanochromophores lead to an effectively permanent "turn on" optical signal that is limited primarily by photobleaching of the activated chromo- or fluorophore. For example, Boydston[58] and Bielawski[59] independently reported that under sonication the mechanically forced cyclo-reversion reaction of an anthracene-maleimide (AnMal) adduct leads to the liberation of an anthracene fluorophore that is capable of a blue fluorescent response. This and similar designs offer capabilities that complement the previously discussed mechanochromophores. For example, reversible systems such as SP will rapidly lose color once a chain breaks, whereas here chain scission is directly responsible for the optical response. In addition, the chromic response of the AnMal system accumulates over time; unlike the dioxetane system, chain scission can be assessed at any point following a putative mechanical event, rather than requiring constant monitoring. The AnMal mechanophore, for example, was used by the Moore group in 2016 to probe molecular activation at the heterogeneous interface between an organic poly(methylacrylate) (PMA) chain and inorganic silica nanoparticles.[60] The AnMal was placed through synthesis at the organic-inorganic junction to test the hypothesis that this is the site of stress concentration and preferential scission. When subjected to forces applied by ultrasonication, the predicted liberation of PMA-terminated anthracene was observed.

In a similar example, anthracene derivatives were used by the Chan Moon Chung group as crack sensors that could be monitored via fluorescence spectroscopy.[61] Anthraldehyde (AA) was dimerized via a photochemical 4π-4π cycloaddition to form cyclooctane adducts (di-AA) that served as the mechanophore (Figure 1.3(c)). It was hypothesized that the same adduct could undergo mechanochemical cycloreversion to regenerate the anthraldehyde moiety accompanied by a change in fluorescence properties. When incorporated in a crosslinked matrix by reacting di-

AA with poly(vinyl alcohol) to form acetal linkages, it was seen that the resulting hard polymer, poly-AA, could be ground mechanically to cleave the adduct. This was confirmed via fluorescence spectroscopy: when excited at 380nm, the ground polymer had a significant increase in fluorescence at 500-600nm compared to the native polymer due to the presence of free anthracene groups. More recently, an anthracene dimer based mechanochromophore was used by Weng and coworkers to track the crack propagation in a multi-network elastomer.[62]

Improvements in mechanochromophore design: The enhancement of mechanochromophores in materials applications continues through improvements in a number of molecular performance metrics. For example, fluorescence quantum yield, optical reversibility, and the lifespan of optical "on" states each contribute to the utility of a mechanochromophore, independent of the mechanical activity. The AnMal system, for example, has recently been enhanced by Sijbesma et al. through the use of π-extended anthracene chromophores that improve the otherwise low quantum efficiency of the liberated anthracene by over two orders of magnitude.[63] The system offered other advantages as well: bathochromic shifts in the emission spectra that allowed access to a wider range of detection wavelengths, and low oxygen sensitivity that reduced fluorescence quenching. When incorporated within various polyacrylates, the π-extended AnMal is activated in both solutions and bulk solids and therefore offers promise for irreversible, durable signaling of mechanically induced scission events in polymeric materials.

Beyond improvements in individual mechanophore design, additional opportunities exist through the combination of mechanochromophores. As mentioned in the context of BNP, for example, there is a growing interest in sequential, multi-color responses. Otsuka and co-workers have shown that multiple colored responses can be achieved in a single material via the careful

combination of two mechanophores: diarylbibenzyl furanone (DABBF) and napthopyran (NP).[64] The two mechanochromophores have different mechanisms of activation: DABBF can be cleaved to produce blue arylbenzylfuranone radicals, whereas napthopyran can isomerize to an orange merocyanine dye. When incorporated into a polymer-silica composite matrix, gentle kneading of the material results in the matrix turning from its initial yellow state to blue. On further kneading, the color turns green due to the activation of the NP. The color can be switched back to blue by exposing it to the white light that triggers the photochemical isomerization of the NP. Together with the control of individual mechanochromophore color available through molecular designs such as the π-extended anthracenes, similar multi-component systems are likely to lead to the development of multimodal damage sensors with an even larger palette of available colors.

A final, emerging area of activity in the field is aimed at the external regulation of mechanical response. Otsuka and co-workers reported the first example of regulation of mechanochemical activation via photochemical reaction[64] (Figure 1.3(d)). Diarylethene Diels-Alder (DAE/DA) adducts can undergo reversible photochemical cyclization at the diarylethene motif and so regulate the cycloreversion of DAE/DA adducts. The authors hypothesized that when a DAE/DA adduct is incorporated within a polymer chain, the open form of the adduct is more likely to undergo chain scission via retro-DA reaction than the closed form. When incorporated in the middle of a PMA chain, the DAE_{open}/DA chain showed scission under sonication. The retro DA products, furan and maleimide groups were confirmed via size exclusion chromatography and NMR spectroscopy. On the other hand, polymers with DAE/DA at the chain ends, or without DAE/DA altogether, did not show activation. On exploring the mechanochromic property of the closed form, the rate of chain scission was found to be significantly lower than the open form. Similarly, the Robb group reported

using a DA adduct between cyclopentadiene and maleimide in the center of a PMA chain to mechanochemically regulate a photoswitching reaction.[65] When subjected to ultrasonication, the adduct can be broken via retro Diels-Alder reaction to afford a DAE with an optical response. When subjected to UV irradiation, the original DA adduct does not have any photoswitching properties, however, the DAE could be irradiated with UV light to its open form having a red color. Results of the mechanochemical degradation of the initial polymer and subsequent changes in color were confirmed via GPC and UV-Vis spectroscopy.

1.4 Polymer Mechanochemistry and 3D printing:

The fields of AM and polymer mechanochemistry have, individually, seen rapid advances and prolific research, however the merge between the two have been relatively unexplored. This can be attributed to the mechanophores undergoing irreversible transformation under printing conditions. The Boydston group reported SP incorporation within a polycaprolactone matrix by filamentizing the polymer and printing using an FDM 3D printer[28]. PCL was chosen due to its low melting and glass transition temperature (Tg~60°C) which afforded milder printing conditions. This work highlighted the key advantages of integrating AM with mechanochromic materials which provided an excellent spatial control over deposition patterns and regions. However, PCL being a thermoplastic was irreversibly deformed after stretching and could not be re-used. Additionally, the Boydston group reported the incorporation of an oxonorbornadiene mechanophore within a hydroxy ethyl acrylate resin which could be 3D printed using vat photopolymerization techniques[66]. It was observed that upon compression, the soft elastomeric sample could undergo “flex” activation to release a small molecule. The molecule was extracted and quantified with GC-MS to determine percent activation of mechanophore as a function of

strain. In this case, the polymer material after compression could have full shape recovery, however, the mechanophore activation had to be quantified by GC-MS and was not optically detectable. As mechanochemistry is being studied at greater depth, there is a huge potential for merging the field with AM in order to enhance the chemo-mechanical responses in materials. AM can also provide a platform for more complex geometry designs and enable rapid iterative design realization and optimization. This thesis focuses on the development of a series of inks for DIW 3D printing with SP as the mechanchromophore of choice. Two different platforms based on silicone-based elastomers and iongels with tunable mechanical properties are discussed herein.

1.5 REFERENCES

1. Hull, C. W. Apparatus for Production of Three-Dimensional Objects by Stereolithography. US4575330A, March 11, 1986.
2. Industrial Applications of 3D Printing: The Ultimate Guide. *AMFG*.
3. McCue, T. J. Significant 3D Printing Forecast Surges To $35.6 Billion https://www.forbes.com/sites/tjmccue/2019/03/27/wohlers-report-2019-forecasts-35-6-billion-in-3d-printing-industry-growth-by-2024/#39fd3efb7d8a (accessed May 13, 2020).
4. Gao, W.; Zhang, Y.; Ramanujan, D.; Ramani, K.; Chen, Y.; Williams, C. B.; Wang, C. C. L.; Shin, Y. C.; Zhang, S.; Zavattieri, P. D. The Status, Challenges, and Future of Additive Manufacturing in Engineering. Computer-Aided Design 2015, 69, 65–89.
5. Hardin, J. O.; Ober, T. J.; Valentine, A. D.; Lewis, J. A. Microfluidic Printheads for Multimaterial 3D Printing of Viscoelastic Inks. *Advanced Materials* **2015**, *27*, 3279–3284.
6. Skylar-Scott, M. A.; Mueller, J.; Visser, C. W.; Lewis, J. A. Voxelated Soft Matter via Multimaterial Multinozzle 3D Printing. *Nature* **2019**, *575*, 330–335.
7. Gleadall, A.; Visscher, D.; Yang, J.; Thomas, D.; Segal, J. Review of Additive Manufactured Tissue Engineering Scaffolds: Relationship between Geometry and Performance. *BURNS TRAUMA* **2018**, *6*.
8. Youssef, A.; Hollister, S. J.; Dalton, P. D. Additive Manufacturing of Polymer Melts for Implantable Medical Devices and Scaffolds. *Biofabrication* **2017**, *9*, 012002.
9. Uriondo, A.; Esperon-Miguez, M.; Perinpanayagam, S. The Present and Future of Additive Manufacturing in the Aerospace Sector: A Review of Important Aspects: *Proceedings of the Institution of Mechanical Engineers, Part G: Journal of Aerospace Engineering* **2015**.
10. Callahan, C. J.; Lee, R.; Zulauf, K.; Tamburello, L.; Smith, K. P.; Previtera, J.; Cheng, A.; Green, A.; Azim, A. A.; Yano, A.; et al. Open Development and Clinical Validation of Multiple 3D-Printed Sample-Collection Swabs: Rapid Resolution of a Critical COVID-19 Testing Bottleneck. *medRxiv* **2020**, 2020.04.14.20065094
11. Celik, H. K.; Kose, O.; Ulmeanu, M.-E.; Rennie, A. E. W.; Abram, T. N.; Akinci, I. Design and Additive Manufacturing of Medical Face Shield for Healthcare Workers Battling Coronavirus (COVID-19). International Journal of Bioprinting 2020, 6.
12. Callahan, C. J.; Lee, R.; Zulauf, K.; Tamburello, L.; Smith, K. P.; Previtera, J.; Cheng, A.; Green, A.; Azim, A. A.; Yano, A.; et al. Open Development and Clinical Validation of Multiple 3D-Printed Sample-Collection Swabs: Rapid Resolution of a Critical COVID-19 Testing Bottleneck. medRxiv 2020, 2020.04.14.20065094.
13. Hybrid Manufacturing Resources http://www.hybridmanutech.com/resources.html (accessed Jul 14, 2020).
14. Hon, K. K. B.; Li, L.; Hutchings, I. M. Direct Writing Technology—Advances and Developments. *CIRP Annals* **2008**, *57*, 601–620.
15. Li, L.; Lin, Q.; Tang, M.; Duncan, A. J. E.; Ke, C. Advanced Polymer Designs for Direct-Ink-Write 3D Printing. *Chemistry – A European Journal* **2019**, *25*, 10768–10781.
16. Lewis, J. A.; Smay, J. E.; Stuecker, J.; Cesarano, J. Direct Ink Writing of Three-Dimensional Ceramic Structures. *Journal of the American Ceramic Society* **2006**, *89*, 3599–3609.

17. Valino, A. D.; Dizon, J. R. C.; Espera, A. H.; Chen, Q.; Messman, J.; Advincula, R. C. Advances in 3D Printing of Thermoplastic Polymer Composites and Nanocomposites. *Progress in Polymer Science* **2019**, *98*, 101162.
18. Kim, Y.; Yuk, H.; Zhao, R.; Chester, S. A.; Zhao, X. Printing Ferromagnetic Domains for Untethered Fast-Transforming Soft Materials. *Nature* **2018**, *558*, 274–279.
19. Lewis, J. A. Direct Ink Writing of 3D Functional Materials. *Adv. Funct. Mater.* **2006**, *16*, 2193–2204.
20. Barry, R. A.; Shepherd, R. F.; Hanson, J. N.; Nuzzo, R. G.; Wiltzius, P.; Lewis, J. A. Direct-Write Assembly of 3D Hydrogel Scaffolds for Guided Cell Growth. *Adv. Mater.* **2009**, *21*, 2407–2410.
21. Ahn, B. Y.; Shoji, D.; Hansen, C. J.; Hong, E.; Dunand, D. C.; Lewis, J. A. Printed Origami Structures. *Advanced Materials* **2010**, *22*, 2251–2254.
22. Yin, J.; Yan, M.; Wang, Y.; Fu, J.; Suo, H. 3D Bioprinting of Low-Concentration Cell-Laden Gelatin Methacrylate (GelMA) Bioinks with a Two-Step Cross-Linking Strategy. *ACS Appl. Mater. Interfaces* **2018**, *10*, 6849–6857.
23. Hinton, T. J.; Jallerat, Q.; Palchesko, R. N.; Park, J. H.; Grodzicki, M. S.; Shue, H.-J.; Ramadan, M. H.; Hudson, A. R.; Feinberg, A. W. Three-Dimensional Printing of Complex Biological Structures by Freeform Reversible Embedding of Suspended Hydrogels. *Science Advances* **2015**, *1*, e1500758.
24. D. Jochum, F.; Theato, P. Temperature- and Light-Responsive Smart Polymer Materials. *Chemical Society Reviews* **2013**, *42*, 7468–7483.
25. Du, J.-Z.; Du, X.-J.; Mao, C.-Q.; Wang, J. Tailor-Made Dual PH-Sensitive Polymer–Doxorubicin Nanoparticles for Efficient Anticancer Drug Delivery. *J. Am. Chem. Soc.* **2011**, *133*, 17560–17563.
26. Li, J.; Nagamani, C.; Moore, J. S. Polymer Mechanochemistry: From Destructive to Productive. *Acc. Chem. Res.* **2015**, *48*, 2181–2190.
27. Peterson, G. I.; Larsen, M. B.; Ganter, M. A.; Storti, D. W.; Boydston, A. J. 3D-Printed Mechanochromic Materials. *ACS Appl. Mater. Interfaces* **2015**, *7*, 577–583.
28. Wallin, T. J.; Pikul, J.; Shepherd, R. F. 3D Printing of Soft Robotic Systems. *Nature Reviews Materials* **2018**, *3*, 84–100.
29. Kotikian, A.; McMahan, C.; Davidson, E. C.; Muhammad, J. M.; Weeks, R. D.; Daraio, C.; Lewis, J. A. Untethered Soft Robotic Matter with Passive Control of Shape Morphing and Propulsion. *Science Robotics* **2019**, *4*.
30. Sydney Gladman, A.; Matsumoto, E. A.; Nuzzo, R. G.; Mahadevan, L.; Lewis, J. A. Biomimetic 4D Printing. *Nature Materials* **2016**, *15*, 413–418.
31. Hinton, T. J.; Jallerat, Q.; Palchesko, R. N.; Park, J. H.; Grodzicki, M. S.; Shue, H.-J.; Ramadan, M. H.; Hudson, A. R.; Feinberg, A. W. Three-Dimensional Printing of Complex Biological Structures by Freeform Reversible Embedding of Suspended Hydrogels. *Science Advances* **2015**, *1*, e1500758.
32. Hospodiuk, M.; Dey, M.; Sosnoski, D.; Ozbolat, I. T. The Bioink: A Comprehensive Review on Bioprintable Materials. *Biotechnology Advances* **2017**, *35*, 217–239.
33. He, Y.; Yang, F.; Zhao, H.; Gao, Q.; Xia, B.; Fu, J. Research on the Printability of Hydrogels in 3D Bioprinting. *Scientific Reports* **2016**, *6*, 29977.

34. Poly(Ethylene Oxide)□poly(Propylene Oxide)□poly(Ethylene Oxide) Block Copolymer Surfactants in Aqueous Solutions and at Interfaces: Thermodynamics, Structure, Dynamics, and Modeling. *Colloids and Surfaces A: Physicochemical and Engineering Aspects* **1995**, *96*, 1–46.
35. King, S. M.; Heenan, R. K.; Cloke, V. M.; Washington, C. Neutron Scattering from a Poly(Oxyethylene)−Poly(Oxypropylene)−Poly(Oxyethylene) Copolymer in Dilute Aqueous Solution under Shear Flow. *Macromolecules* **1997**, *30*, 6215–6222.
36. Wong, J.; Gong, A. T.; Defnet, P. A.; Meabe, L.; Beauchamp, B.; Sweet, R. M.; Sardon, H.; Cobb, C. L.; Nelson, A. 3D Printing Ionogel Auxetic Frameworks for Stretchable Sensors. *Advanced Materials Technologies* **2019**, *4*, 1900452.
37. Wong, J.; Basu, A.; Wende, M.; Boechler, N.; Nelson, A. Mechano-Activated Objects with Multidirectional Shape Morphing Programmed via 3D Printing. *ACS Appl. Polym. Mater.* **2020**, *2*, 2504–2508.
38. Staudinger, H. & Heuer, W. Uber hochpolymere Ver- bindungen, 93. Mitteil. 1) : Uber das Zerreinen der Faden-Molekule des Poly-styrols. *Ber. Dtsch. Chem. Ges* 1934,1159–1164.
39. Hickenboth, C. R.; Moore, J. S.; White, S. R.; Sottos, N. R.; Baudry, J.; Wilson, S. R. Biasing Reaction Pathways with Mechanical Force. *Nature* **2007**, *446*, 423–427.
40. Ong, M. T.; Leiding, J.; Tao, H.; Virshup, A. M.; Martínez, T. J. First Principles Dynamics and Minimum Energy Pathways for Mechanochemical Ring Opening of Cyclobutene. *J. Am. Chem. Soc.* **2009**, *131*, 6377–6379.
41. Ramirez, A. L. B.; Kean, Z. S.; Orlicki, J. A.; Champhekar, M.; Elsakr, S. M.; Krause, W. E.; Craig, S. L. Mechanochemical Strengthening of a Synthetic Polymer in Response to Typically Destructive Shear Forces. *Nature Chemistry* **2013**, *5*, 757–761.
42. Ramirez, A. L. B. *et al.* Microstructure of copolymers formed by the reagentless, mechanochemical remodeling of homopolymers via pulsed ultrasound. *ACS Macro Lett.* **2012**,1, 23–27.
43. Larsen, M. B.; Boydston, A. J. "Flex-Activated" Mechanophores: Using Polymer Mechanochemistry To Direct Bond Bending Activation. *J. Am. Chem. Soc.* **2013**, *135*, 8189–8192.
44. Potisek, S. L.; Davis, D. A.; Sottos, N. R.; White, S. R.; Moore, J. S. Mechanophore-Linked Addition Polymers. *J. Am. Chem. Soc.* **2007**, *129*, 13808–13809.
45. Chen, Y., Yeh, C. J., Qi, Y., Long, R. & Creton, C. From force-responsive molecules to quantifying and mapping stresses in soft materials. *Sci. Adv.* 6, **2020** eaaz5093.
46. Wang, Q., Gossweiler, G. R., Craig, S. L. & Zhao, X. Cephalopod-inspired design of electro mechano-chemically responsive elastomers for on-demand fluorescent patterning. *Nat. Commun.* **2014**,5, 4899 ().
47. Davis, D. A. *et al.* Force-induced activation of covalent bonds in mechanoresponsive polymeric materials. *Nature.* **2009** 459, 68–72.
48. Zhang, H. *et al.* Spiropyran as a mechanochromic probe in dual cross-linked elastomers. *Macromolecules* **2014,**47, 6783–6790.
49. Li, M., Liu, W., Zhang, Q. & Zhu, S. Mechanical Force Sensitive Acrylic Latex Coating. *ACS Appl. Mater. Interfaces* **2017**,9, 15156–15163.

50. Chen, H., Yang, F., Chen, Q. & Zheng, J. A Novel Design of Multi-Mechanoresponsive and Mechanically Strong Hydrogels. *Adv. Mater.* **2017** 29, 1606900.
51. Peterson, G. I., Larsen, M. B., Ganter, M. A., Storti, D. W. & Boydston, A. J. 3D-printed mechanochromic materials. *ACS Appl. Mater. Interfaces* **2015*7***, 577–583.
52. [1] Rohde, R. C. *et al.* Mechanochromic composite elastomers for additive manufacturing and low strain mechanophore activation. *Polym. Chem.* **2019**,10, 5985–5991.
53. Gossweiler, G. R. *et al.* Mechanochemically Active Soft Robots. *ACS Appl. Mater. Interfaces* **2015**,7, 22431–22435.
54. Barbee, M. H. *et al.* Mechanochromic Stretchable Electronics. *ACS Appl. Mater. Interfaces* **2018,**10, 29918–29924.
55. Robb, M. J. *et al.* Regioisomer-Specific Mechanochromism of Naphthopyran in Polymeric Materials. *J. Am. Chem. Soc.* **2016**,138, 12328–12331.
56. McFadden, M. E. & Robb, M. J. Force-Dependent Multicolor Mechanochromism from a Single Mechanophore. *J. Am. Chem. Soc.* 2**019**,141, 11388–11392.
57. Chen, Y. *et al.* Mechanically induced chemiluminescence from polymers incorporating a 1,2-dioxetane unit in the main chain. **2012** *Nat. Chem.* 4, 559–562.
58. Church, D. C., Peterson, G. I. & Boydston, A. J. Comparison of mechanochemical chain scission rates for linear versus three-arm star polymers in strong acoustic fields. *ACS Macro Lett.***2014**, 3, 648–651 (2014).
59. Brantley, J. N., Wiggins, K. M. & Bielawski, C. W. Polymer mechanochemistry: The design and study of mechanophores. *Polym. Int.* **2013**, 62, 2–12.
60. Li, J. *et al.* Mechanophore activation at heterointerfaces. *J. Am. Chem. Soc.* **2014**,136, 15925–15928.
61. Song, Y.-K.; Lee, K.-H.; Hong, W.-S.; Cho, S.-Y.; Yu, H.-C.; Chung, C.-M. Fluorescence Sensing of Microcracks Based on Cycloreversion of a Dimeric Anthracene Moiety. *J. Mater. Chem.* **2011**, *22*, 1380–1386.
62. Zhang, H.; Zeng, D.; Pan, Y.; Chen, Y.; Ruan, Y.; Xu, Y.; Boulatov, R.; Creton, C.; Weng, W. Mechanochromism and Optical Remodeling of Multi-Network Elastomers Containing Anthracene Dimers. *Chem. Sci.* **2019**, *10*, 8367–8373.
63. Göstl, R.; Sijbesma, R. P. π-Extended Anthracenes as Sensitive Probes for Mechanical Stress. *Chem. Sci.* **2015**, *7*, 370–375.
64. Kosuge, T.; Zhu, X.; Lau, V. M.; Aoki, D.; Martinez, T. J.; Moore, J. S.; Otsuka, H. Multicolor Mechanochromism of a Polymer/Silica Composite with Dual Distinct Mechanophores. *J. Am. Chem. Soc.* **2019**, *141*, 1898–1902.
65. Hu, X., McFadden, M. E., Barber, R. W. & Robb, M. J. Mechanochemical Regulation of a Photochemical Reaction. *J. Am. Chem. Soc.* **2018**,140, 14073–14077.
66. Cao, B.; Boechler, N.; Boydston, A. J. Additive Manufacturing with a Flex Activated Mechanophore for Nondestructive Assessment of Mechanochemical Reactivity in Complex Object Geometries. *Polymer* **2018**, *152*, 4–8.

Image	Name	Description
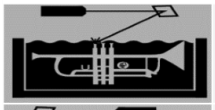	Vat Photopolymerization	Liquid photopolymer is cured through selective exposure to light (via a laser or projector) and converted into a solid part
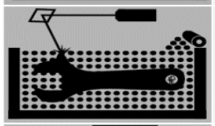	Powder bed fusion	Power material is selectively melted by heating using a laser or electron beam. The powder surrounding the consolidated part acts as a support for the printed structure
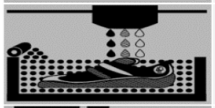	Binder jetting	Liquid bonding agents are applied selectively onto thin layers of powder, building up materials layer by layer
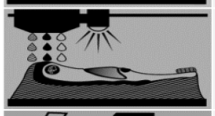	Material Jetting	Droplets of material like a photocurable resin is deposited in layers
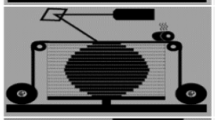	Sheet Lamination	Sheets of material are stacked and bonded together. The bonding can be chemicals like adhesive or welding (metal)
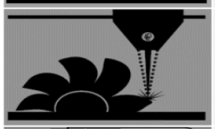	Directed energy deposition	Powder or wire is fed into a melt pool which has been generated on the surface where it adheres to underlying parts by using energy source
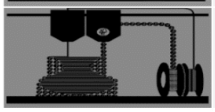	Material Extrusion	Material is extruded from nozzles or orifices which can be stacked in layers to form a part

Table 1.1: List of current additive manufacturing techniques according to ASTM guidelines

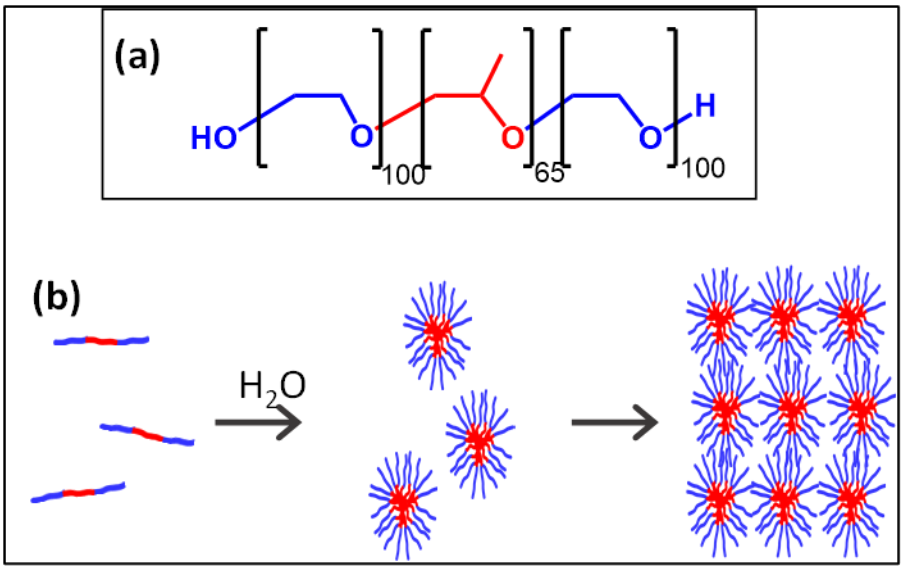

Figure 1.1: (a)Chemical structure of Pluronic F127 and (b) cartoon depiction of mechanism of gel formation when Pluronic F127 is dissolved in water. Individual polymer strands pack together to form core-shell micelles which pack into a cubic close pack structure.

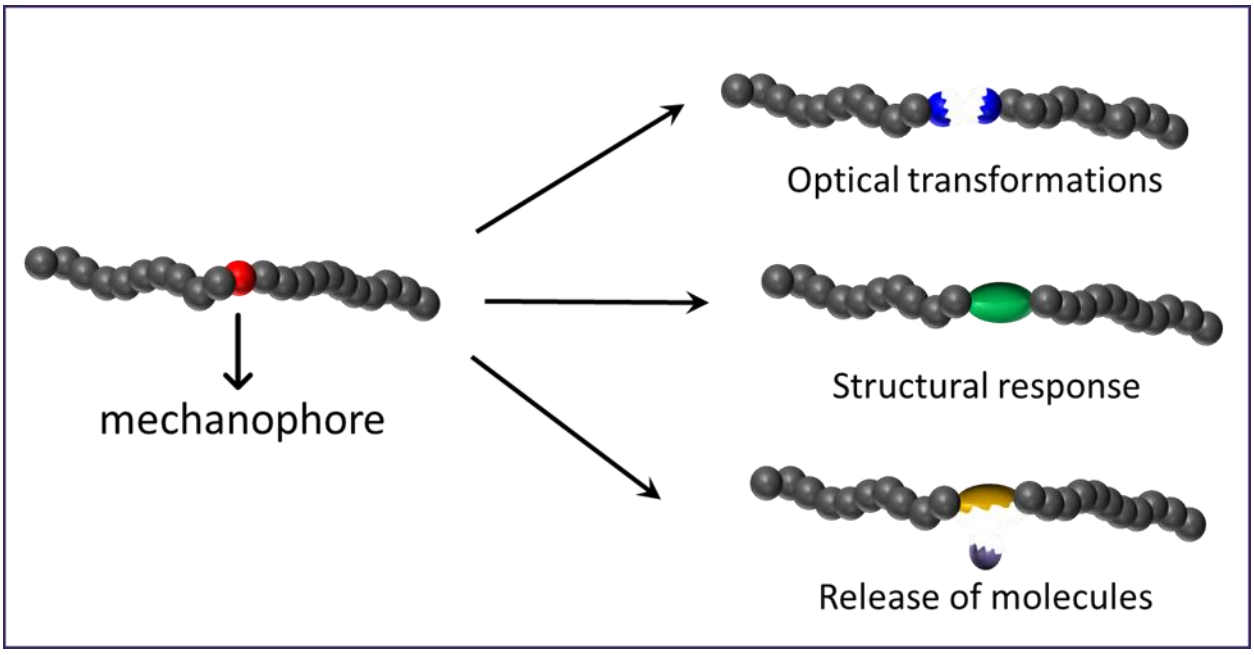

Figure 1.2: Cartoon of a mechanophore responding to mechanical stimulus via 3 major pathways. These responses can be reversible or irreversible.

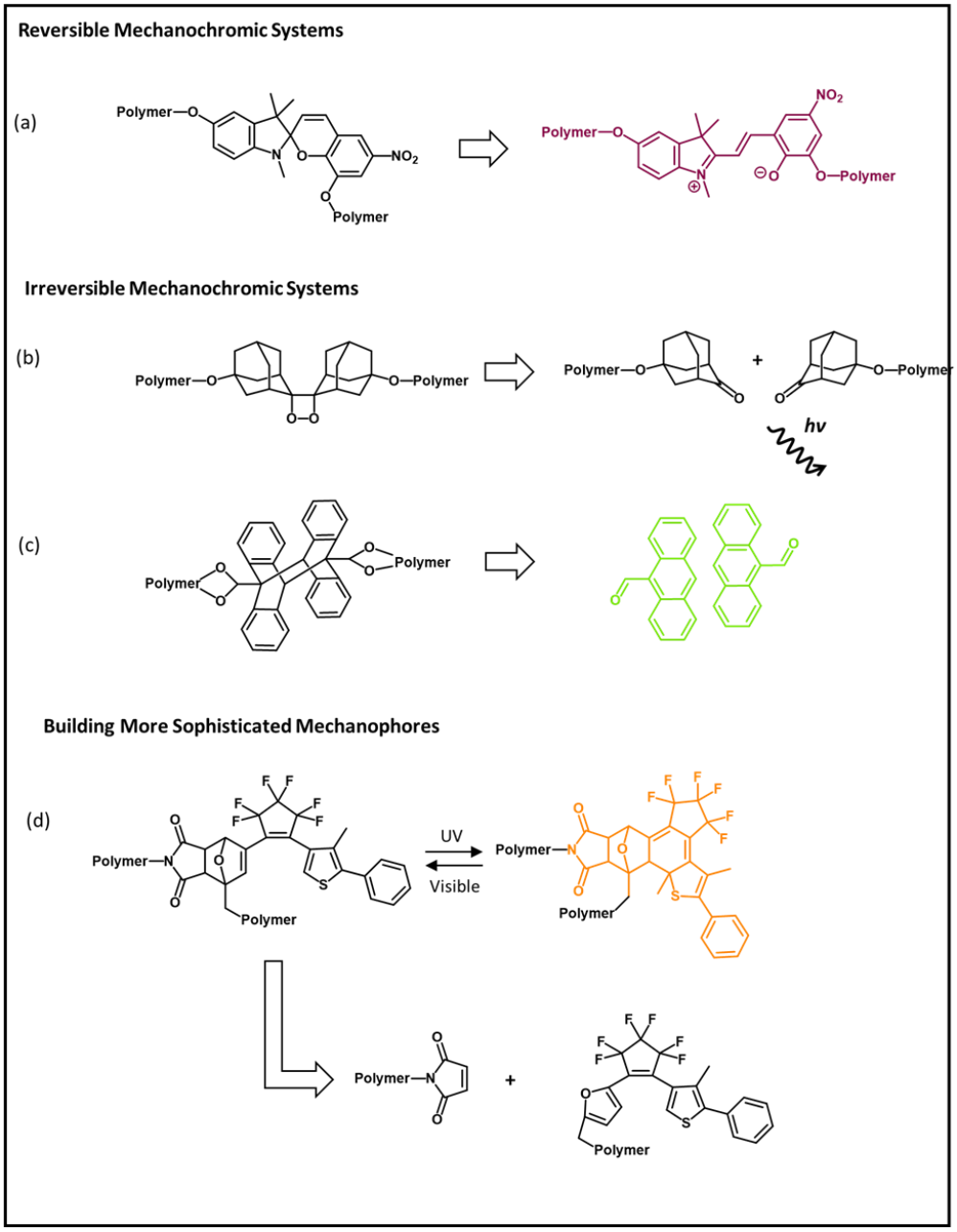

Figure 1.3: Mechanochromophores activate via a range of mechanism and can exhibit reversible or irreversible responses. Shown here (a) reversible activation of spiropyran (b-c) irreversible conversions of dioxetanes and anthracenes and (d) photochemically gated mechanical scission of a diaryethene photoswitch adduct.

CHAPTER 2: **CATALYTICALLY INITIATED GEL-IN-GEL PRINTING OF COMPOSITE HYDROGELS**

2.1 ABSTRACT

Herein, we describe a method to 3D print robust hydrogels and hydrogel composites via gel-in-gel 3D printing with catalytically activated polymerization to induce cross-linking. A polymerizable shear-thinning hydrogel ink with a catalyst was directly extruded into a shear-thinning hydrogel support bath with an initiator in a pattern-wise manner. When the two gels came into contact, the free radicals generated by the catalyst initiated the free-radical polymerization of the hydrogel ink. Radical polymerizations are advantageous as non-stoichiometric reactions, wherein a single radical initiator can initiate a cascade of reactions to afford a robust cross-linked material. But unlike photo-curing, a catalyst-initiated polymerization is suitable for printing hydrogel composites of varying opacity since it does not depend upon light penetration through the sample. The hydrogel support bath also exhibited a temperature responsive behavior in which the gel 'melted' upon cooling below 16^{o}C. Therefore, the printed object was easily removed by cooling the gel to a liquid state. Hydrogel composites with graphene oxide and multi-walled carbon nanotubes (MWCNTs) were successfully printed. The printed composites with MWCNTs afforded photo-thermally active objects, which have utility as stimuli-responsive actuators.

2.2 INTRODUCTION

Additive manufacturing (also referred to as 3D printing) represents a versatile technology which enables customized fabrication of three-dimensional objects for applications ranging from soft robotics[1] to tissue engineering.[2-4] Direct-write 3D printing is a specific type of additive manufacturing in which an ink is extruded through a nozzle that is rastered across a surface in a pattern-wise manner. Many classes of ink materials have been developed for direct-write 3D printing that includes colloidal suspensions,[5] polymeric materials,[6] and concentrated polyelectrolyte complexes.[7] Developing new printable materials requires careful consideration of the viscoelastic behavior of the inks. For example, an ideal ink for direct-write 3D printing should shear-thin during the extrusion process to ensure uniform dispensation of the ink, but then rapidly gel or solidify upon exiting the nozzle in order to maintain the printed form. A common approach to rapidly increase the elastic modulus of the extruded material is to induce cross-linking of the polymer chains. For example, sodium alginate can be cross-linked in the presence of calcium ions via ionic bonds,[6] and polymers functionalized with (meth)acrylate groups undergo rapid polymerization in the presence of radical initiators.[8]

Polymer hydrogels have emerged as a promising candidate for 3D bioprinting implants,[9-11] and tissue constructs.[12-14] The soft, water-filled nature of these materials mimic the internal environment of the living tissues and the extracellular matrix. Polymeric hydrogels and composite materials also have useful for applications beyond tissue engineering in areas such as flexible supercapacitors,[15] microfluidics,[16,17] and sensors.[18,19] One of the challenges in direct-write 3D printing of hydrogels is the fabrication of robust spanning or overhanging structures. The viscoelastic properties of the hydrogel inks are typically unsuitable for situations wherein the

hydrogel is printed in a manner that requires it to support its own weight. Thus, features without underlying support structures tend to sag or collapse, which restricts direct-write 3D printing to objects wherein each successive hydrogel layer is printed immediately above another hydrogel layer. One approach to resolve this issue is to extrude the ink directly into a reservoir of a second supporting gel. For example, Feinberg and co-workers have developed a method known as freeform reversible embedding of suspended hydrogels (FRESH) [20], wherein a liquid-phase material ink is extruded into gel support bath. In one form of this approach, the liquid ink is comprised of sodium alginate, which rapidly gels when the polymer encounters the calcium embedded within the support gel. Burdick and co-workers have described[21] a similar approach in which supramolecular cross-linking between polymer chains in the liquid ink and the bath gels induces the rapid gelation of the ink. However, these systems are dynamic and can change or degrade over time, which limits their use to specific applications.

Herein, we report a catalyst-initiated gel-in-gel 3D printing for creating 3D structured hydrogels and hydrogel composites. The process involves the extrusion of a cross-linkable hydrogel ink directly into a support hydrogel bath containing a catalyst that initiates in situ free-radical polymerization (Figure 2.1). Because each initiator can initiate a separate polymerization, this cross-linking mechanism is non-stoichiometric. This feature is important when compared to other inks, such as calcium alginate, in which the extent of cross-linking is proportional to the concentration of calcium ions present. Photo-initiated polymerizations are also non-stoichiometric but require the printed and support structures to be transparent. Both the hydrogel ink and the support hydrogel are stimuli-responsive materials based on F127, which is a commercially

available ABA triblock copolymer of poly (ethylene oxide)-block-poly (propylene oxide)-block-poly(ethylene oxide) (PEO-b-PPO-b-PEO). This polymer forms stimuli-responsive hydrogels (at 20-40 wt % concentrations in water) that exhibit a concentration and temperature-dependent sol-gel transition at ~16 °C and is also shear-thinning.[23]

The temperature-response facilitates three key features of this process: (i) loading of the hydrogel ink into the printer cartridge (or syringe), (ii) incorporation of additives into the hydrogel ink, and (iii) removal of the printed object from the support gel. The shear-thinning response ensures smooth extrusion of hydrogel filaments from the nozzle, as well as minimal disruption of the support gel by the traversing nozzle. The hydrogel ink is comprised of F127-dimethacrylate (F127-DMA), which is a cross-linkable form of F127 with methacrylate functionalities at the chain ends. The reaction is initiated when the hydrogel ink comes into contact with the catalyst present in the support gel to form a robust 3D construct. We also demonstrate that the hydrogel ink is amenable to the inclusion of functional nanomaterial additives such as graphene oxide (GO) and carbon nanotubes (CNTs) to afford hydrogel composites. These hydrogel composites are of interest because the nanomaterials can impart new functionalities or material behaviors, such as near-IR photothermal response.

2.3 Materials and Methods

2.3.1 Materials:

Pluronic F-127 (BioReagent, powder, suitable for cell culture), was purchased from Sigma Life Science. Triethylamine (≥ 99.5%), Methacryloyl chloride (97%; 200 ppm monomethyl ether hydroquinone as stabilizer), graphite and multi-walled carbon nanotubes (MWCNTs), (product

no.659258-2G, Lot no. MKBZ7167V) were purchased from Sigma-Aldrich. Toluene (HPLC Grade, 99.9%), Sulphuric acid, nitric acid, potassium permanganate, ethanol and diethyl ether (anhydrous) were purchased from Fisher Chemical. Details about all syntheses are included in the supporting information. (Figure A1)

2.3.2 Preparation of ink gel.

The ink hydrogel was prepared by dissolving 2.5 g of F127DMA in 7.5 g deionized water and stirred at 4 °C overnight or till the polymer completely dissolved. This was followed by the addition 0.1 wt % TMEDA under constant stirring. Food color was added to get proper images of the printed gel. The hydrogel was equilibrated at 4 °C until it is free of air bubble and then poured into syringes fitted with a nozzle of 0.41 mm inner diameter and kept at room temperature till the solution acquired a uniform temperature around 25 °C and turned into a shear responsive gel. For the composite ink gels, the desired concentration of additives was achieved by adding a fixed volume of the stock solution into the prepared native hydrogel followed by sonication for an hour at 4 °C.

2.3.3 Preparation of Support gel.

The support gel was prepared by adding 2 g of the commercially available Pluronic F127 to 8g of deionized water and stirring under ice till the polymer completely dissolves. Ammonium persulfate (1 % by weight of hydrogel) was added to it while stirring. It was then poured into 100 mm Petri dishes and kept in an oven at 25 °C for 10 mins to ensure complete gelation of the whole volume.

2.3.4 Rheology.

For rheological characterization of the materials, dynamic oscillatory experiments were performed on a TA Instruments Discovery Hybrid Rheometer-2 (DHR-2) equipped with a peltier device. The

instrument operates by applying a known displacement (stress) and measuring the material's resistance (strain) to the force. Rheology tests were conducted by depositing hydrogel between the rheometer base plate and a 20 mm parallel plate geometry at a gap of 1 mm. Samples were equilibrated in an ice bath for at least 30 min and then were carefully loaded onto the Peltier plate at 5°C and a preshear experiment was applied to eliminate air bubbles from the sample. The sample was equilibrated at 25°C for 8 min before each run. Gel yield stresses were measured under oscillatory stress (frequency 1 Hz, 25°C) starting with an initial stress of 1 Pa up to 104 Pa. Viscosity versus shear rate experiments were performed in the range between 0.01 and 10 of shear rate. Cyclic shear thinning tests (frequency 1 Hz) were performed at 25°C using alternating strains of 1% for 5 min and 100% for 3 min per cycle, to investigate the shear-thinning and recovery behavior of the hydrogels. Temperature ramp experiments were performed at 1 Hz from 5−50 °C at a rate of 2 °C/min.

2.3.5 Printing.

The printing was performed on a Prusa I3 RepRap printer. All CAD models were designed in Solidworks 2016. All printing was done using barrel shaped size 22 Metcal extrusion nozzle (Inner Diameter 0.41 mm) with extrusion air pressure of 20 psi (~2.4 atm). Printing parameters such as speed and bath gel composition were optimized. The tip of the needle was positioned at a designated point on the support gel holder that served as the XYZ origin for all prints. Printing was controlled through standard 3DP software to generate G-code commands (Slic3r) from CAD-generated (Solidworks).

2.4 Results and Discussions

Figure 2.1 shows the general scheme for the catalyst-initiated gel-in-gel 3D printing. The cross-linkable ink hydrogel, comprised of 25 wt % F127-DMA, was extruded through a barrel nozzle into a support hydrogel bath containing unmodified F127 hydrogel (20 wt %). The support gel behaved as a Bingham plastic, which allowed the nozzle to traverse through the support gel without fracturing it under the high shear forces. On the other hand, the support gel behaved as a solid under low shear, which provided mechanical support to the printed object suspended within the hydrogel. Another important feature of the gel-in-gel 3D printing process was the utilization of a catalyst-initiated radical polymerization (instantaneously initiated when the ink gel and the support gel came into contact) to afford a covalently cross-linked 3D printed object. This approach offers a contrast to other reports in which non-covalent interactions were utilized to cross-link the hydrogels.[15,16]

The dimethacrylate end-groups of the hydrogel ink was polymerized using ammonium persulfate (APS) as the initiator and tetramethylethylenediamine (TMEDA) as the catalyst; present in the support gel and ink gel, respectively (or vice versa). Thus, the polymerization was only initiated after the extruded filament and surrounding support gel came into contact. The printed structure was removed from the support gel bath by using the thermoreversible gel-sol transition property of the F-127 hydrogel. Upon completion of the printing, the support gel was cooled for 15 min at 4 °C in order to melt the gel and remove the 3D printed object.

A temperature ramp rheometrical experiment was performed to characterize the thermo-responsive behavior of the ink hydrogel as shown in Figure 2.2(a), which shows the changes to the loss (G") and storage (G') moduli with temperature. The gelation temperature (represented by the

intersection of the storage and loss moduli) for a 25 wt % F127-DMA solution was ~16 °C. Below this temperature, the hydrogel ink is a fluid, as exhibited by the low values (<10 Pa) for both the G' and G". The material transforms into a gel above the gelation temperature where G' is several orders of magnitude larger than G". Thus, at the operating temperature for the direct-write 3D printer (21°C) the ink exists in its 'gel' state.

For extrusion-based printing processes, the shear-thinning and yield stress behaviors are of critical importance to make the material flow from its solid like state.[22] A strain sweep at room temperature showed that the ink hydrogel was moderately firm at 25 wt % with a G' of ~20 kPa (Figure 2.2(b)). At higher stresses, beyond the critical yield stress (647 Pa), the material response becomes non-linear with the storage modulus rapidly decreasing with an increase in applied stress. This is an important parameter for layer-by-layer processes, such 3D printing since it indicates the maximum load bearing capacity of the gel as it supports subsequent stacked layers. (We note that this parameter is more pertinent to structures printed in air, as opposed to those printed inside a support gel). The shear-thinning behavior of the ink was confirmed, as shown in Figure 2.2(c), wherein the viscosity decreased almost three orders in magnitude with increasing shear rate. This behavior ensured a smooth flow of the ink gel from the nozzle during the 3D printing process. The reversible shear-thinning under stress and rapid self-healing nature of the hydrogel networks under shear-relaxed conditions manifests itself in the instantaneous response of the gel modulus to changes in the applied strain (Fig. 2.2(d)). F127-DMA hydrogel was subjected to five successive cycles of alternating low (1%) and high (100%) strains for 5 and 3 min, respectively. The hydrogel exhibited a sharp decrease in the storage moduli (G') at high strains and immediate recovery at low strains for each cycle. The hydrogel demonstrated modulus decrease and recovery each in less

than 15 s. The hydrogel displayed minimal hysteresis between strain cycles, which suggests that the polymers can rapidly reform the physical cross-links between the polymer chains that provide the mechanical stability of the gel. The function of the support gel containing unmodified 20 wt % F127 in water was to physically maintain the shape and position of the printed forms, while permitting the translation of the nozzle through the support gel in the absence of viscous drag. The oscillatory stress sweep plot of the support hydrogel (Figure 2.3) shows it has a shear storage modulus (G') of 21 kPa, which is suitable to support the weight of the printed structure. The material also shows a yield stress of ~100 Pa, at which point it cannot maintain its rigid gel form, thus enabling the smooth movement of the printing head through the gel without fracture. The modulus of the support bath was found to be highly dependent on temperature, wherein the elastic modulus decreased with temperature. Below 15°C the material shows no appreciable elastic modulus. Thus, at these reduced temperatures, the fluidity of the support gel enables facile removal of the printed object upon completion.

Hydrogels traditionally have low mechanical strength, which during 3D printing translates into problems such as the fusion of adjacent layers due to a vertical collapse of the hydrogel, or the inability to print spanning structures. Figure 2.4 (a) and (b) provides a comparison of hydrogels that were printed without and with a support gel, respectively. During conventional direct-write 3D printing of the hydrogel ink without a support gel, the upper layer printed filaments sagged downward (Figure 2.4(a)), and as a result, the printed layers became more rounded and sank to the surface below. However, with gel-in-gel 3D printing, the support matrix ensures that there is no sag observed, and the filaments retain their tubular shape without collapsing, which leads to a

higher print fidelity. This method also enables the facile fabrication of structures with overhangs as demonstrated by 3D printing an inverted cone in Figure 2.4(c)-(e)

Other reports[24,25] which utilize a post-printing photo-curing step are restricted to 3D objects that readily transmit UV light through the entirety of the sample. The physical properties of hydrogels can be enhanced by incorporation of organic additives,[26,27] carbon nanotubes,[28] and other nanomaterials[29] to afford hydrogels with improved mechanical[30] or conductive properties.[31] However, these hydrogel composites are typically opaque or light-absorbing and cannot be efficiently cured by irradiation with light. GiG 3DP does not rely on the transmission of light through the sample, and therefore, can lead to more uniformly cured composite hydrogels with enhanced functionality. We demonstrated this concept by creating composite hydrogels that either contained graphene oxide (GO) or multi-walled carbon nanotubes (MWCNT). The thermos-reversible properties of the F127-DMA hydrogel facilitated the uniform incorporation and distribution of nanomaterials within the ink at low temperature (10°C). We did not observe significant precipitation or settling of the nanomaterials, which may suggest that the polymers used in this study may also serve as surfactants for dispersing these nanomaterials in the aqueous mixture. Upon warming the solution above 16°C, we observed the formation of a homogenous shear-thinning and temperature-responsive hydrogel. In general, as the concentration of nanomaterial additive increased, the hydrogel became darker in color. We observed that 0.2wt % GO and 2 wt % MWCNT (where the wt % was relative to the total weight of the hydrogel) could be added to the hydrogel, after which the hydrogels lost their temperature response. These hydrogels were characterized rheometrically in a temperature ramp plot (Figure 2.5(a)) which showed the gelation temperature increased with the filler concentration (~19°C). The shear-

thinning and self-healing properties of the composites resembled the parent F-127-DMA hydrogel (Figure 5 (b)-(d)). These composites were successfully printed into robust 3D objects, as shown in Figure 5(e) and 5(f).

Carbon nanotubes are nanomaterials which show remarkable absorption in the near-infrared (NIR) (λ= 700-1100nm) region. They are known to have a high photothermal conversion rate,[32] by which the material absorbs in the NIR region and convert that energy into heat by non-radiative decay. The photothermal heating effect in carbon nanotubes was exploited to make responsive composite gels which maybe be developed into hydrogel actuators with potential in fields like soft robotics, microfluidics and medicine.[33] In order to demonstrate this concept, hydrogel filaments were drawn with and without MWCNTs and irradiated with an IR-laser for up to 3 min. The resulting shrinkage in the hydrogel due to the local heating and subsequent evaporation of water was monitored. The filament with MWCNTs showed a rapid 70% decrease of its initial diameter, while the filament without the additive exhibited a 20% decrease. It was also seen that the amount of photothermal effect was proportional to the MWNT content. (Figure 2.6)

2.5 Conclusion

In conclusion, we developed a gel-in-gel 3D printing process that uses an in situ catalytic cross-linking approach that occurs when the hydrogel ink comes into contact with the support gel. Both the ink and support hydrogels were shear-thinning materials. The ink gel was extruded in a smooth and continuous fashion and was held in place by the support gel. At the same time, free-radical cross-linking of the ink hydrogel occurred when the catalyst in the ink gel and the initiator of the support gel came into contact. Radical polymerizations are advantageous as non-stoichiometric reactions, wherein a single radical initiator can initiate a cascade of reactions to afford a robust

cross-linked material. This contrasts hydrogel inks based on ionic bonds, such as calcium alginate, which requires stoichiometric quantities of calcium for cross-linking. Our approach is suitable for applications wherein a robust (largely non-biodegradable) hydrogel network is required. In addition to the printing of nanocomposite hydrogels, this approach enabled spanning and over-hanging features to be successfully printed with high fidelity. The nanocomposite hydrogels comprised of MWCNTs were photo-thermally active and could be used to 3D print stimuli-responsive actuators and devices.

2.6 REFERENCES

1. (a)Sydney Gladman, A.; Matsumoto, E. A.; Nuzzo, R. G.; Mahadevan, L.; Lewis, J. A. Biomimetic 4D Printing. *Nat. Mater.* **2016**, *15*, 413–418; (b)Bakarich, S. E.; Gorkin, R.; Panhuis, M. in het; Spinks, G. M. 4D Printing with Mechanically Robust, Thermally Actuating Hydrogels. *Macromol. Rapid Commun*. **2015,** 36, 1211–1217; (c) Sundaram, S.; Kim, D. S.; Baldo, M. A.; Hayward, R. C.; Matusik, W. 3D-Printed Self-Folding Electronics. *ACS Appl. Mater. Interfaces* **2017**, DOI: 10.1021/acsami.7b10443.
2. Murphy, S. V.; Atala, A. 3D Bioprinting of Tissues and Organs. *Nat. Biotech.* **2014**, *32*, 773–785.
3. Martin, I.; Simmons, P. J.; Williams, D. F. Manufacturing Challenges in Regenerative Medicine. *Sci. Transl. Med.* **2014**, *6*, 232fs16.
4. Guvendiren, M.; Lu, H. D.; Burdick, J. A. Shear-Thinning Hydrogels for Biomedical Applications. *Soft Matter* **2012**, *8*, 260–272.
5. Smay, J. E.; Cesarano, J.; Tuttle, B. A.; Lewis, J. A. Directed Colloidal Assembly of Linear and Annular Lead Zirconate Titanate Arrays. *J. Am. Ceram. Soc.* **2004**, *87*, 293–295.
6. Lee, K. Y.; Mooney, D. J. Alginate: Properties and Biomedical Applications. *Prog. Polym Sci.* **2012**, *37*, 106–126.
7. Su, B.; Zhang, D.; Button, T. W. Micropatterning of Fine Scale Ceramic Structures. *J. Mater. Sci.* **2002**, *37*, 3123–3126.
8. Custódio, C. A.; Reis, R. L.; Mano, J. F. Photo-Cross-Linked Laminarin-Based Hydrogels for Biomedical Applications. *Biomacromolecules* **2016**, *17*, 1602–1609.
9. Kang, H.-W.; Lee, S. J.; Ko, I. K.; Kengla, C.; Yoo, J. J.; Atala, A. A 3D Bioprinting System to Produce Human-Scale Tissue Constructs with Structural Integrity. *Nat. Biotech.* **2016**, *34*, 312–319.
10. Duan, B.; Hockaday, L. A.; Kang, K. H.; Butcher, J. T. 3D Bioprinting of Heterogeneous Aortic Valve Conduits with Alginate/Gelatin Hydrogels. *J Biomed Mater Res A* **2013**, *101*, 1255–1264.
11. Ishida, Y.; Miyasaka, T. Dimensional Accuracy of Dental Casting Patterns Created by 3D Printers. *Dent. Mater. J* **2016**, *35*, 250–256.
12. Sinha, G. Cell Presses. *Nat. Biotech.* **2014**, *32*, 716–719
13. Derby, B. Printing and Prototyping of Tissues and Scaffolds. *Science* **2012**, *338*, 921–926.
14. Lee, C. H.; Rodeo, S. A.; Fortier, L. A.; Lu, C.; Erisken, C.; Mao, J. J. Protein-Releasing Polymeric Scaffolds Induce Fibrochondrocytic Differentiation of Endogenous Cells for Knee Meniscus Regeneration in Sheep. *Sci. Transl. Med.* **2014**, *6*, 266ra171-266ra171.
15. (a) Shi, Y.; Pan, L.; Liu, B.; Wang, Y.; Cui, Y.; Bao, Z.; Yu, G. Nanostructured Conductive Polypyrrole Hydrogels as High-Performance, Flexible Supercapacitor Electrodes. *J. Mater. Chem. A* **2014**, *2*, 6086–6091; (b) Dubbin, K.; Hori, Y.; Lewis, K. K.; Heilshorn, S. C. 3D Bioprinting: Dual-Stage Crosslinking of a Gel-Phase Bioink Improves Cell Viability and Homogeneity for 3D Bioprinting (Adv. Healthcare Mater. 19/2016). Adv. Healthcare Mater. 2016, 5 (19), 2568–2568.

16. Burdick, J. A.; Khademhosseini, A.; Langer, R. Fabrication of Gradient Hydrogels Using a Microfluidics/Photopolymerization Process. *Langmuir* **2004**, *20*, 5153–5156.
17. Kishi, R.; Miura, T.; Kihara, H.; Asano, T.; Shibata, M.; Yosomiya, R. Fast pH-Thermo-Responsive Copolymer Hydrogels with Micro-Porous Structures. *J. Appl. Polym. Sci.* **2003**, *89*, 75–84.
18. Holtz, J. H.; Asher, S. A. Polymerized Colloidal Crystal Hydrogel Films as Intelligent Chemical Sensing Materials. *Nature* **1997**, *389*, 829–832.
19. Lee, Y.-J.; Braun, P. v. Tunable Inverse Opal Hydrogel pH Sensors. *Adv. Mater.* **2003**, *15*, 563–566.
20. Hinton, T. J.; Jallerat, Q.; Palchesko, R. N.; Park, J. H.; Grodzicki, M. S.; Shue, H.-J.; Ramadan, M. H.; Hudson, A. R.; Feinberg, A. W. Three-Dimensional Printing of Complex Biological Structures by Freeform Reversible Embedding of Suspended Hydrogels. *Sci. Adv.* **2015**, *1*, e1500758
21. Highley, C. B.; Rodell, C. B.; Burdick, J. A. Direct 3D Printing of Shear-Thinning Hydrogels into Self-Healing Hydrogels. *Adv. Mater.* **2015**, *27*, 5075–5079.
22. Zhang, M.; Vora, A.; Han, W.; Wojtecki, R. J.; Maune, H.; Le, A. B. A.; Thompson, L. E.; McClelland, G. M.; Ribet, F.; Engler, A. C.; Nelson, A. Dual-Responsive Hydrogels for Direct-Write 3D Printing. *Macromolecules* **2015**, *48*, 6482–6488.
23. Pawar, G. M.; Koenigs, M.; Fahimi, Z.; Cox, M.; Voets, I. K.; Wyss, H. M.; Sijbesma, R. P. Injectable Hydrogels from Segmented PEG-Bisurea Copolymers. *Biomacromolecules* **2012**, *13*, 3966–3976.
24. (a)Wu, W.; DeConinck, A.; Lewis, J. A. Omnidirectional Printing of 3D Microvascular Networks. *Adv. Mater.* **2011**, *23*, H178–H183.
25. (b)Hinton, T. J.; Hudson, A.; Pusch, K.; Lee, A.; Feinberg, A. W. 3D Printing PDMS Elastomer in a Hydrophilic Support Bath via Freeform Reversible Embedding. *ACS Biomater. Sci. Eng*. **2016**, 2, 1781–1786.
26. Müller, M.; Becher, J.; Schnabelrauch, M.; Zenobi-Wong, M. Nanostructured Pluronic Hydrogels as Bioinks for 3D Bioprinting. *Biofabrication* **2015**, *7*, 035006.
27. Lee, Y.; Jung Chung, H.; Yeo, S.; Ahn, C.-H.; Lee, H.; B. Messersmith, P.; Gwan Park, T. Thermo-Sensitive, Injectable, and Tissue Adhesive Sol–gel Transition Hyaluronic Acid /Pluronic Composite Hydrogels Prepared from Bio-Inspired Catechol - Thiol Reaction. *Soft Matter* **2010**, 6, 977–983.
28. Lin, S.; Yuk, H.; Zhang, T.; Parada, G. A.; Koo, H.; Yu, C.; Zhao, X. Stretchable Hydrogel Electronics and Devices. *Adv. Mater.* **2016**, *28*, 4497–4505.
29. Joddar, B.; Garcia, E.; Casas, A.; Stewart, C. M. Development of Functionalized Multi-Walled Carbon-Nanotube-Based Alginate Hydrogels for Enabling Biomimetic Technologies. *Sci. Rep.* **2016**, *6*, 32456.
30. Zhang, L.; Wang, Z.; Xu, C.; Li, Y.; Gao, J.; Wang, W.; Liu, Y. High Strength Graphene Oxide/Polyvinyl Alcohol Composite Hydrogels. *J. Mater. Chem.* **2011**, *21*, 10399–10406.
31. Barrett, D. G.; Fullenkamp, D. E.; He, L.; Holten-Andersen, N.; Lee, K. Y. C.; Messersmith, P. B. pH-Based Regulation of Hydrogel Mechanical Properties Through Mussel-Inspired Chemistry and Processing. *Adv. Funct. Mater.* **2013**, *23*, 1111–1119.

32. Russo, A.; Ahn, B. Y.; Adams, J. J.; Duoss, E. B.; Bernhard, J. T.; Lewis, J. A. Pen-on-Paper Flexible Electronics. *Adv. Mater.* **2011**, *23*, 3426–3430.
33. Kosmala, A.; Wright, R.; Zhang, Q.; Kirby, P. Synthesis of Silver Nano Particles and Fabrication of Aqueous Ag Inks for Inkjet Printing. *Materials Chemistry and Physics* **2011**, *129* (3), 1075–1080.
34. Singh, R.; Torti, S. V. Carbon Nanotubes in Hyperthermia Therapy. *Adv. Drug Deliv. Rev.* **2013**, *65*, 2045–2060.

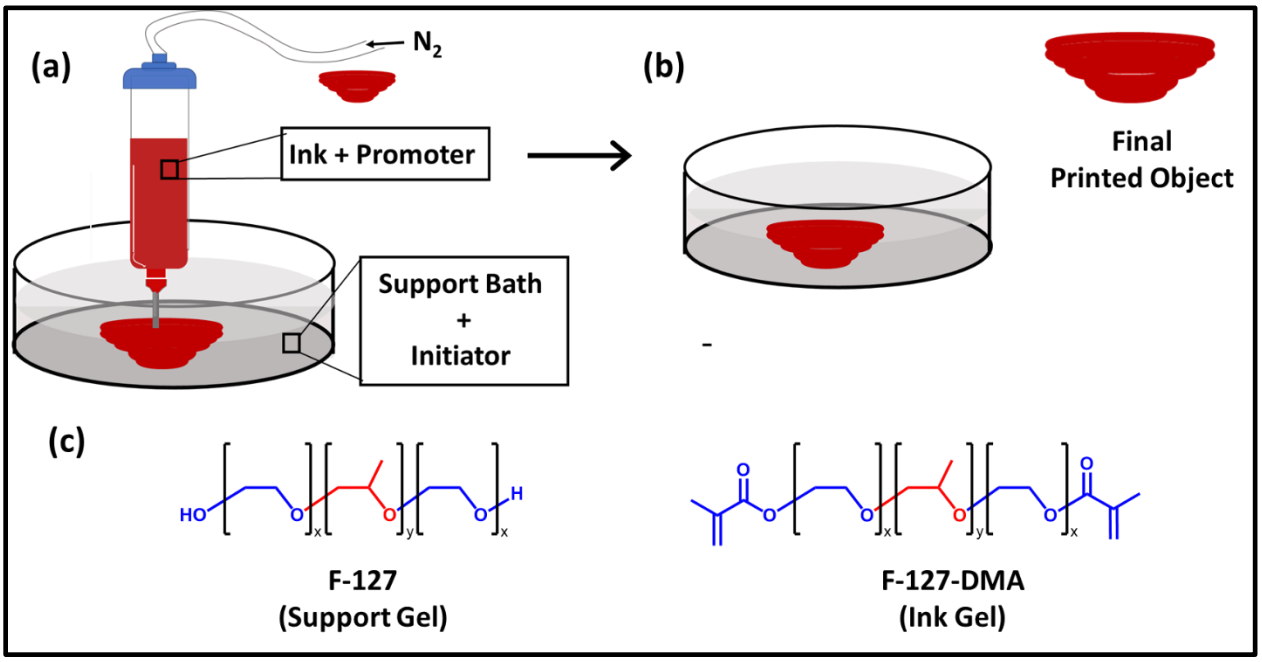

Figure 2.1 A representative scheme for the gel-in-gel 3D printing process: (a) a polymerizable shear-thinning ink gel with embedded initiator (APS) is extruded through a nozzle into a support gel embedded with catalyst (TMEDA). The polymerization of the methacrylate groups occurs upon contact between the catalyst and initiator. (b) The support gel is melted by cooling to 10 °C, and the fully cross-linked printed object is removed. (c) The chemical structures of the polymers used in the ink and support gels

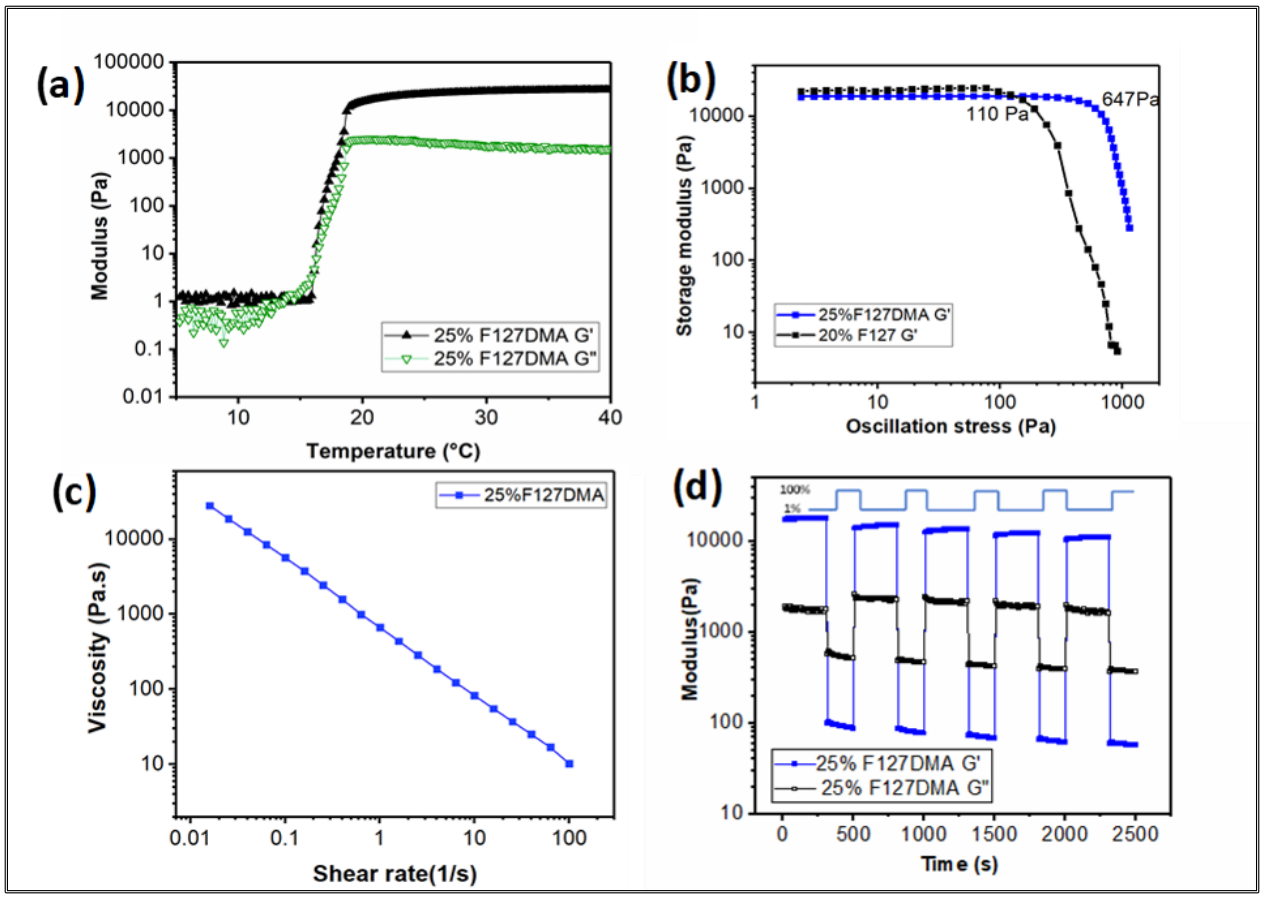

Figure 2.2 Rheometrical characterization of the ink hydrogel (25 wt % F-127-DMA in H_2O) at 25 °C unless noted otherwise: (a) A plot of the temperature ramp experiment for the ink. The intersection of the G' and G" represents the gelation temperature. (b) Oscillatory strain measurements of the ink hydrogel F-127-DMA, and the support hydrogel (F-127, 20 wt%) for comparison, (c) a plot of the viscosity versus the shear rate, demonstrating the shear-thinning behavior of the hydrogel; (d) cyclic strain experiment alternating between low (1 %) and high (100%) oscillatory strains. The plot shown tracks the storage (G') and loss (G") moduli over time.

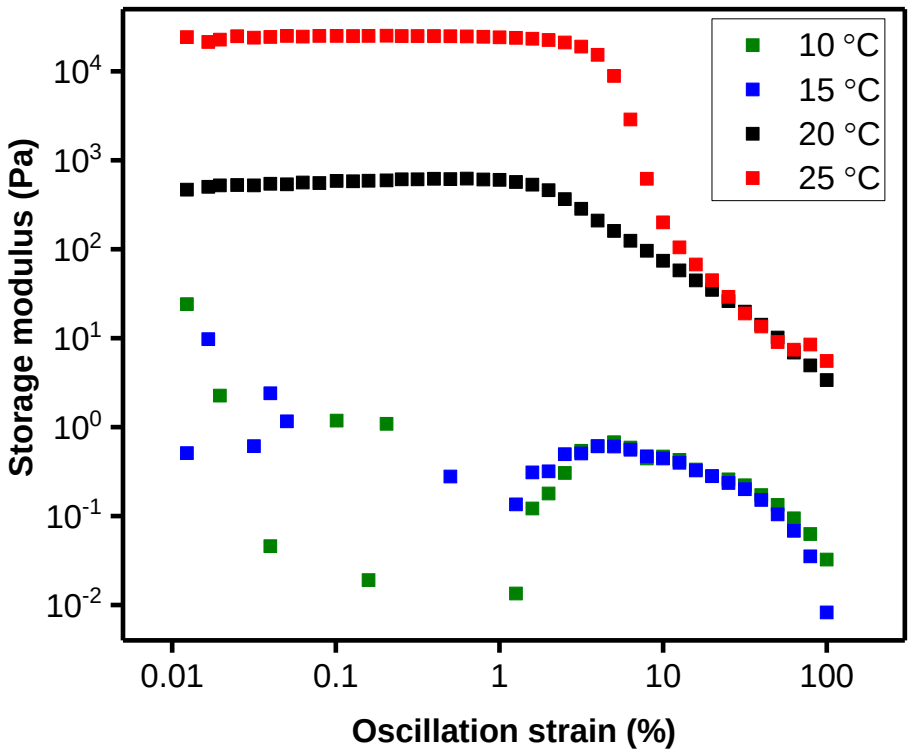

Figure 2.3 Rheometrical characterization of the support hydrogel (20 wt % F-127 in H_2O) which demonstrates the increase in the storage modulus (G') of the hydrogel as the temperature is increased from 10 to 25 °C.

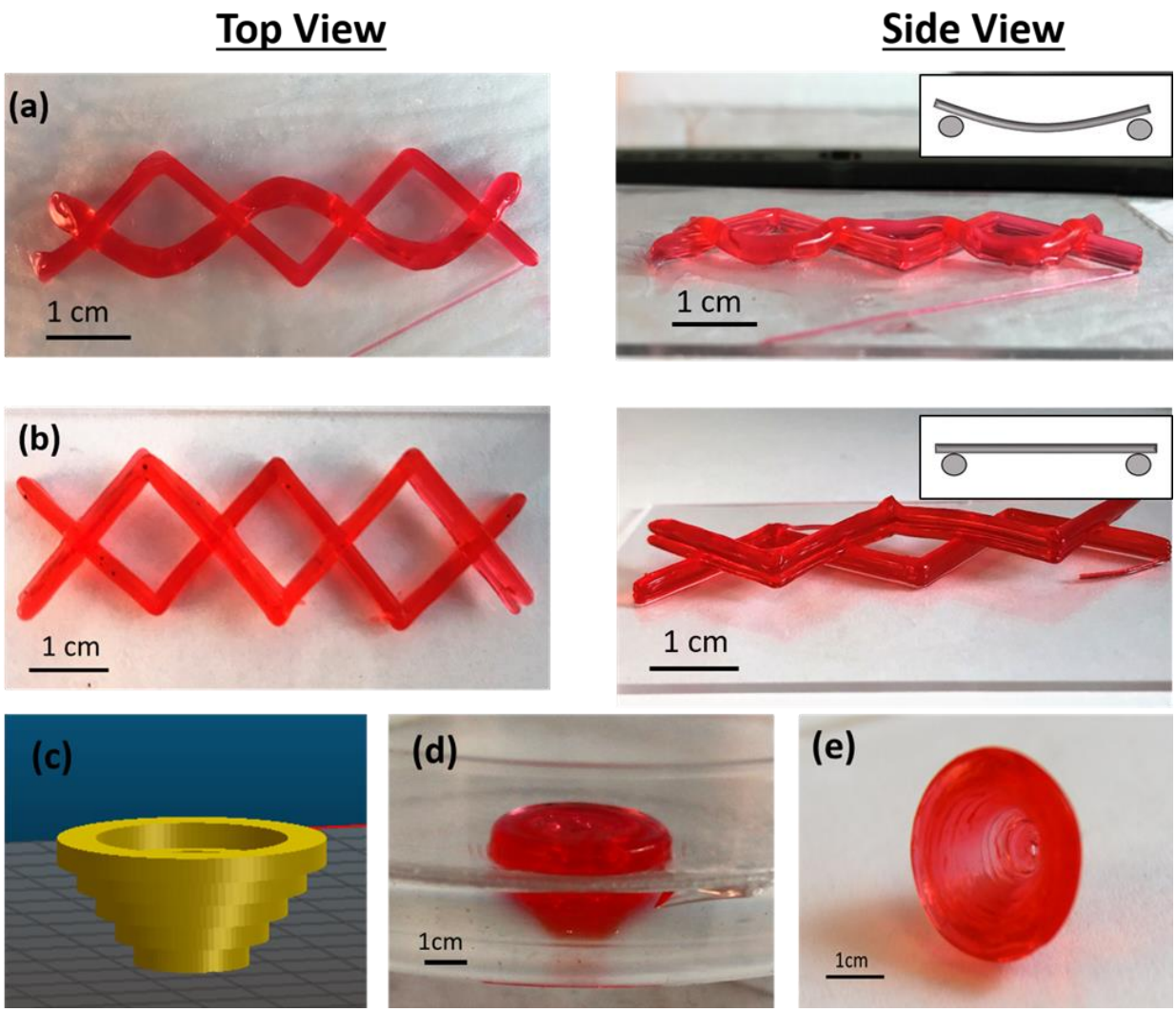

Figure 2.4 Top and side view of 3D printed structures (a) with support gel and (b) without support gel showing possible deformation in absence of the support gel (inset). (c) STL file of an inverted cone used for printing within the support gel. (d) an inverted cone printed and cured within the support gel and (e) after its removal from the bath gel

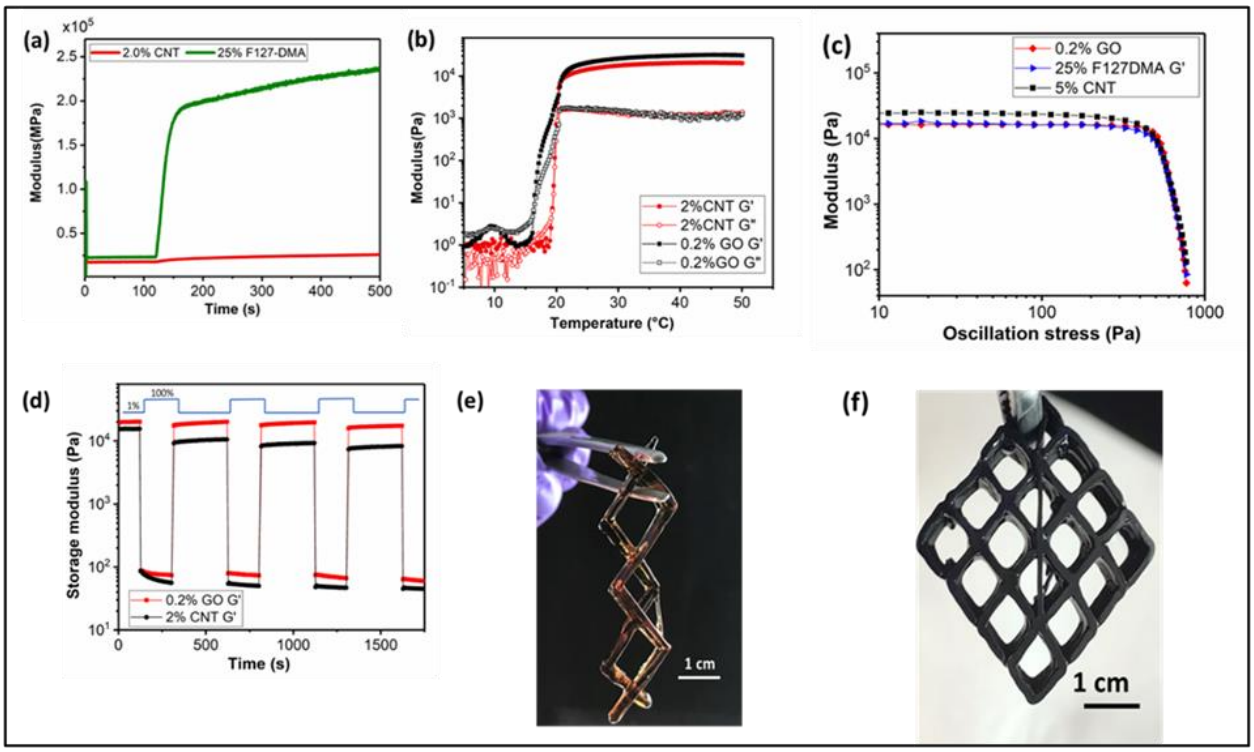

Figure 2.5 GO- and CNT-composite hydrogel inks (25 wt % F-127-DMA in H_2O at 25 °C unless noted otherwise): (a) A photorheometry plot showing the comparison in storage modulus (G') for native F127DMA hydrogels when irradiated with 365 nm light. (b) A plot of the temperature ramp experiment for the composite hydrogels, where the intersection of the G' and G" represents the gelation temperature for the hydrogel at this concentration. (c) Oscillatory strain measurements of the ink hydrogel composites, (d) cyclic strain experiment alternating between low (1 %) and high (100%) oscillatory strains. Optical images (e) and (f) of the 0.2 wt % and 2 wt % hydrogel composites of GO and CNT, respectively.

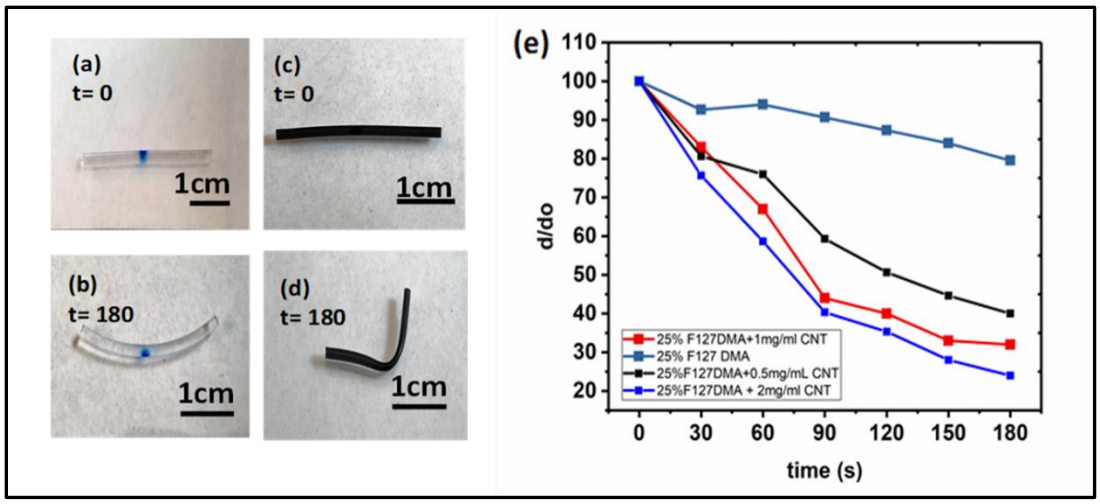

Figure 2.6 NIR laser driven volume change due to photothermal effect. (a) control filament at time 0 and (b) after 3minutes. (c) filament with 1 mg/ml MWNT/F127DMA at time 0 and (d)after 3 minutes. (c) Plot showing the change in diameter of both on F127DMA and MWNT/F127DMA filaments with time, where d and d_0 are the initial and final diameters of the filament

CHAPTER 3: **CHEMICAL MODIFICATION AND PRINTABILITY OF SHEAR-THINNING HYDROGEL INKS FOR DIRECT-WRITE 3D PRINTING**

3.1 ABSTRACT

Shear-thinning hydrogels are often employed in direct-write 3D printing, however, the viscoelastic behaviors that define a printable hydrogel have not been fully established. In this report, we demonstrate a library of hydrogel inks based on the incorporation of water-soluble reactive meth(acrylate) monomers into Pluronic F127-dimethacrylate hydrogels. This strategy afforded printed hydrogels with a broad range of chemical functionalities and mechanical properties. A systematic investigation was also performed to correlate the printability and mechanical properties to the viscoelastic properties of the shear-thinning hydrogel ink formulations. The materials with a high dynamic yield stress afforded extruded filaments that correlated well with the inner diameter of the printing nozzle. The static yield stress of the material was correlated to the extrusion pressure and print speed required for optimal printing. Thus, this study not only provides a set of new hydrogel inks for customized direct-write 3D printing, but also provides a guide for the future development of shear-thinning hydrogel inks for direct-write 3D printing.

3.2 INTRODUCTION

Additive manufacturing (also referred to as 3D printing) represents a versatile technology which enables the customized fabrication of three-dimensional objects for applications ranging from soft robotics[1,2] to tissue engineering.[3-5] Direct-write 3D printing is a type of additive manufacturing wherein a nozzle is rastered across a surface in a pattern-wise manner while an ink is deposited. An advantageous feature of this method of 3D printing is the easy access to the fabrication of functional materials, as well as multi-material printing.[6] A broad spectrum of inks has been developed that include polymeric materials ,[7-9] polyelectrolyte complexes,[10,11] and colloids[12]. As a result, direct-write 3D printing has become an attractive tool in the additive manufacturing of 3D objects.[13,14]

Polymer hydrogels have gained prominence as candidates for 3D printing and bioprinting of tissue constructs[15,16] and implants.[17,18] These soft materials are largely comprised of water, and serve as natural mimics of extracellular matrices. Synthetic hydrogels have tunable chemical features, and are also suitable for flexible electronics,[19,20] supercapacitors,[21] controlled drug release[22] and sensor[23,24] applications. Direct-write 3D printing is a facile method to pattern functional hydrogels to afford unique geometries and functionalities that are difficult or impossible to produce by conventional methods.[25] There are two strategies to print hydrogels via direct-write printing. The first strategy utilizes a low viscosity ink that is extruded from a nozzle, which then undergoes gelation induced by a chemical, photo-chemical,[26,27]or noncovalent process.[28] For example, calcium alginate gels have been printed in this manner using divalent calcium ions to cross-link the polyanionic polysaccharide.[29] Alternatively, a shear-thinning hydrogel ink—which

exhibits a viscoelastic response to applied pressure—can be extruded from a nozzle to directly deposit the gel into a 3D object. Our group has focused[30] on this latter approach to develop synthetic hydrogels for direct-write 3D printing. Despite the importance of understanding the viscoelastic behavior of hydrogel inks for direct-write 3D printing, a clear quantitative understanding of the viscoelastic requirements has yet to emerge. The palette of new hydrogel ink compositions for direct-write 3D printing can improved more rapidly with a fundamental understanding of the viscoelastic parameters necessary to fabricate 3D objects consistently and accurately. For example, the optimization of the printed resolution should be dictated by inks that minimize die-swelling behavior and affords extruded filament diameters commensurate with the inner diameter (I.D.) of the nozzle. Additionally, the ink should demonstrate rapid shear recovery and robust mechanical properties post-extrusion to maintain the printed form over time and allow easy manipulation and handling.

Pluronic F127 is a commercially available triblock copolymer with the composition, poly(ethylene oxide)-*block*-poly(propylene oxide)-*block*-poly(ethylene oxide) (PEO-*b*-PPO-*b*-PEO), which has been used as a biocompatible polymer for wound dressings and drug delivery.[31-33] When dissolved in aqueous media, F127 forms dual stimuli-responsive hydrogels (at 20-40 wt % concentrations in water) that responds to temperature and pressure (shear-thinning) stimuli.[30,34] Zenobi-Wong and co-workers have also demonstrated that F127 can be functionalized at the chain-ends with methacrylate groups (F127-DMA) to afford a cross-linkable hydrogel that can be photo-polymerized after 3D printing.[26] While F127 and F127-DMA are useful inks for direct-write 3D printing, the field presently lacks approaches to modify the hydrogel ink in order to afford printed structures with greater control over chemical functionality and mechanical properties of the printed hydrogel.

Herein, we demonstrate a library of hydrogel inks for direct-write 3D printing formulated with F127-DMA and water-soluble reactive monomer additives. Furthermore, we utilize rheometry to correlate the viscoelastic properties of these hydrogel inks to its printability. The addition of any number of such monomers can add new functionality to the native F127-DMA hydrogels, to increase its versatility as a biomaterial, pH/ temperature responsive smart material, or handle for peptide and fluorophore conjugation.[35,36] Previous reports for direct-write 3D printing hydrogel demonstrated that the quality of the printed object can be optimized by tuning parameters such as extrusion pressure and printing speed.[37] critical Mathematical models that predict filament resolution for shear-thinning hydrogels have also been developed.[38] M'Barki et al. recently investigated shear-thinning ceramic inks and demonstrated that the yield stress is a parameter in defining a suitable ink for extrusion-based printing.[39] There are two different types of yield stresses: the static yield stress (σ_{stat}) is the stress required to make a fluid (or gel) flow from rest, and the dynamic yield stress (σ_{dyn}) is the minimum stress required for a fluid (or gel) in motion to sustain its flow. Thus, in order for a shear-thinning hydrogel to be employed as a 3D printable ink, the material must not only overcome the static yield stress to initiate extrusion from a nozzle, but also exceed the dynamic yield stress to sustain the extrusion of a filament from that nozzle to form a continuous filament with minimum deformation. The dynamic yield stress also determines the extent to which a hydrogel filament continues to flow after it has exited the nozzle. The minimization of this flow will lead to filament diameters that are commensurate with the nozzle diameter. In this report, we will correlate the rheometrical analysis of these hydrogel inks to the printing parameters required for direct-write 3D printing. As a demonstration of the versatility that these inks provide,[40-41] we also demonstrate the changes to the mechanical properties of the printed hydrogels with the inclusion of these additives.

3.2 Materials and Methods

3.2.1 Materials

Pluronic F-127 (BioReagent, powder, suitable for cell culture) was purchased from Sigma Life Science. Triethylamine (≥ 99.5%), 2-hydroxy-2-methylpropiophenone (97%), 2-hydroxyethyl acrylate (96%), acrylic acid (99%), 2-(dimethylamino)ethyl methacrylate (98%), methacryloyl chloride (97%; 200 ppm monomethyl ether hydroquinone as stabilizer), and poly(ethylene glycol) diacrylate (M_n 700 Da) were purchased from Sigma-Aldrich. Toluene (HPLC Grade, 99.9%) and diethyl ether (anhydrous) were purchased from Fisher Chemical.

3.2.2 Functionalization of F127

Pluronic F-127 (30 g, 2.4 mmol, 1.0 eq) was dried under vacuum for 24 hours, then dissolved in 275 mL of anhydrous toluene (dried using activated molecular sieves, Grade 514, 4Å) under N_2 atmosphere at 40 °C. Triethylamine (3.4 mL, 24 mmol, 10 eq) was added to the solution via syringe. The reaction mixture was cooled to 0 °C, then a solution of methacryloyl chloride (2.4 mL, 24 mmol, 10 eq) in 25 mL toluene was added dropwise over 30 minutes with constant stirring. Following complete addition of methacryloyl chloride, the reaction mixture was stirred at 0 °C for 1 h, then warmed to room temperature and stirred for 24 h under N_2 atmosphere. The following day, the reaction mixture was warmed to 40 °C and vacuum-filtered through a fritted glass funnel with filter paper. The slightly turbid filtrate was concentrated under reduced pressure, then reconstituted in 300 mL fresh toluene and warmed to 40 °C. This process was repeated for a total of 3 filtrations. The transparent filtrate was concentrated under reduced pressure, then dissolved in 100 mL of toluene and precipitated with a large excess (800 mL) of anhydrous diethyl ether (dried

over magnesium sulfate). The slurry was centrifuged at 4400 rpm for 15 min, and the supernatant was discarded. The solid residue was rinsed twice with fresh diethyl ether, and then centrifuged. F127-DMA was recovered as a fluffy, white powder and was dried under ambient conditions for 12 h. Finally, powder was dried under reduced pressure at 40 °C for 24 h. Dry F127-DMA (29 g) was transferred to amber glass containers and stored at 5 °C. ^{1}H NMR spectroscopy indicated 94-96% functionalization of chain ends. ^{1}H NMR sample was prepared in deuterochloroform at concentrations of 20 mg / mL (Supporting information) and ^{1}H NMR spectra was collected on a Brüker Avance 500 MHz spectrometer. Pluronic F127 has average poly (propylene oxide) block lengths of DP = 69 and poly(ethylene oxide) block lengths of *DP* = 97 (total M_n = 12,500 g / mol). In all F127-DMA spectra, the methyl groups of the poly (propylene oxide) block were calibrated to (69 x 3) = 207. The degree of DMA functionalization (f_n) was estimated by dividing the integrated methacrylate vinyl and methyl protons, as well as the PEO chain-end methylene protons, by their theoretical values. For example, 1.90 (vinyl, actual) / 2 (vinyl, theoretical) x 100 ≈ 95% functionalization of chain ends. The degree of DMA-functionalization is reported as a range of estimates, from lowest to highest. ^{1}H NMR (500 MHz, $CDCl_3$, 298 K): δ = 6.12 (m, 2H, H-CH=C) 5.56 (m, 2H, H-CH=C) 4.29 (t, 3J = 4.9 Hz; 4H, $CH_2OC(O)$) 3.79-3.40 (m, 1001H, CH_2O, CH_3CHO) 1.93 (dd, 4J = 1.7 Hz, 4J = 0.9 Hz; 6H, $CH_3C(CO_2)=CH_2$) 1.12 (dd, 3J = 6.1 Hz, 4J = 4.4 Hz; 207H, CH_3CO). (FigureB1)

3.2.3 Preparation of hydrogel ink formulations

The weight percentages provided (supporting information) are based on the total composition of the hydrogel including the aqueous solvent. F127-DMA (1.25 g) was dissolved in 3.75 g of deionized (DI) water and cooled at 4 °C overnight to prepare 25 wt % F127-DMA hydrogel. Photo radical generator, 2-hydroxy-2-methylpropiophenone (5 μL), was added to the hydrogel and

vortexed, creating a homogenous solution. Then, the solution was allowed to equilibrate at 4 °C until bubbles were removed. Finally, the solution was warmed to room temperature to undergo a sol to gel transition, resulting in a shear-responsive gel. The same process was used to prepare the various 4 wt % and 10 wt % hydrogel ink formulations, with the additional step of replacing 0.2 g or 0.5 g of water with 0.2 g or 0.5 g of the additives, respectively. For example, 1.25 g F127-DMA and 0.5 g HEA were dissolved in 3.25 g DI water and cooled at 4 °C overnight to prepare the 10 wt % HEA formulation.

3.2.4 Rheological Characterization

For rheological characterization of the materials, dynamic oscillatory experiments were performed on a TA Instruments Discovery Hybrid Rheometer-2 (DHR-2) equipped with a peltier. The instrument operates by applying a known displacement (strain) and measuring the material's resistance (stress) to the force. Rheological tests were conducted by depositing hydrogel between the rheometer base plate and 20 mm parallel plate geometry at a gap of 1 mm unless otherwise mentioned. Samples were equilibrated in an ice bath for at least 30 min and then were carefully loaded onto the Peltier plate at 5 °C and a preshear experiment was applied to eliminate the bubbles from the sample. The sample was equilibrated at 21 °C for 8 min before each run. Viscosity versus shear rate experiments were performed under a shear rate increasing from 0.0001 to 50 s^{-1} then decreasing back to 0.0001 s^{-1} using a 40 mm cone and plate geometry with a cone angle of 1.019° using a solvent trap. Cyclic shear strain tests (frequency 1 Hz) were performed at 21 °C using alternating strains of 1% for 5 min and 100% for 3 min per cycle, to investigate the yielding and recovery behavior of the hydrogels. Temperature ramp experiments were performed at 1 Hz from 5−50 °C at 2 °C/min. Photo-curing was performed using a fully integrated smart swap LED photo

curing accessory. A 600 s irradiation with 365 nm light at 5 mW/cm^2 intensity was triggered into the experiment, and the sample was monitored for a total of 1020 s at 1% strain and at 1 Hz (n=3).

3.2.5 Preparation of tensile specimens

All hydrogel formulations were brought below their T_{gel} and poured into ASTM D638 type V specimen molds. Each specimen was then brought back to 21 ^{o}C to induce gelation. Upon complete gelation, the specimens were cured for 30 minutes in a custom-fabricated curing chamber with sunlite 365 nm A19 UV Lamps. To prevent evaporation, tensile specimens were stored alongside moist Kim wipes in centrifuge tubes until the mechanical tests were conducted.

3.2.6 Mechanical tests

Tensile mechanical measurements were performed on as-prepared tensile specimens using an Instron 5585H load frame with a 50 N load cell and flat pneumatic grips. All tests were conducted using a crosshead rate of 10mm/min, until specimen failure. The dimensions of each specimen were measured with calipers prior to testing to ensure accurate calculation of stress and strain. At least five specimens of each formulation were tested. The Young's moduli were calculated from the linear region of stress vs strain curve.

3.2.7 Printing of hydrogel inks

All the polymer formulations were loaded into 10 ml syringes fitted with a barrel-shaped size 22 Metcal extrusion nozzle (410 µm I.D.) and allowed to equilibrate to the surrounding temperature of 21 °C before printing. The printing was performed on a Prusa I3 RepRap printer, where each ink printed single layered filament (n=3). This was photo-polymerized by UV irradiation for 60 s and then imaged with Nikon Eclipse E600 Pol fitted with a Optix Cam camera**.** The filament

diameter and analysis were done using ImageJ software. All CAD models were designed in Solidworks 2016. All printing was done using with printing parameters as mentioned later. The tip of the needle was positioned at a designated point on the support gel holder that served as the XYZ origin for all prints. Printing was controlled through standard 3DP software to generate G-code commands (Slic3r) from CAD-generated (Solidworks).

3.3 Results and Discussion

3.3.1 Flow behavior and rheological characterization of the polymer compositions

Figure 3.1 shows the general scheme to formulate and direct-write 3D print with the hydrogel inks. The reversible temperature response of the hydrogel allows facile incorporation of additives to the solution-phase of the aqueous mixture at temperatures below its gelation temperature (T_{gel}) where the aqueous mixtures of F127-DMA behave as a solution. The shear-thinning property of the inks enable their extrusion through the nozzle with applied pressure. Irradiation with 365 nm light initiates photo-polymerization of the reactive monomers to cross-link the hydrogel, and effectively turn off the shear-thinning response. We chose water-soluble, photo-polymerizable monomers as additives, such as acrylic acid (AA), 2-hydroxyethyl acrylate (HEA), 2-(dimethylamino) ethyl methacrylate (DMAEMA) and poly(ethylene glycol) diacrylate (PEG-DA), which can undergo *in situ* photo-copolymerization of the methacrylate end-groups of F127-DMA with the reactive monomer additives. The additives were included as either 4 or 10 wt% of the total hydrogel composition.

A temperature ramp experiment was performed for each of the samples to characterize the thermo-responsive behavior of the materials (Supporting Information). The T_{gel} is represented by the cross-over point between the storage (G') and loss moduli (G"). All of the formulations

exhibited a temperature-dependent sol-gel transition, although the value for the T_{gel} changed with the quantity and the composition of the additive (Table 1). The values for the T_{gel} ranged from 7.5 to 17.5 °C.

Rheological experiments such as viscosity versus shear rate and cyclic shear strain (Supporting Information) were used to probe the differences in the viscoelastic responses of the inks under conditions representative of 3D printing. For extrusion-based 3D printing of hydrogel inks, shear-thinning materials are often favored since they undergo a substantial reduction in viscosity under shear stress. All formulations showed similar shear-thinning behavior, wherein the viscosity decreased by almost three orders of magnitude as the shear rates increased from 0.01 s^{-1} to 100 s^{-1} (Supporting information). This feature is important to ensure the smooth flow of hydrogels from a nozzle during direct-write 3D printing. In the cyclic shear strain experiment, periods of high strain emulated the shear forces the inks experienced as they were extruded through a nozzle and the subsequent period of low strain represented the ink after it exited the nozzle. Alternating periods of low amplitude strain of ~ 1% and high amplitude strain of ~ 100% were applied on each sample for 5 mins and 3 mins, respectively for five cycles (Figure 3.2). All the samples showed a sharp decrease in moduli under high strain and recovered within 4 s upon relief from that strain. The hydrogel displayed minimal hysteresis between strain cycles, which suggests that the hydrogel inks can rapidly reform the physical cross-links between the polymer chains that provide the mechanical stability of the hydrogel. Even after several cycles, the yielding and recovery behavior of the materials did not appreciably change, which suggested that the hydrogel inks were suitable for direct-write printing processes wherein the flow of the ink is turned “on” and “off ”.

3.3.2 Evaluation of Ink Printability

Given that all the hydrogel ink formulations were temperature responsive and shear-thinning, we next sought to correlate the printability of the hydrogel inks to rheometrical differences. The critical printing parameters, which included the pressure exerted onto the gel in the syringe, the printing speed (the rate at which the nozzle moves across the surface), and the temperature of the printing environment, were kept constant at 20 psi, 5 mm/s and 21 °C, respectively. Each of the inks was tested for printability by extruding the ink through a 410 μm I.D. nozzle. If there was a significantly large deviation from this value, then the hydrogel ink is not ideal for direct-write 3D printing. Filaments were extruded and analyzed with an optical microscope for differences in shape or diameter. "Printable" filaments were defined as those that produced continuous, tubular filaments with diameters close to the actual nozzle diameter. To define the error in printability, a term ε was defined using the equation:

$$\varepsilon = \frac{D_{fiber} - D_{nozzle}}{D_{nozzle}} \times 100 \qquad (3)$$

where D_{fiber} and D_{nozzle} are the measured diameter of the printed fiber and diameter of the nozzle, respectively (Table 3.1).

Since that the hydrogel formulations in this study were shear-thinning, their flow behavior was approximated by the Hershel-Bulkley equation given by:

$$\sigma = \sigma_{dyn} + \mathrm{K}\dot{\gamma}^{\mathrm{n}} \qquad (4)$$

Where $\dot{\gamma}$ is the shear rate, K is the consistency index and n is the flow index. A plot of stress vs. shear rate shows a good fit to the model (R^2 = 0.99467, Supplemental Information). As shown in Figure 3.3, the yield stresses were determined from the plot of shear stress versus shear rate,

wherein the shear history of a hydrogel ink undergoing extrusion is simulated in the rheometer. An increasing shear stress was applied until the material yielded, after which the shear rate was reduced allowing the material to relax until it stopped flowing. The σ_{stat} was measured from the change in the slope of the stress from the first part of the loop (increasing shear rate) while the σ_{dyn} was measured from the y-intercept ($\dot{\gamma} = 0\ s^{-1}$) of the same plot under decreasing shear rate. We observed that some materials produced filaments which were much larger in size than the nozzle diameter while others showed minimal deviation. The σ_{dyn} values of the material closely matched their trend in printability. This indicated that of the materials investigated, the ones with a higher dynamic shear stress retained the filament shape and diameter more uniformly after extrusion. The native ink F127-DMA had better filament resolution at higher concentrations (30 wt %, ε= 7.3 %) in contrast to the filament diameter of the 25 wt % hydrogel. (ε= 186.6 %). Upon addition of the functional monomers, the printability of the Pluronic hydrogel changed significantly (Figure 3.4). For example, a grid structure printed with 30 wt % F127-DMA showed good printability (~ 446 ± 10 μm) with good resolution in contrast to the hydrogel formulation with the AA additive (10 wt %), which had very broad extruded filaments (~ 750 ± 15 μm). The DMAEMA (10 wt %) containing hydrogel formulation had smaller diameter filaments (~ 270 ± 10 μm) under the same printing conditions. In addition to viscosity, the monomers also exhibited considerable influence upon the yield stresses of the material. The addition of DMAEMA in different proportions increased the σ_{dyn} of the ink. The protic AA monomer also showed similar trends, but to a much lesser degree than the aprotic DMAEMA. On the other hand, HEA (10 wt %) behaved very similarly to the native 25 wt % F127-DMA, whereas HEA (4 wt %) caused the σ_{dyn} to decrease significantly. The addition of PEGDA monomers afforded an unexpected behavior. The formulation with lower PEGDA content (4 wt %) exhibited a reduction in σ_{dyn} while PEG-DA

(10 wt %) was much stiffer with very high σ_{dyn} and showed high fidelity to the nozzle diameter (ε= 1.7 %). The cumulative set of results with the addition of these additives suggested that a σ_{dyn} value of ca. 300 Pa affords hydrogel filaments that correspond well to the I.D. of the nozzle.

It is, however, important to distinguish between the two parameters (σ_{stat} and σ_{dyn}) and their relationship to the hydrogel ink printability. Although the values of σ_{stat} and σ_{dyn} can be similar (Table 3.1 and Table 3.2) for our shear-thinning hydrogels, the static yield stress should dictate the extrusion pressure, while the σ_{dyn} should determine the quality of the filament shape. For example, HEA (10 wt %) exhibited a lower yield stress (270 Pa) relative to the other formulations, and therefore, required less pressure (12 psi) to extrude the filament. At the same time, this HEA formulation also retained filament fidelity (relative to the nozzle I.D.) (ε = 12.15 %) as a consequence of its moderately good dynamic stress 250 Pa. The quality of the extruded filament decreased as the extrusion pressure was increased, which further demonstrates that extrusion pressure is an important parameter in direct-write 3D printing.

The reason behind the differences of the printability and the yield stresses due to the addition of monomers has yet to be fully elucidated. We hypothesize that the polarity and hydrogen bonding capability may be important parameters. Alexandridis *et. al.*[42,43] has also shown that the addition of co-solvents can alter the micelle formation of Pluronics in water by partitioning into different blocks of the macromolecule.[44] The co-solvents may cause local dehydration effects and changes in micelle packing that are comparable to those induced by changes in temperature. The extent and direction in which the co-solvents change the self-assembly behavior depends on the polarity of the added solvents. The differences in polarity of the additives used in this study may be causing the differences in material properties, and further investigations are underway to delineate the origins of these affects.

The optimized filament resolution for each of the formulations are listed in Table 3.2. These results were obtained by controlling print speed and extrusion pressure during the printing of a hydrogel ink (at 21 °C). The extrusion pressure is defined as the minimum pressure to extrude a smooth and continuous filament from a nozzle and was varied from 0 to 20 psi. For hydrogel materials, a minimal printing time is desired to minimize dehydration of the printed filaments over time. The printing speed in this study was varied between 2 to 25 mm/s. Table 3.2 also shows the static yield stresses along with the filament diameter produced by the different hydrogel inks. Extrusion pressure and print speed are not mutually independent, and a higher extrusion pressure can be offset by a faster print speed. However, a closer examination of the extruded filaments under an optical microscope (Figure 3.5), showed that a higher extrusion pressure and print speed yielded filaments with non-uniform diameters due to uneven extrusion or jetting. For example, when 30% F127-DMA is printed at a lower print speed (5 mm/s), the filament obtained is smoother and more uniform than printing at 10 mm/s which afforded filaments with a variable width (~270 μm). A static yield stress greater than 450 Pa could not be extruded at 20 psi, which was the maximum pressure available for the direct-write 3D printer.

3.3.3 Rheometrical and tensile characterization of crosslinked hydrogel ink formulations

The mechanical properties of the hydrogel formulations after the photo-initiated cross-linking was investigated by performing *in situ* UV curing rheometrical experiments. The storage modulus was recorded prior to, during, and after UV irradiation (Figure 6). The 25 wt % F127-DMA had a storage modulus of 143 kPa after curing. The storage modulus of the various PEG-DA formulations increased with increasing concentration of PEG-DA, ranging from 134 kPa to 429 kPa for 6 wt % to 20wt% PEG-DA, respectively. This drastic increase in storage moduli suggests that bis-functionalized PEG-DA increased the crosslinking density of the hydrogel.[45] Conversely,

the storage modulus of each of the DMAEMA formulations decreases with increasing additive concentration, 100 kPa and 73 kPa for 4 wt % and 10 wt %, respectively. For the HEA and AA formulations, the storage modulus does not depend on the additive concentration and the equilibrium storage modulus after crosslinking is about 140 kPa and 130 kPa, respectively.

Figure 3.6 shows the change in storage modulus of the various hydrogel ink formulations as they undergo UV irradiation (N=3)

The chemical structure of the different additives also influences the rate of polymerization. The monomers with acrylate groups (HEA, AA, and PEG-DA) all reach maximum storage modulus during UV irradiation faster than monomers with methacrylate groups (DMAEMA) and F127-DMA alone. Upon 290 s of UV irradiation, F127-DMA reached its maximum storage modulus, while HEA and AA formulations reach equilibrium storage moduli within 15 s, and PEG-DA formulations within 35 s. DMAEMA formulations required a longer time period (394 s or 410 s for 4 wt % or 10 wt %, respectively) to reach their maximum storage moduli, likely a consequence of the slower reactivity of methacrylates.[46]

The elongation at break, ultimate tensile strength, and Young's modulus of the hydrogel ink formulations are summarized in Figure 3.7. The addition of PEG-DA increased the tensile strength and Young's modulus of F127-DMA. These two parameters increased with increasing amount of PEG-DA, with the maximum change in strength and Young's modulus coming from the 10 wt % PEG-DA formulation (240 % and 366 %, respectively) compared to native 25 wt % F127-DMA. However, as the concentration of PEG-DA was increased, the elongation at break decreased significantly (88 % for 10 wt % PEG-DA versus 237 % for native 25 wt % F127-DMA). The Young's moduli and ultimate tensile strength for AA and DMAEMA formulations remained unchanged in comparison to native 25 wt % F127-DMA. For HEA formulations, the stiffness and

tensile strength increased with increasing concentration of monomer. The elongation at break was improved by 35 %, 41 %, and 43 % for 10 wt % HEA, AA, and DMAEMA, respectively. Thus, these results reveal that the additives can serve an important role in modifying the mechanical properties of the cross-linked hydrogels.

3.4. CONCLUSION

In this report, several hydrogel inks were formulated by the addition of reactive monomers, which included acrylic acid, 2-*N*, *N*-dimethylaminoethyl methacrylate, 2-hydroxyethyl acrylate, and poly (ethylene glycol) diacrylate to F127-DMA hydrogels. The printability of the resulting hydrogel inks prior to photo-polymerization, and the mechanical properties of the ink after photo-polymerization, were investigated. Prior to UV irradiation, the two critical rheological parameters that correlate to printability were the dynamic and the static yield stress. Materials with low dynamic yield stress, below 200 Pa, are not promising candidates for direct-write printing, as they do not retain their shape well enough to form a filament upon extrusion. On the other hand, we observed that there was a correlation between the static yield stress and the pressure required to extrude the hydrogel ink from a 410 μm I.D. nozzle. At a printing pressure of 20 psi, the maximum value for the static yield stress that still afforded a smooth and continuous hydrogel filament was 450 Pa. Finally, we demonstrated that the monomer additives were covalently incorporated into the cross-linked hydrogels and had a significant affect upon the mechanical properties of the resulting hydrogels. The results of these findings can serve as a guide to the development of new functional shear-thinning hydrogel inks for direct-write 3D printing.

3.5 REFERENCES

1. Naficy, S.; Gately, R.; Gorkin, R.; Xin, H.; Spinks, G. M. 4D Printing of Reversible Shape Morphing Hydrogel Structures.*Macromol.Mater.Eng.* **2017**, 302, 413-419.
2. Bakarich, S. E.; Gorkin, R.; Panhuis, M. in het; Spinks, G. M. 4D Printing with Mechanically Robust, Thermally Actuating Hydrogels. *Macromol. Rapid Commun.* **2015**, *36*, 1211–1217.
3. Murphy, S. V.; Atala, A. 3D Bioprinting of Tissues and Organs. *Nat Biotech.* **2014**, 32, 773–785
4. Martin, I.; Simmons, P. J.; Williams, D. F. Manufacturing Challenges in Regenerative Medicine. *Sci.Trans. Med.* **2014**, *6*, 232.
5. Guvendiren, M.; Lu, H. D.; Burdick, J. A. Shear-Thinning Hydrogels for Biomedical Applications. *Soft Matter* **2012**, *8*, 260–272.
6. (a) Sun, K.; Wei, T.-S.; Ahn, B. Y.; Seo, J. Y.; Dillon, S. J.; Lewis, J. A. 3D Printing of Interdigitated Li-Ion Microbattery Architectures. *Adv. Mater.* **2013**, 25, 4539–4543. (b) Wu, W.; DeConinck, A.; Lewis, J. A. Omnidirectional Printing of 3D Microvascular Networks. *Adv. Mater.* **2011**, 23, H178–H183.
7. Maiti, A.; Small, W.; Lewicki, J. P.; Weisgraber, T. H.; Duoss, E. B.; Chinn, S. C.; Pearson, M. A.; Spadaccini, C. M.; Maxwell, R. S.; Wilson, T. S. *Sci. Rep*. **2016**, 6 (1), 24871.
8. Lee, K. Y.; Mooney, D. J. Alginate: Properties and Biomedical Applications. *Prog Polym Sci* **2012**, *37*, 106–126.
9. Wu, Z.; Su, X.; Xu, Y.; Kong, B.; Sun, W.; Mi, S. Bioprinting Three-Dimensional Cell-Laden Tissue Constructs with Controllable Degradation. *Scientific Reports* **2016**, *6*, 24474.
10. Su, B.; Zhang, D.; Button, T. W. Micropatterning of Fine Scale Ceramic Structures. *J. Mater. Sci*, **2002**, *37*, 3123–3126.
11. Gratson, G. M.; Xu, M.; Lewis, J. A. Microperiodic Structures: Direct Writing of Three-Dimensional Webs. *Nature* **2004**, *428*, 386–386.
12. Smay, J. E.; Cesarano, J.; Tuttle, B. A.; Lewis, J. A. Directed Colloidal Assembly of Linear and Annular Lead Zirconate Titanate Arrays. *J. Am. Ceram. Soc.* **2004**, *87*, 293–295.
13. Billiet, T.; Vandenhaute, M.; Schelfhout, J.; Van Vlierberghe, S.; Dubruel, P. A Review of Trends and Limitations in Hydrogel-Rapid Prototyping for Tissue Engineering. *Biomaterials* **2012**, *33*, 6020–6041.
14. Truby, R. L.; Lewis, J. A. Printing Soft Matter in Three Dimensions. *Nature* **2016**, *540*, 371–378.
15. Sinha, G. Cell Presses. *Nat. Biotech.* **2014**, *32*, 716–719.
16. Derby, B. Printing and Prototyping of Tissues and Scaffolds. *Science* **2012**, *338*, 921–926.
17. Kang, H.-W.; Lee, S. J.; Ko, I. K.; Kengla, C.; Yoo, J. J.; Atala, A. A 3D Bioprinting System to Produce Human-Scale Tissue Constructs with Structural Integrity. *Nat. Biotech.* **2016**, *34*, 312–319.
18. Duan, B.; Hockaday, L. A.; Kang, K. H.; Butcher, J. T. 3D Bioprinting of Heterogeneous Aortic Valve Conduits with Alginate/Gelatin Hydrogels. *J Biomed. Mater. Res. A* **2013**, *101*, 1255–1264.

19. Sundaram, S.; Kim, D. S.; Baldo, M. A.; Hayward, R. C.; Matusik, W. 3D-Printed Self-Folding Electronics. *ACS Appl. Mater.Interfaces* **2017**, 32290–32298.
20. Russo, A.; Ahn, B. Y.; Adams, J. J.; Duoss, E. B.; Bernhard, J. T.; Lewis, J. A. Pen-on-Paper Flexible Electronics. *Adv. Mater.* **2011**, *23*, 3426–3430.
21. Shi, Y.; Pan, L.; Liu, B.; Wang, Y.; Cui, Y.; Bao, Z.; Yu, G. Nanostructured Conductive Polypyrrole Hydrogels as High-Performance, Flexible Supercapacitor Electrodes. *Journal of Materials Chemistry A* **2014**, *2*, 6086–6091.
22. Biondi, M.; Ungaro, F.; Quaglia, F.; Netti, P. A. Controlled Drug Delivery in Tissue Engineering. *Adv. Drug Deliv. Rev.* **2008**, *60*, 229–242.
23. Lee, Y.-J.; Braun, P. v. Tunable Inverse Opal Hydrogel pH Sensors. *Adv. Mater.* **2003**, *15* (7–8), 563–566.
24. Holtz, J. H.; Asher, S. A. Polymerized Colloidal Crystal Hydrogel Films as Intelligent Chemical Sensing Materials. *Nature* **1997**, *389*, 829–832.
25. Hinton, T. J.; Jallerat, Q.; Palchesko, R. N.; Park, J. H.; Grodzicki, M. S.; Shue, H.-J.; Ramadan, M. H.; Hudson, A. R.; Feinberg, A. W. Three-Dimensional Printing of Complex Biological Structures by Freeform Reversible Embedding of Suspended Hydrogels. *Sci. Adv.* **2015**, *1*, e1500758
26. Müller, M.; Becher, J.; Schnabelrauch, M.; Zenobi-Wong, M. Nanostructured Pluronic Hydrogels as Bioinks for 3D Bioprinting. *Biofabrication* **2015**, *7*, 035006.
27. Custódio, C. A.; Reis, R. L.; Mano, J. F. Photo-Cross-Linked Laminarin-Based Hydrogels for Biomedical Applications. *Biomacromolecules* **2016**, *17*, 1602–1609.
28. Highley, C. B.; Rodell, C. B.; Burdick, J. A. Direct 3D Printing of Shear-Thinning Hydrogels into Self-Healing Hydrogels. *Adv. Mater.* **2015**, *27*, 5075–5079.
29. Lee, K. Y.; Mooney, D. J. Alginate: Properties and Biomedical Applications. *Prog. Polym. Sci.* **2012**, *37*, 106–126.
30. (a)Zhang, M., Vora, A., Han, W., Wojtecki, R.J., Maune, H., Le, A.B.A., Thompson, L.E., McClelland, G.M., Ribet, F., Engler, A.C., Nelson, A. Dual-Responsive Hydrogels for Direct-Write 3D Printing. *Macromolecules* **2015**, *48*, 6482–6488. (b) Karis, D. G.; Ono, R. J.; Zhang, M.; Vora, A.; Storti, D.; Ganter, M. A.; Nelson, A. Cross-Linkable Multi-Stimuli Responsive Hydrogel Inks for Direct-Write 3D Printing. *Polym. Chem.* **2017**, *8* (29), 4199–4206.
31. Schmolka, I. R. Artificial Skin I. Preparation and Properties of Pluronic F-127 Gels for Treatment of Burns. *J. Biomed. Mater. Res.* **1972**, *6* (6), 571–582.
32. Kabanov, A. V.; Batrakova, E. V.; Alakhov, V. Y. Pluronic® Block Copolymers as Novel Polymer Therapeutics for Drug and Gene Delivery. *J. Control. Release* **2002**, *82*, 189–212.
33. Müller, M.; Becher, J.; Schnabelrauch, M.; Zenobi-Wong, M. Printing Thermoresponsive Reverse Molds for the Creation of Patterned Two-Component Hydrogels for 3D Cell Culture. *J. Vis. Exp.* **2013**, *77*, e50632.
34. Mortensen, K.; Talmon, Y. Cryo-TEM and SANS Microstructural Study of Pluronic Polymer Solutions. *Macromolecules* **1995**, *28*, 8829–8834.
35. París, R.; Quijada-Garrido, I. Temperature- and pH-Responsive Behaviour of poly(2-(2-Methoxyethoxy) ethyl Methacrylate-Co-N,N-Dimethylaminoethyl Methacrylate Hydrogels. *Eur. Polym. J.* **2010**, *46*, 2156–2163.
36. Fussell, G. W.; Cooper, S. L. Endothelial Cell Adhesion on RGD-Containing Methacrylate Terpolymers. *J. Biomed. Mater. Res.* **2004**, *70A*, 265–273.

37. He, Y.; Yang, F.; Zhao, H.; Gao, Q.; Xia, B.; Fu, J. Research on the Printability of Hydrogels in 3D Bioprinting. *Sci. Rep.* **2016**, *6*, 29977.
38. Suntornnond, R.; Tan, E. Y. S.; An, J.; Chua, C. K. A Mathematical Model on the Resolution of Extrusion Bioprinting for the Development of New Bioinks. *Materials*, **2016**, *9*,756.
39. M'Barki, A.; Bocquet, L.; Stevenson, A. Linking Rheology and Printability for Dense and Strong Ceramics by Direct Ink Writing. *Sci. Rep.* **2017**, *7*, 6017.
40. Deepa, G.; Thulasidasan, A. K. T.; Anto, R. J.; Pillai, J. J.; Kumar, G. V. Cross-Linked Acrylic Hydrogel for the Controlled Delivery of Hydrophobic Drugs in Cancer Therapy. *Int. J. Nanomedicine* **2012**, *7*, 4077–4088.
41. Xu, F.-J.; Kang, E.-T.; Neoh, K.-G. pH- and Temperature-Responsive Hydrogels from Crosslinked Triblock Copolymers Prepared via Consecutive Atom Transfer Radical Polymerizations. *Biomaterials* **2006**, *27*, 2787–2797.
42. Alexandridis, P.; Ivanova, R.; Lindman, B. Effect of Glycols on the Self-Assembly of Amphiphilic Block Copolymers in Water. 1. Phase Diagrams and Structure Identification. *Langmuir* **2000**, *16*, 3676–3689.
43. Kaizu, K.; Alexandridis, P. Glucose-Induced Sphere to Ellipsoid Transition of Polyoxyethylene–polyoxypropylene Block Copolymer Micelles in Aqueous Solutions. *Colloids Surf A: Physicochemical and Engineering Aspects* **2015**, *480*, 203–213.
44. Alexandridis, P.; Yang, L. SANS Investigation of Polyether Block Copolymer Micelle Structure in Mixed Solvents of Water and Formamide, Ethanol, or Glycerol. *Macromolecules* **2000**, *33*, 5574–5587.
45. Son, K.H.; Lee, J.W. Synthesis and Characterization of Poly(Ethylene Glycol) Based Thermo-Responsive Hydrogels for Cell Sheet Engineering. *Materials* **2016**, *9*, 854.
46. Odian, G. G. *Principles of polymerization*; Wiley-Interscience: Hoboken, NJ, 2004.

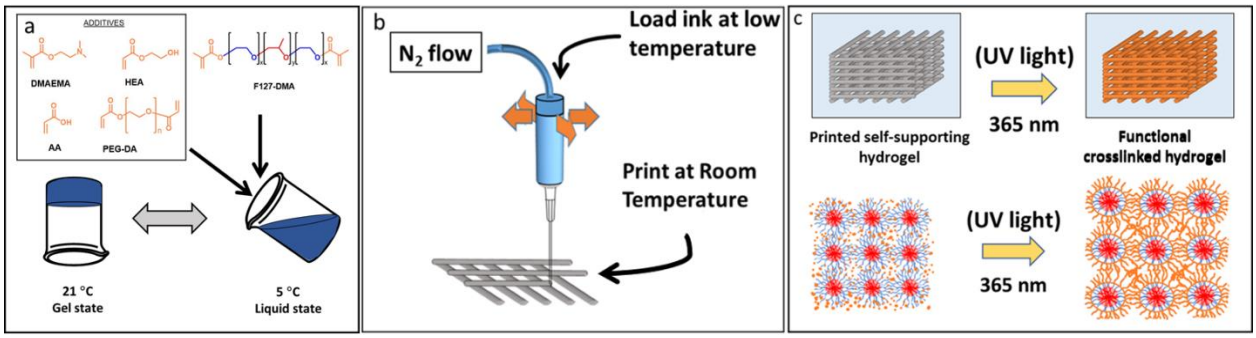

Figure 3.1: Scheme of ink preparation for DIW 3D printing: (a) Additives are incorporated into F127-DMA in its sol state, and then transferred into a syringe where it becomes a gel at 21 °C. (b) Nitrogen gas is used to pressurize the syringe to dispense the shear-thinning hydrogel ink from a nozzle at 21 °C. (c) The printed structure is irradiated with 365 nm light to induce *in-situ* co-polymerization of F127-DMA and the additives

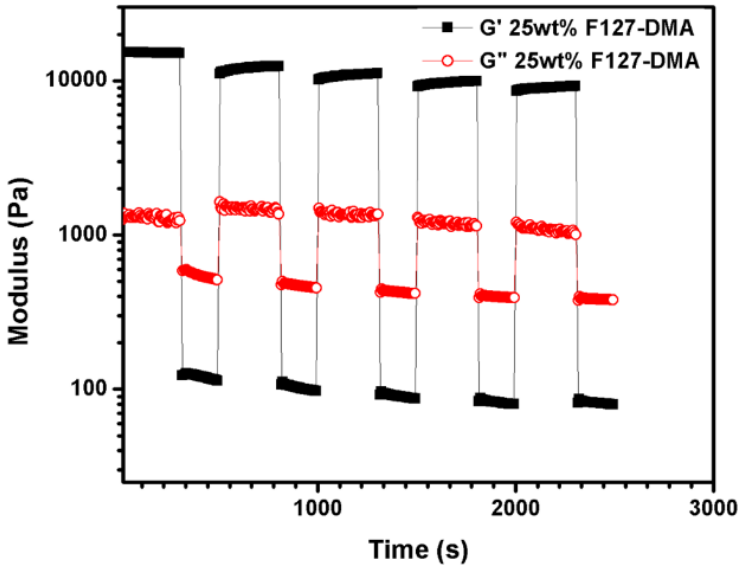

Figure 3.2: Cyclic shear thinning plot of F127-DMA over time.

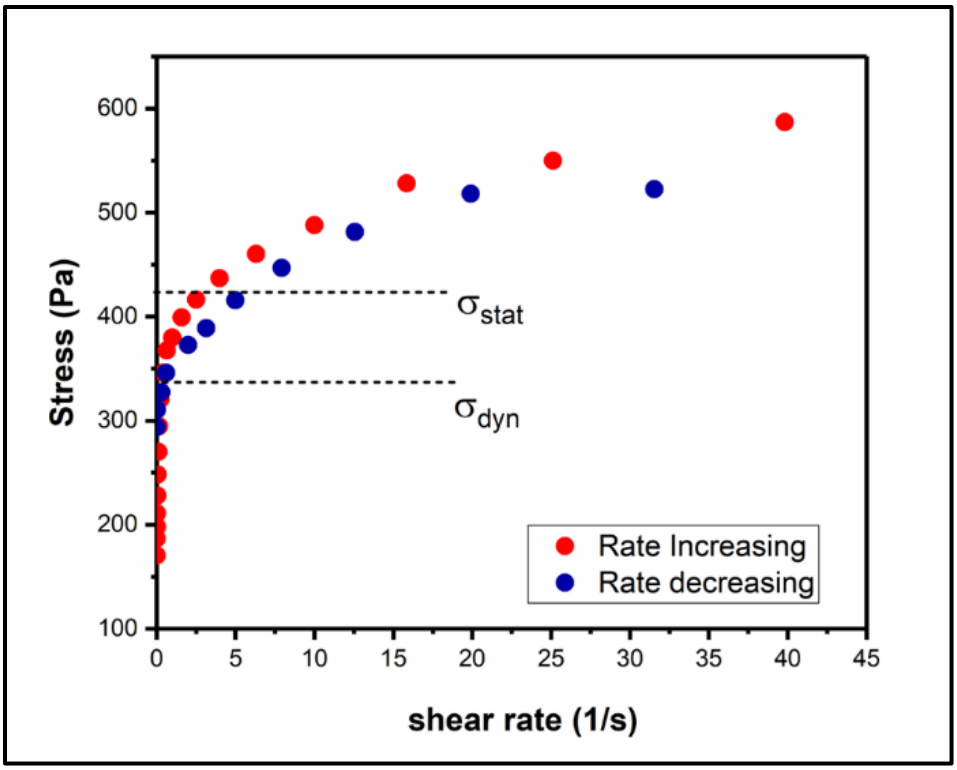

Figure 3.3: A stress versus shear rate plot showing the stress history of a 30 wt % F127-DMA hydrogel when extruding a filament. The shear rate was increased until the material yielded (σ_{stat}), after which the shear rate was decreased to zero (σ_{dyn}). The static yield stress was obtained from the onset of the slope change while the shear rate was increased, while the dynamic yield stress was obtained from the y-intercept of the plot when shear rate was decreased.

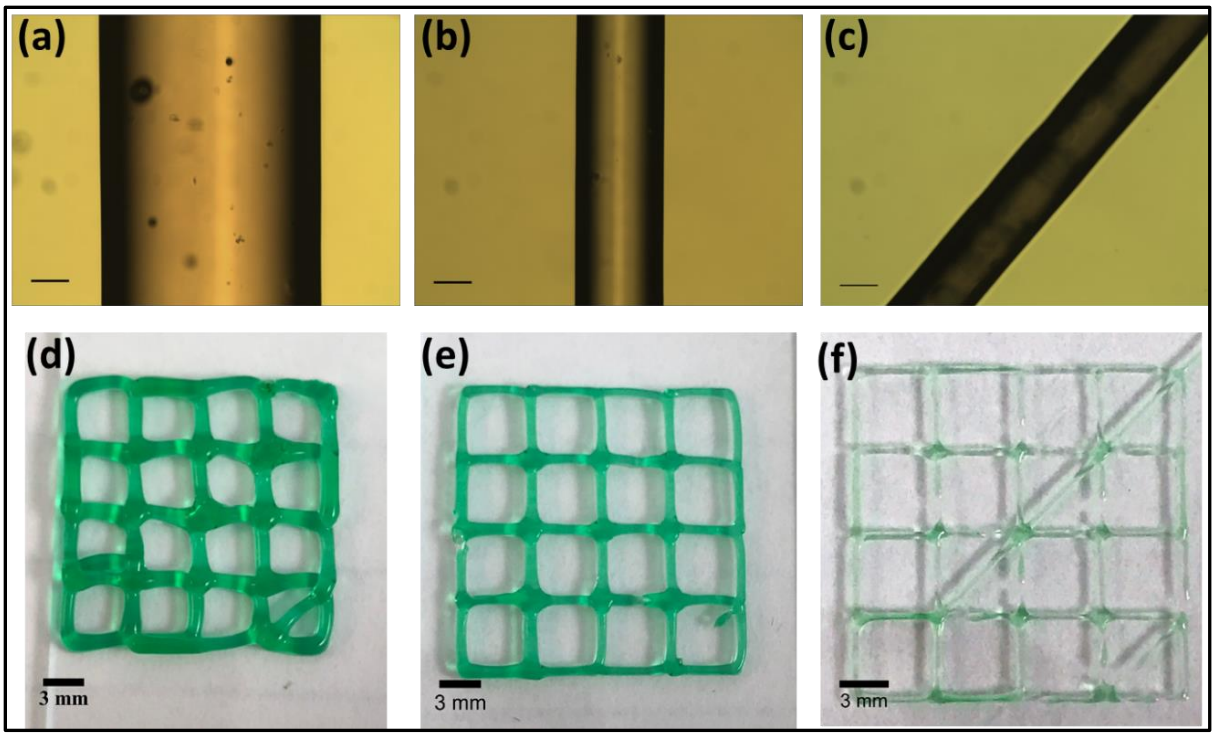

Figure 3.4: Filaments and grids printed at 20 psi and 5mm/s showing different rates of extrusion for (a) AA (10), (b) 30% F127-DMA, and (c) DMAEMA (10) under an optical microscope (scalebar represents 200 μm). Optical photographs of printed grid structures for (d) AA (10), (e) 30% F127-DMA, and (f) DMAEMA (10).

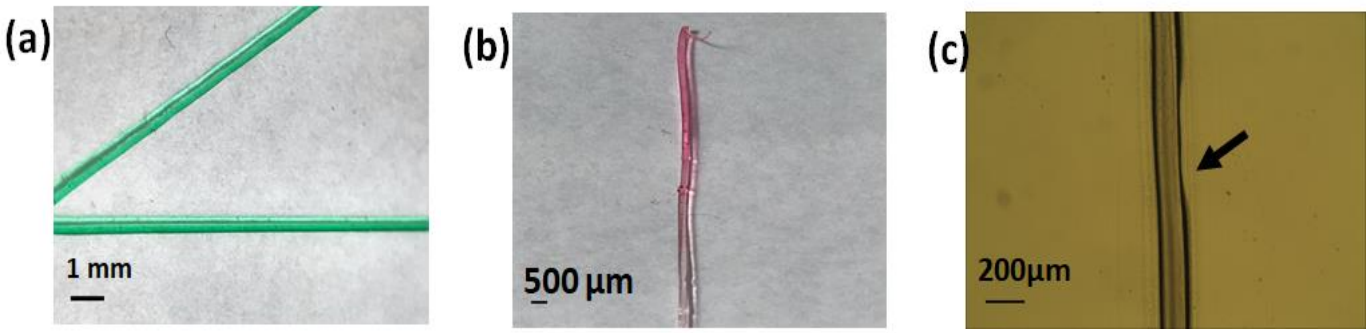

Figure 3.5: 30% F127-DMA extruded at different print speeds, (a) 5mm/s and (b, c) 10 mm/s.

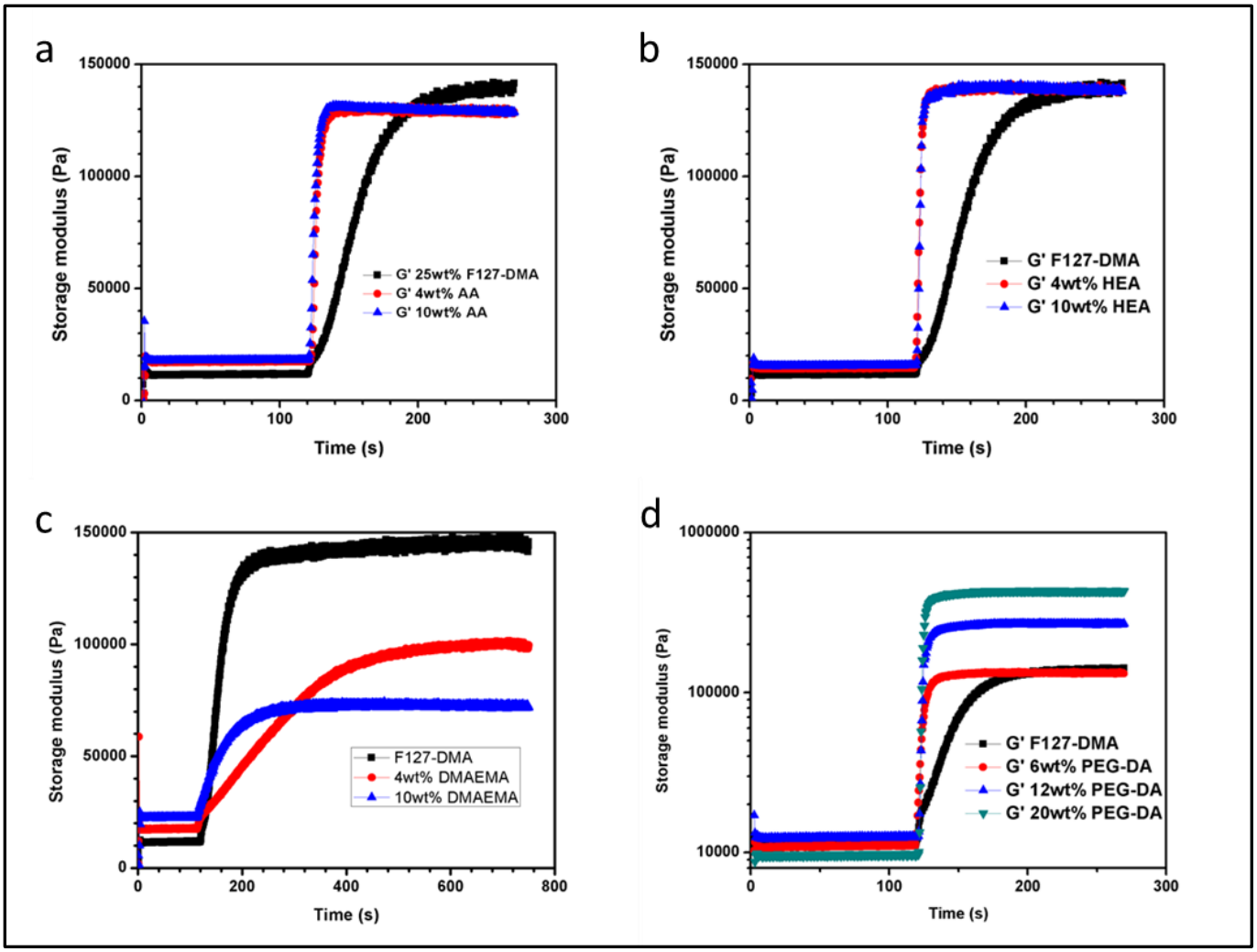

Figure 3.6: (a-d) Dynamic oscillatory UV cure experiments performed at 21 ° C showing an increase in storage modulus when the lamp is turned on 120 s after the start of the experiment for a total irradiation time of 600 s. (a) 25 wt % F127-DMA, AA (4), and AA(10) (b) 25 wt % F127-DMA, HEA (4), and HEA (10) (c) 25 wt % F127-DMA, DMAEMA (4), and DMAEMA (10) and (d) 25 wt % F127-DMA, PEG-DA (6), PEG-DA (12), and PEG-DA (20).

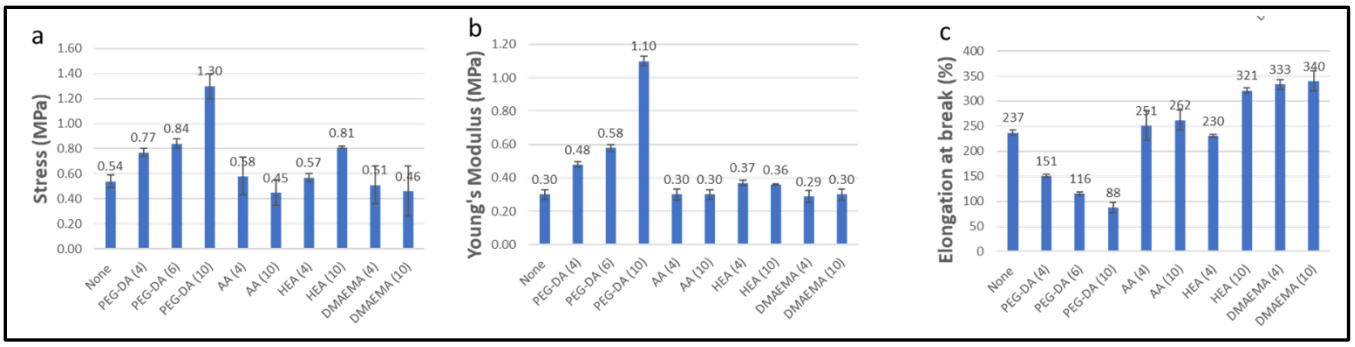

Figure 3.7: Plots that summarize the (a) tensile strength, (b) Young's modulus, and (c) elongation at break for the hydrogel ink formulations.

Polymer 1 (wt %)	**Additive (wt %)**	**Filament diameter (µm)**	σ_{DYN} **(Pa)**	**ε (%)**	**T_{Gel} (°C)**
F127-DMA (30)	-	430 ± 15	322.70	4.87	13.9
F127-DMA (25)	-	1176 ± 20	224.64	186.83	16.2
F127-DMA (25)	PEG-DA (10)	410 ± 10	417.02	2.44	15.2
F127-DMA (25)	PEG-DA (4)	N/A [a]	179.39	N/A	14.6
F127-DMA (25)	DMAEMA (10)	415 ± 10	365.90	3.65	7.5
F127-DMA (25)	DMAEMA (4)	450 ± 10	313.66	9.75	14.2
F127-DMA (25)	AA (10)	735 ± 15	260.54	79.26	12.2
F127-DMA (25)	AA (4)	909 ± 5	236.74	121.70	14.2
F127-DMA (25)	HEA (10)	1150 ± 30	251.04	180.49	15.9
F127-DMA (25)	HEA (4)	N/A [a]	8.18	N/A	15.1

Table 3.1: Hydrogel formulations and filament diameters printed at 20 psi and 5 mm/s at 21 ° C where σ_{dyn} is the dynamic yield stress of the material and ε is the deviation from the nozzle size.

[a] A filament could not be extruded with this formulation at the given temperature.

Polymer 1 (wt %)	**Additive (wt %)**	**σ_{STAT} (Pa)**	**Pressure (psi)**	**Print speed (mm/s)**	**Filament Diameter (µm)**
F127-DMA (30)	-	394.14	20	5	440 ± 5
F127-DMA (25)	-	224.64	15	20	770 ± 25
F127-DMA (25)	PEG-DA (10)	454.18	20	3	410 ± 20
F127-DMA (25)	PEG-DA (4)	194.13	12	20	N/A
F127-DMA (25)	DMAEMA (10)	414.01	20	3	415 ± 10
F127-DMA (25)	DMAEMA (4)	356.98	20	5	468 ± 20
F127-DMA (25)	AA (10)	260.55	15	10	510 ± 20
F127-DMA (25)	AA (4)	286.82	15	5	530 ± 30
F127-DMA (25)	HEA (10)	270.60	12	20	471 ± 15
F127-DMA (25)	HEA (4)	17.30	12	20	N/A

Table 3.2: Rheological properties and optimized printing conditions for each hydrogel ink formulation that afforded the best filament resolution.

CHAPTER 4: **MECHANOCHROMIC COMPOSITE ELASTOMERS FOR ADDITIVE MANUFACTURING AND LOW STRAIN MECHANOPHORE ACTIVATION**

4.1 ABSTRACT

Herein, we report a strategy for additive manufacturing of a mechanochemically active polydimethylsiloxane (PDMS) system primarily comprised of PDMS microbeads. Extruded, stable structures of cured microbeads were held together with a "bridging material" comprising uncured PDMS and spiropyran in a water medium. The spiropyran derivative did not degrade during the printing process. After thermal curing, the material displays repeatable and reversible mechanochromic activity. The extruded composite displays chromophore activation at lower mechanical strains under uniaxial tension (60-70%) than in a film without the microbeads (130-140%). The composite was employed in extrusion based direct writing to fabricate a variety of objects that displayed mechanochromic activity.

4.2 INTRODUCTION

Three-dimensional printing (3DP) has gained prominence in the last decade as an effective, low-cost method of prototyping for a variety of applications[1]. Recently, the merger of commercially available 3DP technologies and increasingly functional polymeric filaments have given rise to promising potential 3DP applications including bioprinting tissues and organs,[2,3] drug-delivery,[4] and materials for energy storage.[5] Nozzle extrusion remains among the most widely used 3DP technique and can be used to print materials ranging from thermoplastics to metals.[6,7] It remains challenging to extrude elastomeric materials, however, as their precursors are usually liquids under ambient conditions and their viscosities are too low for additive stacking strategies. Polydimethylsiloxane (PDMS), for example, is of interest for 3DP applications as it has favorable mechanical properties and optical clarity and is often used in biomedical applications, but its commercially available synthetic precursors are not suitable for direct ink writing.[8,9] Recently, Roh and coworkers reported that a dispersion of PDMS microbeads in a secondary PDMS matrix that offers a promising strategy for 3DP of PDMS.[8] The "ink" comprises a high ratio of cured PDMS microbeads to uncured PDMS precursor, which is dispersed in water to form a thixotropic granular paste that can be extruded into discrete objects. The structures reported are mechanically stable owing to the formation of inter-bead capillary bridges formed by the uncured PDMS in the presence of water; similar forces are responsible for the creation and stability of sandcastles. This paste has a high storage modulus and yield stress that allow it to be extruded at room temperature with an adapted 3D printer. The resulting structures are highly elastic, and the process can produce intricate meshes and other structures.[8]

Recent interest in stimuli responsive materials to be used in 3DP has spurred the design of innovative molecular functionalities:[10] including shape-memory polymers,[11–13] electroluminescent materials[14] and materials with functional molecular recognition.[15–17] Mechanically-responsive materials, such as those based on covalent mechanophores, remain relatively unexplored for use in 3DP.[18,19] In mechanophore-based polymers the strain felt in a polymer network changes the chemical potential energy of a desired chemical reaction. Historically, this reactivity was limited to homolytic bond scission reactions and the weakening of the polymeric material,[20,21] but the past decade has seen mechanophores used to drive responses include that self-strengthening,[22] chemical cargo release,[23] mechanochromism[24] and luminescence.[25] Spiropyran derivatives (SP) are among the most widely studied mechanophores and have been incorporated into commercial PDMS systems so that it will undergo a strain induced ring-opening reaction to yield a conjugated, colored merocyanine (MC)[26] (Figure 4.1(a)). If the mechanophore is appropriately embedded in the polymer network so that isomerization is coupled to molecular level tension in the network, the strain in the network can be monitored visually. The SP to MC reaction is reversible and repeatable; the color disappears when the material relaxes and returns if the elastomer is strained again.

There have been relatively few examples of 3D printable mechanoresponsive materials, perhaps because many mechanophores might undergo irreversible reactions under printing conditions.[27] Recently, Boydston and coworkers reported printing poly(ε-caprolactone) (PCL) containing SP by filamentizing the polymers and printing structures with a commercially available fused filament fabrication printer.[18] PCL was selected due to its low glass transition temperature, allowing for milder printing conditions over other polymer systems: however, once strained to mechanochromic activation, the material is irreversibly deformed. Boydston and coworkers also

reported photopolymerizing complex object geometries containing an oxanorbornadiene based mechanophore that releases a small molecule.[19] The molecule was extracted and quantified with GC-MC to determine percent activation of mechanophore as a function of strain. While the objects display full shape recovery, the mechanochemical reaction is irreversible and cannot be visualized. To address these limitations, we set out to combine the siloxane 3DP strategy reported by Roh and coworkers with the mechanochromic PDMS strategies previously reported previously by some of us (Figure 4.1(b)-(c)). Additionally, by incorporating SP in the uncured PDMS "bridging" material, we anticipated that the mechanophore would be concentrated at the interfaces between the beads where theoretical models predict stress to be concentrated under deformation,[28,29] via mechanism that is reminiscent of the selective mechanochemical activation of a Diels-Alder adduct-based mechanophore at silica-polymer interfaces.[30]Therefore, we hypothesized that this printing platform would provide both a strategy to 3D print mechanophores in silicone silicone materials that have increased mechanochromic activity compared to their bulk elastomer counterparts..

4.3 Materials and Methods

Sylgard 184 base and Sylgard 184 crosslinking reagent (Dow Corning) was purchased from Ellesworth Adhesive, Germatown WI, Mowiol 18-88, xylene and Polysorbate 20 were purchased from Sigma-Aldrich. Dragon Skin A and B were purchased from Smooth-On. All chemicals were used as received without further purification.

4.3.1 Creating the PDMS Inks.

The preparation of the PDMS ink first required the formation of PDMS microbeads. Sylgard 184 base and Sylgard 184 crosslinking reagent were combined in a 10:1 ratio. The PDMS prepolymer

mixture was then vortexed for 5 min and promptly degassed on a vacuum manifold for 30 min. Then, 6 mL of the PDMS pre-polymer mixture and 250 mL of a 14 wt% aqueous solution of polyvinyl alcohol (Mowiol 18-88) were combined and vigorously stirred for 10 min using an overhead mechanical stirrer at 1000 rpms (OS40-Pro,SciLogex). The reaction was left to continue overnight at 80°C to afford cured PDMS microbeads. The beads were washed ten times with 50 mL of polysorbate 20 solution (0.1 wt%). Storage of the PDMS microbeads in polysorbate 20 solution (0.1 wt%) as 50 wt% suspensions was necessary to prevent aggregation.

The PDMS microbead was transformed into a gel via the formation of capillary bridges. A solution of SP dissolved in xylenes (175 mg/mL) was added to Dragon Skin 30 Part B. This solution was thoroughly mixed before an equal mass of Dragon Skin 30 Part A was added to yield a polymer comprised of 1:1 (Part A: Part B) and loaded with 0.5 wt% SP. The PDMS microbead suspension and uncured Dragon Skin 30 precursor with SP were combined and vortexed to achieve a final ink composition of 40 wt% of Dragon Skin 30 precursor, 60 wt% Sylgard 184 microbeads and 0.25 wt% SP. After 5 min, a visible sol-gel transition was observed. The gel was further mixed with a mortar and pestle. The final ink contains small amounts of water.

4.3.2 Extrusion and Curing of PDMS Inks.

The silicone inks were hand loaded in a syringe and extruded by hand for preliminary characterization. The resulting structures were cured overnight at 85°C.

4.3.3 Characterizing Mechanochromic Composite Materials.

The inks were imaged via variable pressure scanning electron microscopy (XL30 ESEM, FEI). Cursory images of the cured structures under manually administered tension and compression were taken with a digital microscope (AM3111, Dino-Lite). Tensile tests were performed on cylindrical

samples of hand-extruded PDMS composite material with 0.25 wt% SP and Dragon Skin 30 thin films with 0.25 wt% SP and thin film samples of Dragon Skin 30 with 0.25 wt% SP. Samples were placed in a micro-strain analyzer (RSA IIIm TA Instruments) and the gap distance was subsequently set to zero the pressure reading. The gap speed was set to 1 mm s^{-1}. The tensile test was captured an SLR camera (Canon EOS RebelTM Xsi with a Canon EF-S 18-55 mm f/3.5-5.6 IS SLR lens). Images were white balanced by a color-neutral target card (OptekaTM Digital Color & White Balance Card), which was placed next to the instrument. The image was split into three color channels (red, green and blue) and the pixel intensity was quantified using Fiji ImageJ. The ratio of mean pixel intensity of the blue channel over the green channel was used to determine activation.

4.3.4 Rheological characterization of the PDMS ink:

Rheological characterization of the uncured ink was performed on a TA Instrument DHR-2 rheometer fitted with a 20 mm parallel plate geometry with a gap of 1 mm. Each experiment was run with freshly prepared samples in order to avoid any extent of curing within the silicones. All samples were subject to oscillatory pre-shearing at 10 rad s-1 for 8 min to improve the reproducibility of the data. An oscillatory stress sweep was performed by subjecting the sample to a strain from 0.01% to 100% (1 Hz) to characterize the linear viscoelastic region of the material. A viscosity versus shear rate experiment was performed at 25 °C from 0.01 to 100 s-1 to characterize the shear thinning nature of the material which is important in order to have good printability.

3D Printing of the Silicone Ink. Direct write 3D printing was performed on a modified Alunar i3RepRap extrusion printer that has been retrofitted for pneumatic dispensation with a custom syringe holder. 3D CAD models were designed using Autodesk Fusion360 and converted to a STL

file using Slicer. The objects were printed onto glass slides using a silicone ink comprised of 50:50 Dragonskin30 and Sylgard 184 microbeads with 0.25 weight% spiropyran. Syringes of 3cc volume were purchased from Nordson EFD and fitted with a 20-gauge polypropylene cone shaped nozzle. A pressure of 25 PSI was used to extrude the ink and the nozzle speed was set to 360 mm/s. The printed samples were cured at 85 °C for 2 h.

4.4 Results and Discussions

The development of mechanochromic silicones for direct-write 3D printing first required optimization of the silicone ink for extrusion-based processing. The ideal ink for direct-write extrusion should exhibit a yield stress and shear-thinning behavior.[34] After several rounds of optimization, we arrived at a formulation of 50 wt% Sylgard 184 beads (Dow Corning) held together with 50 wt% Dragon Skin 30 (Smooth-On) that displayed the requisite viscoelastic properties. The formulation exhibited a previously reported sol-gel transition,[8] indicating the formation of capillary bridges. Rheometrical characterization confirmed the yielding and shear-thinning behaviors of the silicone ink (Figure C2). The silicone ink gel exhibited a shear storage modulus on the order of 10^5 Pa that yielded at higher shear stresses. The shear-thinning nature of the material was confirmed by a decrease in viscosity of up to three orders of magnitude as a function of increasing shear rate. This allowed the formulation to be extruded from a syringe to form stable structures, which were subsequently cured (Figure 4.2(a)). The overall formulation was rendered mechanochromic through the incorporation of 0.25 wt% SP. The SP was covalently incorporated into the PDMS network via the platinum-catalyzed hydrosilation reaction that is responsible for the formation of cross-links in the nascent Dragon Skin 30. The cured composite displayed for SP activation, yielding reversible, visible activation by compression and tension

without material failure. SEM images demonstrated the large surface area presented at the bead-matrix interfaces of the material (Figure 4.2(b)). This interface is expected to be important for the increased mechanochemical activation of spiropyran.[33]

Next, we sought to evaluate the tensile strain required to activate SP in the extruded composites. The composite paste was extruded into cylindrical replicates for tensile testing that reliably achieved uniaxial strains of 100-140% before breaking. A camera was used to record the onset of color associated with SP activation during strain. To account for strain induced changes in diffraction, the ratio of the mean pixel intensity of the blue channel to that of the green channel for a small section of elastomer was employed, as reported previously.[35,36] SP isomerizes to a blue-purple MC, so the B/G channel ratio most cleanly reports mechanochromic onset. In previous reports, the onset was determined by analyzing a sequence of photographs of an ongoing tensile test that simply stretched the material until failure. The composite material is porous with numerous PDMS-to-air interfaces compared to bulk films, so light is more readily diffracted; the enhanced scattering leads to a strain-dependent background signal. To avoid complications due to the changing background, we exploited the lifetime of the MC-NO2 derivative, which has a lifetime of several minutes after the activating force is removed. The film was stretched cyclically with a microstrain analyzer, in a process that first took the film to a desired “activating” strain and then subsequently returned it to its zero strain resting state, at which point an image was captured (Figure C5-C7). The use of the resting state for image acquisition minimizes artifacts due to changes in lighting or sample geometry that might occur during stretching. The B/G pixel intensity (Figure C8) was then analyzed at zero percent strain and recorded as a function of activating strain. As a control sample, a film of Dragon Skin 30 with 0.25 wt% SP was analyzed in the same manner to compare the onset and intensity of the mean pixel intensity ratio as a function of strain. The

threshold B/G value used as the onset of SP mechanochromism was defined to be two standard deviations beyond the mean B/G from 0-50% strain over five replicates. All composites tested displayed mechanochromic onset at B/G values corresponding to 60-75% tensile strain (Figure 4.3), whereas the onset strain of mechanochromism in SP in Dragon Skin 30 is 140-150% tensile strain by the same standards. Though the composite materials displayed significantly greater B/G pixel intensity values, this is not necessarily evidence for increased percentage of mechanophore activation in the composites compared to the bulk films; as the geometries, quantity of SP and variations in diffraction patterns could all affect the B/G pixel intensity.

Once cured, the objects were flexible and could be stretched or compressed to activate the embedded spiropyran. Figure 4.4(a) shows a cartoon depiction of a 3D printed cylinder that was pressed against a benchtop by inserting a steel rod through the central cavity, pressing down, and rolling the rod against the interior of the cylinder. A comparison of color before (Figure 4.4(b)) and after (Figure 4.4(c)) clearly shows the purple color associated with SP activation in the region of compression. A 3D printed cone was similarly compressed along its central axis of symmetry with a glass slide (Figure 4.4(d)), again showing a change in color from off-white (Figure 4.4(e)) to purple (Figure 4.4(f)). It was observed that extent of coloration increased with the amount of pressure applied during compression (data not shown). Similar mechanochromism was observed, albeit to a lesser extent, in two dimensional auxetic meshes (Figure C9)

4.5 Conclusion

The mechanochromic silicone inks described here provide access to mechanochemically active, 3D-printable elastomers that might be useful in expanding the many applications of PDMS-based composite materials. In addition, the PDMS-bead composite architecture provides an easily

implemented strategy to improve the sensitivity of the mechanochromic response, both within and outside of the additive manufacturing space. We hypothesize that the greater sensitivity in the base material might be further enhanced in the future by utilizing 3D printed geometries that can localize the forces experienced within an object. Finally, while the mechanochromism of spiropyran is employed here as an easily characterized response, the overall strategy should be more general and could be employed to the ever-growing toolkit of mechanochemical responses available.

4.6 REFERENCE

1. Hofmann, M. 3D Printing Gets a Boost and Opportunities with Polymer Materials. *ACS Macro Lett.* **2014**, *3*, 382–386.
2. Ozbolat, I. T.; Yu, Y. Bioprinting Toward Organ Fabrication: Challenges and Future Trends. *IEEE Transactions on Biomedical Engineering* **2013**, *60*, 691–699.
3. Bertassoni, L. E.; Cecconi, M.; Manoharan, V.; Nikkhah, M.; Hjortnaes, J.; Cristino, A. L.; Barabaschi, G.; Demarchi, D.; Dokmeci, M. R.; Yang, Y.; et al. Hydrogel Bioprinted Microchannel Networks for Vascularization of Tissue Engineering Constructs. *Lab Chip* **2014**, *14*, 2202–2211.
4. Yu, D.-G.; Shen, X.-X.; Branford-White, C.; Zhu, L.-M.; White, K.; Yang, X. L. Novel Oral Fast-Disintegrating Drug Delivery Devices with Predefined Inner Structure Fabricated by Three-Dimensional Printing. *Journal of Pharmacy and Pharmacology* **2009**, *61*, 323–329.
5. Zhao, C.; Wang, C.; Gorkin, R.; Beirne, S.; Shu, K.; Wallace, G. G. Three Dimensional (3D) Printed Electrodes for Interdigitated Supercapacitors. *Electrochemistry Communications* **2014**, *41*, 20–23.
6. Gratson, G. M.; Xu, M.; Lewis, J. A. Direct Writing of Three-Dimensional Webs. *Nature* **2004**, *428*, 386–386.
7. Ladd, C.; So, J.-H.; Muth, J.; Dickey, M. D. 3D Printing of Free Standing Liquid Metal Microstructures. *Advanced Materials* **2013**, *25*, 5081–5085.
8. Roh, S.; Parekh, D. P.; Bharti, B.; Stoyanov, S. D.; Velev, O. D. 3D Printing by Multiphase Silicone/Water Capillary Inks. *Advanced Materials* **2017**, *29*, 1701554.
9. Qin, Z.; Compton, B. G.; Lewis, J. A.; Buehler, M. J. Structural Optimization of 3D-Printed Synthetic Spider Webs for High Strength. *Nature Communications* **2015**, *6*, 7038.
10. Roh, S.; Velev, O. D. Nanomaterials Fabrication by Interfacial Templating and Capillary
11. Engineering in Multiphasic Liquids. *AIChE Journal* **2018**, *64*, 3558–3564.
12. Roh, S.; Okello, L. B.; Golbasi, N.; Hankwitz, J. P.; Liu, J. A.-C.; Tracy, J. B.; Velev, O. D. 3D-Printed Silicone Soft Architectures with Programmed Magneto-Capillary Reconfiguration. *Advanced Materials Technologies* **2019**, *4*, 1800528.
13. Boydston, A. J.; Cao, B.; Nelson, A.; Ono, R. J.; Saha, A.; Schwartz, J. J.; Thrasher, C. J. Additive Manufacturing with Stimuli-Responsive Materials. *J. Mater. Chem. A* **2018**, *6*, 20621–20645.
14. Raasch, J.; Ivey, M.; Aldrich, D.; Nobes, D. S.; Ayranci, C. Characterization of Polyurethane Shape Memory Polymer Processed by Material Extrusion Additive Manufacturing. *Additive Manufacturing* **2015**, *8*, 132–141.
15. Senatov, F. S.; Niaza, K. V.; Zadorozhnyy, M. Yu.; Maksimkin, A. V.; Kaloshkin, S. D.; Estrin, Y. Z. Mechanical Properties and Shape Memory Effect of 3D-Printed PLA-Based Porous Scaffolds. *Journal of the Mechanical Behavior of Biomedical Materials* **2016**, *57*, 139–148.
16. Zarek, M.; Layani, M.; Cooperstein, I.; Sachyani, E.; Cohn, D.; Magdassi, S. 3D Printing of Shape Memory Polymers for Flexible Electronic Devices. *Advanced Materials* **2016**, *28*, 4449–4454.
17. Kong, Y. L.; Tamargo, I. A.; Kim, H.; Johnson, B. N.; Gupta, M. K.; Koh, T.-W.; Chin, H.-A.; Steingart, D. A.; Rand, B. P.; McAlpine, M. C. 3D Printed Quantum Dot Light-Emitting Diodes. *Nano Lett.* **2014**, *14*, 7017–7023.

18. Kim, J. H.; Chang, W. S.; Kim, D.; Yang, J. R.; Han, J. T.; Lee, G.-W.; Kim, J. T.; Seol, S. K. 3D Printing of Reduced Graphene Oxide Nanowires. *Advanced Materials* **2015**, *27*, 157–161.
19. Mandon, C. A.; Blum, L. J.; Marquette, C. A. Adding Biomolecular Recognition Capability to 3D Printed Objects. *Anal. Chem.* **2016**, *88*, 10767–10772.
20. Kirillova, A.; Maxson, R.; Stoychev, G.; Gomillion, C. T.; Ionov, L. 4D Biofabrication Using Shape-Morphing Hydrogels. *Advanced Materials* **2017**, *29*, 1703443.
21. Peterson, G. I.; Larsen, M. B.; Ganter, M. A.; Storti, D. W.; Boydston, A. J. 3D-Printed Mechanochromic Materials. *ACS Appl. Mater. Interfaces* **2015**, *7*, 577–583.
22. Cao, B.; Boechler, N.; Boydston, A. J. Additive Manufacturing with a Flex Activated Mechanophore for Nondestructive Assessment of Mechanochemical Reactivity in Complex Object Geometries. *Polymer* **2018**, *152*, 4–8.
23. Staudinger, H.; Bondy, H. F. Über Isopren Und Kautschuk, 17. Mitteil.: Über Die Fraktionierung Der Balata. *Berichte der deutschen chemischen Gesellschaft* (A and B Series) **1930**, 63, 724–730.
24. Li, J.; Nagamani, C.; Moore, J. S. Polymer Mechanochemistry: From Destructive to Productive. *Acc. Chem. Res.* **2015**, *48*, 2181–2190.
25. Matsuda, T.; Kawakami, R.; Namba, R.; Nakajima, T.; Gong, J. P. Mechanoresponsive Self-Growing Hydrogels Inspired by Muscle Training. *Science* **2019**, *363*, 504–508.
26. Shiraki, T.; Diesendruck, C. E.; Moore, J. S. The Mechanochemical Production of Phenyl Cations through Heterolytic Bond Scission. *Faraday Discuss.* **2014**, *170*, 385–394.
27. Davis, D. A.; Hamilton, A.; Yang, J.; Cremar, L. D.; Van Gough, D.; Potisek, S. L.; Ong, M. T.; Braun, P. V.; Martínez, T. J.; White, S. R.; et al. Force-Induced Activation of Covalent Bonds in Mechanoresponsive Polymeric Materials. *Nature* **2009**, *459*, 68–72.
28. Sagara, Y.; Karman, M.; Verde-Sesto, E.; Matsuo, K.; Kim, Y.; Tamaoki, N.; Weder, C. Rotaxanes as Mechanochromic Fluorescent Force Transducers in Polymers. *J. Am. Chem. Soc.* **2018**, *140*, 1584–1587.
29. Gossweiler, G. R.; Kouznetsova, T. B.; Craig, S. L. Force-Rate Characterization of Two Spiropyran-Based Molecular Force Probes. *J. Am. Chem. Soc.* **2015**, *137*, 6148–6151.
30. Ramirez, A. L. B.; Kean, Z. S.; Orlicki, J. A.; Champhekar, M.; Elsakr, S. M.; Krause, W. E.; Craig, S. L. Mechanochemical Strengthening of a Synthetic Polymer in Response to Typically Destructive Shear Forces. *Nature Chemistry* **2013**, *5*, 757–761.
31. Gossweiler, G. R.; Hewage, G. B.; Soriano, G.; Wang, Q.; Welshofer, G. W.; Zhao, X.; Craig, S. L. Mechanochemical Activation of Covalent Bonds in Polymers with Full and Repeatable Macroscopic Shape Recovery. *ACS Macro Lett.* **2014**, *3*, 216–219.
32. Suslick, K. S. Mechanochemistry and Sonochemistry: Concluding Remarks. *Faraday Discuss.* **2014**, *170*, 411–422.
33. Frenkel, J. *Acta Physicochim*. **1944**, USSR, 19, 51−76
34. Li, J.; Shiraki, T.; Hu, B.; Wright, R. A. E.; Zhao, B.; Moore, J. S. Mechanophore Activation at Heterointerfaces. *J. Am. Chem. Soc.* **2014**, *136*, 15925–15928.
35. Smith, P. T.; Basu, A.; Saha, A.; Nelson, A. Chemical Modification and Printability of Shear-Thinning Hydrogel Inks for Direct-Write 3D Printing. *Polymer* **2018**, *152*, 42–50.
36. Barbee, M. H.; Mondal, K.; Deng, J. Z.; Bharambe, V.; Neumann, T. V.; Adams, J. J.; Boechler, N.; Dickey, M. D.; Craig, S. L. Mechanochromic Stretchable Electronics. *ACS Appl. Mater. Interfaces* **2018**, *10*, 29918–29924.

37. Gossweiler, G. R.; Brown, C. L.; Hewage, G. B.; Sapiro-Gheiler, E.; Trautman, W. J.; Welshofer, G. W.; Craig, S. L. Mechanochemically Active Soft Robots. *ACS Appl. Mater. Interfaces* **2015**, *7*, 22431–22435.

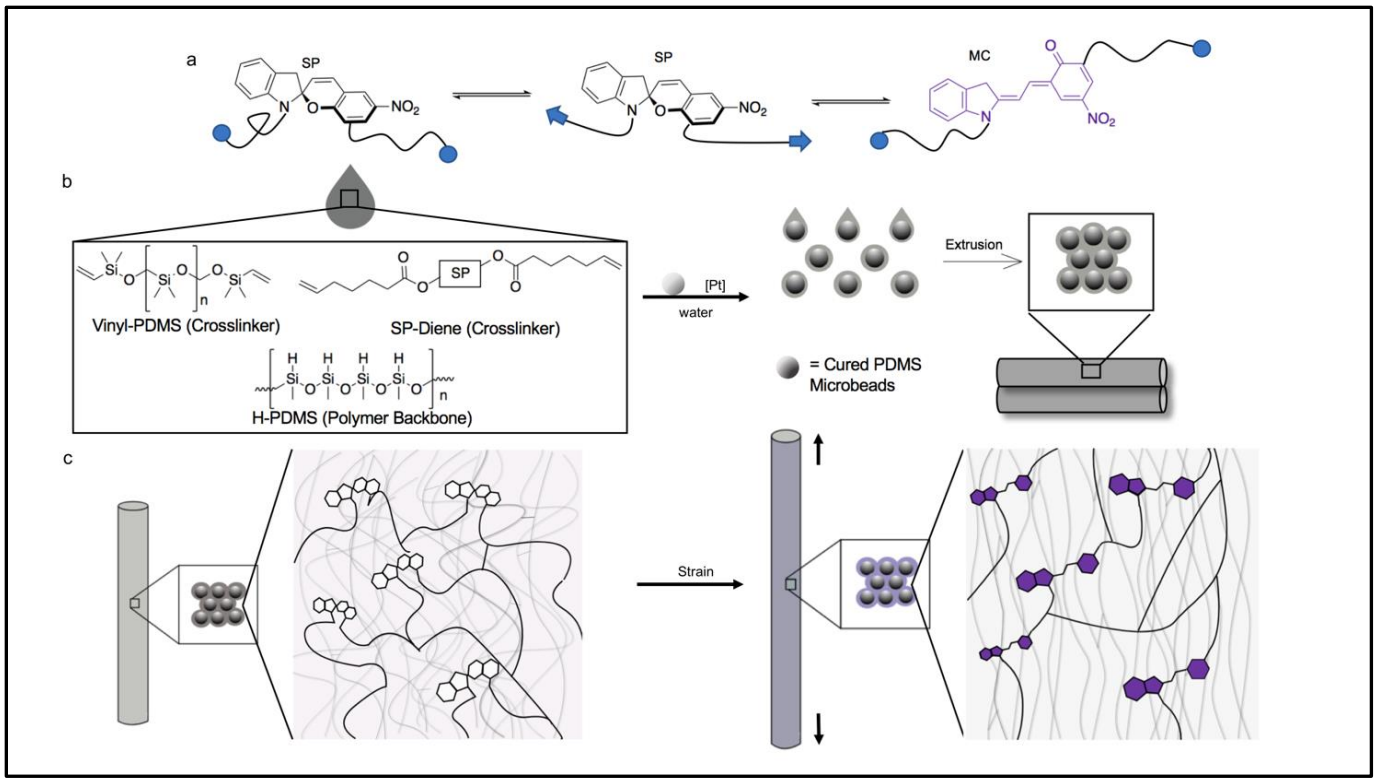

Figure 4.1: (a) (Left to right) SP is covalently incorporated into the polymer network. Macroscopic strain is transferred to the SP via the polymer network, resulting in enthalpic distortions to SP. At a critical force, SP isomerizes to MC and dissipates the force experienced by the polymer network. (b) The SP-diene is incorporated with Dragon Skin 30 vinyl-PDMS crosslinkers, H-PDMS and platinum catalyst. Cured Sylgard 184 microbeads are suspended in Dragon Skin 30 with incorporated SP. The resulting thixotropic paste is formed in the presence of water due to capillary action and is extruded and cured overnight at 80 °C. (c) Cured, extruded material at 0% strain with ring-closed SP crosslinked into the polymer network. After the material experiences strain, the composite displays mechanochromic activity at the bridging sites due to strain-induced ring-opening of spiropyran to form MC.

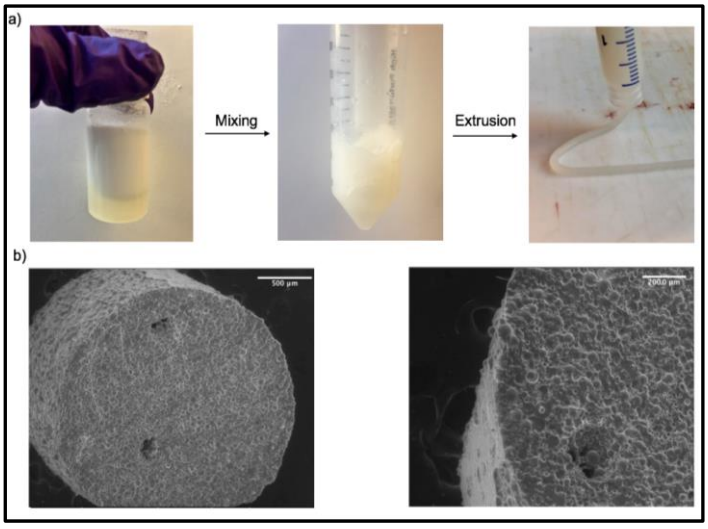

Figure 4.2: (a) Microbead suspension with bridging material. Upon mixing, a sol-gel transition is observed. The uncured silicone ink displayed adequate levels yield stress and shear-thinning for extrusion of multi-layered constructs. (b) Extruded material at 99x magnification (left) and 197x magnification (right).

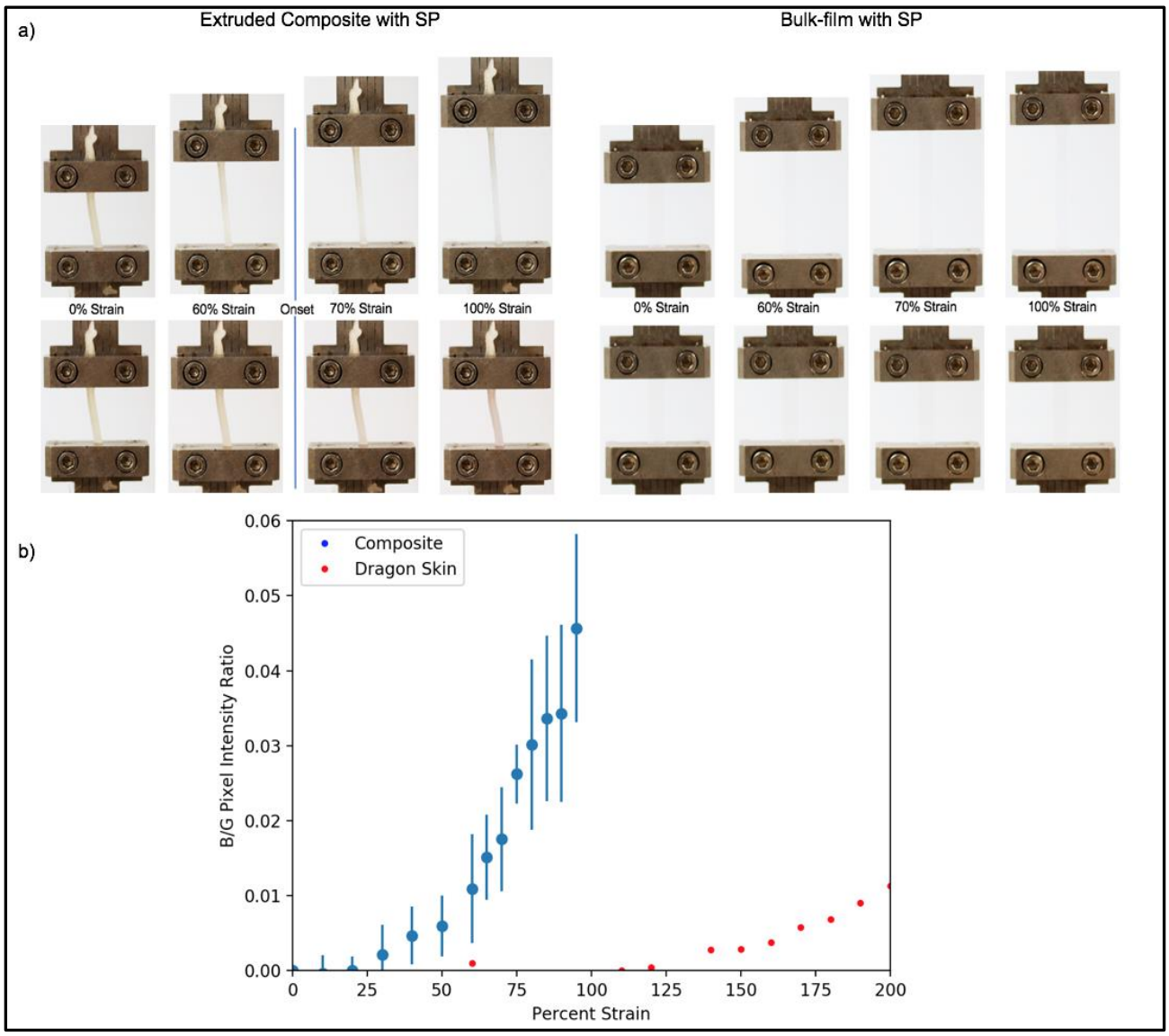

Figure 4.3: (a) Comparison of representative images from adaptive tensile tests at same strain. B/G intensity was measured from the same location when the sample was returned to 0% strain. (b) B/G values from image analysis. Extruded composite material displays SP onset between 60% and 70% strain. Dragon Skin material displays SP onset between 140% and 150%.

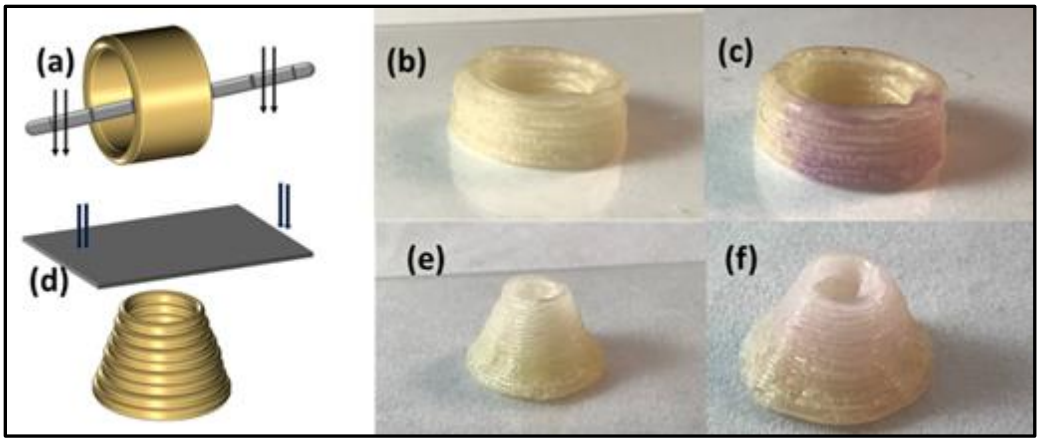

Figure 4.4: Mechanochromic activation in 3D printed constructs: (a) cartoon representing a hollow 3D printed cylinder with a steel rod inserted through it which was pressed on a hard surface. Images taken before (b) and after (c) application of force, showing a definite color change from the off-white to purple due to activation of spiropyran. (d) Cartoon of 3D printed cone which was compressed from top with a glass slide. Images taken before (e) and after (f) the compression showing activation of the cured ink.

CHAPTER 5: **MECHANO-ACTIVATION OF COLOR AND SHAPE IN 3D PRINTED IONIC POLYMER NETWORKS**

5.1 ABSTRACT

Stimuli-responsive 3D objects that can change shape in response to external cues represents an important subfield of 3D printing that could be employed as actuators and sensors. While temperature and pH are common inputs for initiating a response in a 3D printed object, there are few examples of using a mechanical input to afford a response. Herein, we report a suite of mechanochromic ionic liquid gel inks that can be used to fabricate 3D printed objects that utilize a single mechanoactivation event to elicit both, a mechanochromic response and a buckling-induced shape change. Direct-ink write (DIW) 3D printing was used to deposit ionic liquid gel inks with spatial control to create multimaterial objects that underwent a mechanoactivated shape change when the sample was pulled and let go. When spiropyran was incorporated into the inks, the onset of spiropyran isomerization into its purple merocyanine form was dictated by the viscoelastic characteristics of the polymerized ionic liquid. Thus, the onset of color could be used as a visual cue for the strain required to achieve a predetermined change in shape.

5.2 INTRODUCTION:

One of the hallmarks of a living organism is its ability to perceive and respond to an applied force or deformation. The motion observed in Mimosa plants and Venus flytraps, or the change in optical transparency in *Hippopodius* and *Vogtia* when touched, are excellent examples of biological systems responding to mechanical stimuli.[1-2] These biological systems have inspired scientists to design polymeric systems that utilize mechanical energy to trigger complex, autonomous responses[3-5]. Biological structures exhibit 3D hierarchical organization in a manner that cannot be replicated in synthetic systems. While recent developments in multimaterial 3D printing enable the fabrication of spatially organized constructs, the reproduction of the complexity in mechanically induced responses observed in nature is still a challenge.

Mechanoresponsive bulk polymer systems have largely been represented by one of two approaches: mechanochemical activation of molecular components (mechanochemistry) and mechano-activated shape change. Mechanochemical approaches[6] utilize a mechanophore to drive a host of responses that include changes in optical, electrical, or mechanical properties of a material, which is useful for strain sensing,[7-8] damage repair[9-10] or the release of small molecules.[11-12] Many mechanophores are challenging to 3D print due to their sensitivity to temperature or light. Both the Boydston[13] and Craig[14] groups have reported the successful incorporation and 3D printing of spiropyran within thermoplastic polycaprolactone and elastomeric polysiloxane composite, respectively. The spiropyran units within the 3D printed objects were successfully mechanoactivated to undergo an isomerization into its purple-colored merocyanine form, and these materials demonstrate the range of mechanical properties that can be achieved in the mechanoresponsive systems.

The second approach to create mechanoresponsive polymer systems uses mechanical force to induce a change in shape into a predetermined higher dimension.[15-17] For example, composite bilayers can undergo buckling or bending due to mis-matched elastic instabilities between the layers after the application of a compressive or tensile load.[18-19] A few examples of systems taking advantage of mechanoresponsive shape morphing have been reported in the fabrication of complex microstructures,[10,20] , tunable metamaterials[21] and altering the wettability of substrates.[22-23] Within the context of 3D printable materials which can undergo shape morphing (often referred to as 4D printing)[24], most bilayer systems have restrictions based on the need to pre-strain one layer, which also makes it suitable only for unidirectional bending.[25-26] Other groups have reported multidirectional bending in the absence of a pre-stretched layer by introducing mismatched elastic properties achieved from embedded aligned fibers[27] or degree of crystallinity.[28] However, these examples are not 3D printable, which limits the design architectures that can be achieved.

We recently reported the multimaterial DIW 3D printing of ionic liquid gels (ion gels) that can be spatially patterned to afford mechano-activated shape morphing objects.[29] The ion gel inks were comprised of a commercially available poly(ethylene oxide)-*b*-poly(propylene oxide)-*b*-poly(ethylene oxide) triblock copolymer (known as F127), which was modified at the chain ends with methacrylate functionalities (F127-BUM) and dissolved in alkyl vinyl imidazolium tetrafluoroborates. The viscoelastic and viscoplastic recovery of the photocured inks varied with the length of the alkyl sidechain. Thus, spatially controlled multimaterial 3D printing of these inks afforded objects that changed their shape in a predetermined manner after the application of a tensile force. Of note for this study, the autonomous bending angle of mechanoactivated bilayer constructs was highly dependent upon the magnitude of the applied strain. As such, when taken out of the controlled environment of a laboratory, applying an undetermined amount of strain on

a polymer network may cause mechanical failure or misfolding of the object into an undesired shape. Thus, we sought a mechanism by which users can be provided with visual cues, or a real-time set of "instructions", for the amount of strain required to achieve the desired shape morphing.

Herein, we report the incorporation of spiropyran dimethacrylate (SPDMA) as a mechanophore within a suite of polymerizable ion gel inks to develop a platform for DIW 3D printing to create objects wherein mechanochromic changes indicate the strain necessary to achieve the desired mechanoactivated shape change as shown in Figure 5.1(a). DIW 3D printing affords the easy patterning of inks and enables the creation of pre-programmed architecture which can be "activated" at a later time to undergo a shape change. Unlike hydrogel inks (a common choice for DIW 3D printing), the ion gel platform is extremely amenable to the incorporation of small molecules and additives.[30] Under tensile loading, macroscopic forces could be coupled to tension in the network in the molecular level leading to spiropyran undergoing ring opening isomerization to merocyanine accompanied by a change in color from dark yellow to vibrant purple (Figure 5.1(b)). The differences in viscoelastic behavior between these gels after curing leads to a difference in the amount of strain required for mechanophore activation. Additionally, when combined with DIW 3D printed bilayers, these mechanochromic inks can also be used to build visual strain gauges and indicate that the appropriate strain has been reached to achieve a predetermined bending angle.

5.3 Materials and Methods

Pluronics® F127 (BioReagent) was purchased from MilliporeSigma. 2-isocyanatoethyl methacrylate (98%) was purchased from Arctom. Dibutyltin dilaurate (>95%), 1-bromoethane (>99%), 1-bromobutane (>98%), 1-bromohexane (>98%), and sodium tetrafluoroborate (>95%) were purchased from TCI America. 1-vinylimidazole (>99%) was purchased from TCI America.

Diethyl ether, acetone, and methanol (HPLC grade) were purchased from Fisher Scientific. All reagents were used as received without further purification. Anhydrous methylene chloride was obtained by purification over alumina column on a Pure Process Technology purification system. DMSO-d_6 was purchased from Cambridge Isotope Laboratories (D, 99.9% + 0.05% V/V TMS).

S2. Synthesis methods

All ^{1}H-NMR spectra were collected on a Brüker Avance DRX 500 MHz spectrometer equipped with a Brüker triple resonance TXO probe (SI). Spectra were collected at 298 K with a pulse delay time (d1) of 5 or 10 s and 24 scans (^{1}H). The spectrometer was interfaced with a computer running Red Hat Enterprise Linux 6.2 and Topspin 2.1 software. Spectra were analyzed with Topspin 4.0.7 software. NMR samples were prepared in DMSO-d_6. Details of ^{1}H-NMR spectra are provided in Appendix D.

5.3.1 Synthesis of 1 1-ethyl-3-vinylimidazolium bromide ([EVIM]Br)

To a solution of 1-vinylimidazole (18.12 mL, 200 mmol) in acetonitrile (100 mL), 1-bromoethane (17.91 mL, 240 mmol, 1.2 equiv.) was added and magnetically stirred at 40 ℃ for 24 h. The solution was allowed to cool, and the crude product was precipitated in 500 mL EtOAc. The solids are collected by filtration, redissolved with minimal amount of MeOH, and added dropwise into 500 mL EtOAc. The precipitate is collected by filtration as a white solid and further dried in vacuo at 35 ℃ (32.71 g, 80 %).

5.3.2 Synthesis of 1 1-ethyl-3-vinylimidazolium bromide ([EVIM]Br)

1-vinylimidazole (9.06 mL, 100 mmol) and 1-bromobutane (12.89 mL, 120 mmol, 1.2 equiv.) were magnetically stirred at 45 ℃ for 24 h. After cooling, the viscous solution was washed with 100 mL ether three times and dried under vacuum to yield a pale-yellow viscous liquid in quantitative yield.

5.3.3 1-hexyl-3-vinylimidazolium bromide ([HVIM]Br)

1-vinylimidazole (9.06 mL, 100 mmol) and 1-bromohexane (16.80 mL, 120 mmol, 1.2 equiv.) were magnetically stirred at 45 °C for 24 h. After cooling, the viscous solution was washed with 100 mL ether five times and dried under vacuum to yield a pale-yellow viscous liquid in quantitative yield.

5.3.4 1-ethyl-3-vinylimidazolium tetrafluoroborate ([EVIM]BF_4)

1-ethyl-3-vinylimidazolium bromide (32.71 g, 161 mmol) and sodium tetrafluoroborate (18.57 g, 169 mmol, 1.05 equiv.) were added to acetone (75 mL) and let stir at rt for 48 h. The solution is then filtered through alumina to remove NaBr (fine white powder) and acetone was removed in vacuo to obtain a pale-yellow oil. The oil is then filtered through alumina to remove remaining $NaBF_4$ (white crystalline solids) and dried in vacuo (23.08 g, 68%).

[BVIM]BF_4 and [HVIM]BF_4 were prepared using the same method for [EVIM]BF_4. The resulting products were pale yellow oils ([BVIM]BF_4 :16.17 g, 67.9%, [HVIM]BF_4: 14.85 g, 55.8%).

5.3.5 Synthesis of Spiropyran dimethacrylate

Spiropyran-diol (synthetic procedure reported previously)[3] (1.49mmol) was added into anhydrous THF with 4-dimethylaminopyridine (DMAP) (1.63mmol). The mixture was stirred for 15 min. Methacrylic anhydride (3.86mmol) was then added to the system dropwise. The reaction proceeded for 5 hours and monitored by TLC. The crude product was plugged with basic alumina and washed with DCM. The solution was then rinsed successively with saturated ammonia chloride for 2 times, sodium bicarbonate for 2 times, DI water for 4 times, and brine for 1 time. The solution was dried over $MgSO_4$, filtered and then concentrated under reduced pressure to yield purple oil.

5.3.6 Ink Preparation for DIW printing:

To prepare the [EVIM]BF4 and [BVIM]BF4 hydrogels, 0.9g (30 wt%) of F127-BUM polymer was added to 2.1g(70 wt%) of ionic liquid. For the [HVIM]BF4 gel, 1.11g(37 wt%) if F127-BUM was added to 1.89g(63 wt%) of the ionic liquid. To each mixture, 15mg (0.5 wt%) of spiropyran dimethacrylate and Irgacure819 dissolved in 3mLs of methanol was added using volumetric pipettes and stirred on a magnetic plate until a vivid purple liquid with no solid residue was obtained. Methanol was then removed *in vacuo* at 32 °C until a self-supporting gel was obtained. The ionogels are loaded into 3cc syringes and centrifuged at 4000 rpm for 10 minutes to remove air pockets. The syringe cap was then removed and replaced with a 25 Ga Metcal extrusion nozzle (I.D. 0.26 mm).

Direct Ink Write 3D printing was performed on a modified Alunar i3 RepRap extrusion printer that has been retrofitted for pneumatic dispensation. All structures were originally created as a CAD file using Autodesk Fusion360 and converted to G-codes via Slic3r. All printing was performed with an extrusion air pressure of 17-20 psi. The structures were printed with 0.3 mm layer height, with printing speeds at 6-10 mm/s. Upon completion of printing, the structures were irradiated under broad spectrum white LED light (8W) for 2 hours to polymerize the ILs and crosslink the network with F127-BUM, irreversibly fixing the structures.

5.3.7 Rheometric Characterization of uncured inks

Rheometrical characterization was performed on a TA Instruments DHR-2 equipped with an Advanced Peltier Plate system. All rheometric experiments were performed using a stainless steel 8 mm upper plate. All gel samples were loaded onto a 3cc syringe, centrifuged to remove any trapped bubbles. The sample was then loaded by extruding the gel onto the loading plate and trimmed after the upper plate was lowered to the trim gap at 600 μm. The geometry gap between

upper and lower plates was then set to 500 μm for all experiments. For all experiments, a pre-shear was applied at 5 °C for 10 s before additional sample conditioning at 25 °C for 8 min. The frequency sweep experiment was performed to measure the storage and loss moduli at 1% strain over frequency range of 0.1 to 100.0 rad/s (equivalent to 0.0159-15.9 Hz). The strain sweep experiment was performed to measure the storage and loss moduli over 0.01 to 100% strain (1 Hz). The cyclic shear strain experiment (Figure 1e) was performed at 25 °C using alternating strains of 1% for 5 min and 100% for 3 min (1 Hz). The viscosity versus shear rate experiment was performed at 25 °C over a shear rate range of 0.01 to 100 s^{-1}.

5.3.8Tensile Characterization

An Instron 5585H electromechanical load frame with a 200N load cell and pneumatic grips were used to evaluate the mechanical properties of the cured ionogels under tension. All dogbone samples were made by extruding ionogels in a mold followed by photopolymerization. Samples with gauge length 5mm long, 2mm wide and 2mm thick were used in all measurement. The dogbone samples was then attached to the pneumatic self-aligning grips fixed on the load frame with sandpaper and superglue. The samples were subjected to increasing strain at a constant rate of 10 mm/min until mechanical failure of the sample.

5.3.9 Image Analysis for onset calculations

General information

Digital images analysis was performed on the samples to calculate onset of mechanochromic activation in the polymer samples. All samples were irradiated with white light for 30mins in order to revert any ring opened merocyanine to its closed spiropyran form. Dogbone samples were clamped in-between the pneumatic grips of an Instron 5585H load frame. Samples were stretched

at a constant rate of 10mm/mins and images were collected with a camera (Cannon TF6) at random intervals. All camera settings and light exposures were kept same within a data set. The images were captured in a .CR2 format to prevent any autocorrection and loss of any information.

Lightroom and Image J procedures

All images were imported into Adobe Lightroom CC and white balanced against a neutral background. In some cases, exposures were adjusted slightly taking care to apply the same settings to every picture within the experiment and exported as TIFF files. Images used in figures were cropped but otherwise unmodified.

All pictures were imported into ImgaeJ as an image sequence and converted into a hyperstack with 3 color channels (red, green and blue). A rectangular region of interest (ROI) was added to the ROI manager. The pixel intensity of the region was measure in every color and image in the stack. This is repeated for every image in the stack, making sure that the ROI is in the center of the samples being stretched.

The strain was measured in a similar manner. A straight line was added as the region of interest between two points on the sample and measured to get the length. The strain was calculated using the equation:

$$\%Strain = \frac{\{(final\ length) - (initial\ length)\}}{initial\ length} * 100$$

Onset of activation was calculated by plotting the difference between the ratio of blue to green color channels in the sample and the initial unstretched state versus strain to avoid errors due to external parameter or variation in color due to changing dimensions of the sample.

5.3.10 Extent of shape change in bilayer structures and shape morphing

All bilayer dogbone samples used in tensile tests were 10 mm long and 5 mm wide in the narrow section and bending was calculated according to a previously reported procedure[22]. Briefly,

dogbone samples were printed on the RepRap extrusion printer, with one material per layer, setting layer height to 0.3 mm (thickness/layer). Care was taken to incorporate spiropyran dimethacrylate in only one layer so that the color is easily visualized. The printed parts were then exposed to white light for 2h. The sample was then attached to the pneumatic self-aligning grips fixed on the Instron 5585H 250 kN electro-mechanical test frame with sandpaper and superglue. The samples were subjected to increasing strain at a constant rate of 10 mm/min until 25,50, or 100% strain, then removed from the grips. After 1 minute, the photo of the bilayer was taken, and the degree of bending is measured with ImageJ software.

5.4 Results and Discussion

F127-bis urethane methacrylate (F127-BUM) formed ion gels with 1-ethyl-3-vinylimidazolium tetrafluoroborate ([EVIM]BF_4), 1-butyl-3-vinylimidazolium tetrafluoroborate ([BVIM]BF_4), or 1-hexyl-3-vinylimidazolium tetrafluoroborate ([HVIM]BF_4) (Figure 5.1(c) and 5.1(d)) that were shear-thinning and exhibited a yield stress.[29] Irgacure819 and 0.5 w/w% SPDMA were added as the photoradical generator and mechanophore, respectively. The ion gels were formed by dissolving F127-BUM in the ionic liquid, wherein the triblock copolymer self-assembled to form micelles with a poly (propylene oxide) core and poly(ethylene oxide) shell. The polymer micelles functioned as both a gelator and a crosslinker for the ion gel. A 27-30 wt% concentration of F127-BUM was necessary to maintain the shear-thinning feature of the gels, which was required for DIW 3D printing. Rheometry was used to confirm that the presence of the mechanophore (5 wt%) did not affect the shear-thinning or the yield stress behaviors of the ion gel inks (Figure D1-D3). Oscillatory strain sweep experiments showed that the ion gels exhibited a

shear storage modulus on the order of 10^4 Pa. A cyclic strain experiment showed that the ink rapidly converted between the sol and gel states over multiple cycles without significant hysteresis.

2.1 Mechanical Properties of crosslinked ionic polymer networks

The vinyl groups on the imidazolium cation of the ionic liquids and the methacrylate functionalities of F127-BUM and SPDMA underwent photoinitiated free-radical polymerization to afford a cross-linked network. The final matrix was brownish-yellow, with a slight variation in color depending on the choice of the ion gel. To evaluate the mechanical behavior of the polymerized matrices, dogbone samples were casted and subjected to quasi-static tensile testing until failure. As seen in Figure 5.2(a), the three ion gel matrices exhibited different stress-strain curves based on the chain length of the alkyl groups on the ionic liquids. The [EVIM]BF_4, with shortest alkyl side chain of the set, was a viscoplastic material with a Young's Modulus of 579 MPa. Both [BVIM]BF_4 and [HVIM]BF_4 were viscoelastic materials (Young's Modulus of 102 MPa and 71MPa, respectively) with a time-dependent recovery.[29]

We explored the effect of changing the primary crosslinker on the mechanical properties by formulating ion gel inks with blends of noncross-linkable F127 and cross-linkable F127-BUM. To maintain the shear-thinning characteristic required to 3D print these gels, the total concentration of F127 and F127- BUM was held constant at 30 w/w% of polymer. When the F127-BUM concentration was decreased to 10 w/w% (and 20 w/w% F127), small changes to the elastic properties were observed. For example, in the [EVIM]BF_4 samples, there was a gradual decrease in Young's Modulus from 579 MPa to 520 MPa when the amount of F127:F127-BUM changed from 0:30 w/w% to 20:10 w/w%. Similar trends were observed for the [BVIM]BF_4 and [HVIM]BF_4 gels (Figure D4-D6). In all of these cases involving the polymer blends, the mechanical properties of the cured ion gel matrix were dependent upon the composition of the

ionic liquid and did not change significantly as the concentration of F127-BUM in the matrix decreased. Thus, while the F127-BUM acts as a cross-linker in the material, the mechanical properties of the material is largely derived from the composition of the polymerized ionic liquid.

2.2 Color activation test in ionic polymer networks

To quantify the tensile strain required to activate the SPDMA embedded within the polymeric network, dogbones were stretched at a rate of 10 mm/min, and the onset of color was recorded using a digital camera to capture a sequence of images at regular intervals. The ratio of the mean pixel intensity of the blue channel to that of the green channel (B/G) was calculated at the desired strain (Figure D7-D8). This data was recorded as a function of the activating strain and used to detect the onset of mechanochromic activation.[31.] The threshold of mechanochromic activation was defined as the point at which the B/G pixel intensity showed a change in slope.

The onset of activation correlated with the Young's modulus of the photocured ion gel. We observed that the [EVIM]BF_4 dogbone samples exhibited a color onset at the lowest strain (40%) as the material exhibited plastic deformation (Figure 5.2(b)). The necking region of the dogbone sample continued to elongate to an ultimate strain of 350% accompanied with a more intense purple color until material failure. The [BVIM]BF_4 and [HVIM]BF_4 behaved as elastomeric materials and exhibited a color response at ~120% and ~180% strain, respectively (Figure 5.2(c)-(d)) and (Figure D9). As a proof of concept demonstration, we 3D printed a single dogbone comprised of all three inks as shown in Figure 5.2(e)-(f), which was used to show that this sensor possessed visual indicators of the strain applied to the sample. Due to their viscoelastic nature, the [BVIM]BF_4 and [HVIM]BF_4 samples fully recovered their original shape over time (2h) if the samples were not stretched to the point of failure. Moreover, the spiropyran could be regenerated upon irradiation with broad spectrum white light (Figure D10). The color was preserved in all three

polymer matrices even after failure was reached, which indicates that the merocyanine form has a longer lifetime in these matrices. The purple color from the merocyanine form was localized and coincided with the drawing regions of the gauge section. The color intensities recorded for all three inks increased sharply as the material experienced strain hardening. The differences in strains required for the onset of mechanophore activation correlated with the stiffness of the polymer network: we hypothesize that in a stiff and tough matrix like [EVIM]BF_4, the strain applied on the system was transmitted to the spiropyrans incorporated into the polymer network, which in turn, isomerized to its ring-opened form. In case of the elastomeric [BVIM]BF_4 and [HVIM]BF_4 networks, chain mobility provided energy dissipation mechanisms that delayed the onset of mechanophore activation. The onset of spiropyran activation was not affected by the concentration of F127-BUM. For example, when [EVIM]BF_4 and [BVIM]BF_4 ion gels were formed using blends of F127 and F127-BUM at different concentrations (e.g., 0:30 w/w % to 10:20 w/w %), there was no significant change observed with the strain required for mechanochromic activity (Figure D11).

2.3 Shape Morphing in ionic polymer network bilayers

We next coupled two separate mechano-responses to a single mechanoactivation event: a mechanochromic response and a mechanoactivated shape-change. The onset of color in response to a mechanical load was used as a visual cue for any user to apply the strain required to afford a predetermined mechanoactivated shape response. Multimaterial DIW 3D printing was used to pattern the mechanochromic inks. When bilayer constructs were fabricated with an [EVIM]BF_4 layer (with SPDMA) followed by a [BVIM]BF_4 layer, (Figure 5.3(a)-(c)), a mechanochromic response was observed with 60% strain, and upon release of the applied load, the bilayer folded and the extent of the bending was ~111° (Figure D12). In contrast, a dogbone with SPDMA in the [BVIM]BF_4 layer, as opposed to the [EVIM]BF_4 layer, showed an onset of color when stretched

beyond 100% (Figure 5.3(d)-(f)), at which point a larger degree of bending was achieved (~167°). This result correlated with our expectations that a higher strain would induce greater extent of bending in the bilayer construct, and the incorporation of mechanochromic inks into the hinges could be used as a colorimetric indication of the target strain required to achieve a desired degree of bending.

We explored possible shape-memory like behavior of the network by heating the polymer bilayer to induce shape recovery. The original flat shape of the bilayer constructs could only be recovered when the mechanoactivated samples were heated at 120 °C while sandwiched between two glass slides. Two control sample were monitored: 1) one sample heated at 120°C without the glass slides became discolored and brittle and 2) one sample kept at room temperature sandwiched between glass slides showed partial recovery with no discoloration (Figure D13). We hypothesize that when the sample was heated without glass slides at 120°C, unpolymerized ionic liquid evaporated from the matrix at a high temperature to leave behind a polymerized network that was stiff and brittle. When the sample was sandwiched between two glass slides, evaporation was minimized and allowed the original flat structure to be regained.

In all cases, the bending of the bilayer construct was always in the direction of the elastomeric layer, and we could use 3D printing to control the spatial organization of the different inks to affect the direction of bending within a single object. We printed a bilayer with spatially localized regions of both inks that could be mechanoactivated to transform into a “W”. When the mechanophore SPDMA was incorporated into the [BVIM]BF_4 layer, the structure morphed into a “W” as shown in Figure 5.4(a)-(c). However, incorporation of the mechanophore in the stiffer [EVIM]BF_4 layer caused color activation at a lower strain, which led to a misformed structure that did not achieve the appropriate degrees of bending (Figure 5.4(d)-(f)).

Additional examples of mechanoactivated 4D printed objects such as a square pyramid, propeller, and airplane were also created (Figure 5.4 and D14). In the case of the pyramid, a smaller degree of bending was required, hence the SPDMA was incorporated in the [EVIM]BF_4 layer **(**Figure 5.4(g)-(h)). Alternatively, when the spiropyran was incorporated into the [BVIM]BF_4 layer, mechanochromic activation (biaxial activation required) occurred at a higher strain (Figure 5.4(i)), and the 3D printed bilayer over-folded. An airplane structure could be attained using the same concept. In this case, SPDMA was incorporated in the [BVIM]BF_4 layer to obtain the correctly folded structure. Finally, inspired by the shape of the propeller-like seeds in nature,[32] we printed a bilayer construct (Figure 5.4(j)-(k)) that could be mechanoactivated to fold into a propeller comprised of a tail and two wingblades. When launched from a height, the propeller possessed a spinning motion through air as it fell with a controlled velocity (Figure 5.4(l)). We envison such systems to be potentially applicable in easy transport of flat objects and on-demand shape morphing to reach a desired structure.

5.5 Conclusion

In conclusion, we have developed a suite of mechanochromic ionic liquid gel inks to fabricate 3D printed objects that utilize a single mechanoactivation event to elicit both a mechanochromic response and autonomous shape change in the object. The composition of the polymerized ionic liquid matrix determined the onset of spiropyran isomerization into its purple merocyanine form and could be used as a visual cue for the strain required to achieve a predetermined change in shape. DIW 3D printing provided spatial control of the inks within the printed objects, which enabled the final shape of the object after mechanoactivation to be programmed. Mechanoactivated materials represent an important subset of stimuli-responsive materials for 4D printing, and objects

that can respond to multiple stimuli, or provide multiple responses to a single stimulus, will enable the fabrication of synthetic systems that can rival the sophistication observed in natural systems.

5.6 REFERENCES:

1. Mackie, G. & Mackie, G. Mesogloeal ultrastructure and reversible opacity in a transparent siphonophore. *Vie Milieu* **18**, 47–67 (1967).
2. Volkov, A. G.; Foster, J. C.; Ashby, T. A.; Walker, R. K.; Johnson, J. A.; Markin, V. S. Mimosa Pudica: Electrical and Mechanical Stimulation of Plant Movements. *Plant, Cell & Environment* **2010**, *33*, 163–173
3. Caruso, M. M.; Davis, D. A.; Shen, Q.; Odom, S. A.; Sottos, N. R.; White, S. R.; Moore, J. S. Mechanically-Induced Chemical Changes in Polymeric Materials. *Chem. Rev*. **2009**, 109, 5755–5798.
4. Fu, H.; Nan, K.; Bai, W.; Huang, W.; Bai, K.; Lu, L.; Zhou, C.; Liu, Y.; Liu, F.; Wang, J.; Han, M.; Yan Z.; Luan, H.; Zhang, Y.; Zhang, Y.; Zhao, J.; Cheng X.; Li, M.; Lee, J.W.; Fang, D.; Li, X., Huang, Y.; Zhang, Y.; Rogers, J.A.; Morphable 3D Mesostructures and Microelectronic Devices by Multistable Buckling Mechanics. *Nature Materials* **2018**, 17, 268–276.
5. Liu, Y.; Genzer, J.; Dickey, M. D. "2D or Not 2D": Shape-Programming Polymer Sheets. Progress in Polymer *Science* **2016**, 52, 79–106.
6. Ghanem, M. A.; Basu, A.; Behrou, R.; Boechler, N.; Boydston, A. J.; Craig, S. L.; Lin, Y.; Lynde, B. E.; Nelson, A.; Shen, H.; et al. The Role of Polymer Mechanochemistry in Responsive Materials and Additive Manufacturing. *Nat. Rev. Mater.* **2020**, 1–15.
7. Potisek, S. L.; Davis, D. A.; Sottos, N. R.; White, S. R.; Moore, J. S. Mechanophore-Linked Addition Polymers. *J. Am. Chem. Soc.* **2007**, *129*, 13808–13809.
8. Göstl, R.; Sijbesma, R. P. π-Extended Anthracenes as Sensitive Probes for Mechanical Stress. *Chem. Sci.* **2016**, *7*, 370–375.
9. Ramirez, A. L. B. *et al.* Microstructure of copolymers formed by the reagentless, mechanochemical remodeling of homopolymers via pulsed ultrasound. *ACS. Macro. Lett.* **2012**,1, 23–27.
10. Ramirez, A. L. B.; Kean, Z. S.; Orlicki, J. A.; Champhekar, M.; Elsakr, S. M.; Krause, W. E.; Craig, S. L. Mechanochemical Strengthening of a Synthetic Polymer in Response to Typically Destructive Shear Forces. *Nature Chemistry* **2013**, *5*, 757–761.
11. Cao, B.; Boechler, N.; Boydston, A. J. Additive Manufacturing with a Flex Activated Mechanophore for Nondestructive Assessment of Mechanochemical Reactivity in Complex Object Geometries. Polymer 2018, 152, 4–8.
12. Chen, Z.; Mercer, J. A. M.; Zhu, X.; Romaniuk, J. A. H.; Pfattner, R.; Cegelski, L.; Martinez, T. J.; Burns, N. Z.; Xia, Y. Mechanochemical Unzipping of Insulating Polyladderene to Semiconducting Polyacetylene. *Science* **2017**, 357, 475–479.
13. Peterson, G. I.; Larsen, M. B.; Ganter, M. A.; Storti, D. W.; Boydston, A. J. 3D-Printed Mechanochromic Materials. *ACS Appl. Mater. Interfaces* **2015**, *7*, 577–583.
14. Rohde, R. C.; Basu, A.; Okello, L. B.; Barbee, M. H.; Zhang, Y.; Velev, O. D.; Nelson, A.; Craig, S. L. Mechanochromic Composite Elastomers for Additive Manufacturing and Low Strain Mechanophore Activation. *Polym. Chem*. **2019**, 10, 5985–5991.
15. Xu, S.; Yan, Z.; Jang, K.-I.; Huang, W.; Fu, H.; Kim, J.; Wei, Z.; Flavin, M.; McCracken, J.; Wang, R.; et al. Assembly of Micro/Nanomaterials into Complex, Three-Dimensional Architectures by Compressive Buckg. *Science* **2015**, *347*, 154–159

16. Ge, Q.; Dunn, C. K.; Qi, H. J.; Dunn, M. L. Active Origami by 4D Printing. *Smart Mater. Struct.* **2014**, 23, 094007.
17. Wang, X.; Guo, X.; Ye, J.; Zheng, N.; Kohli, P.; Choi, D.; Zhang, Y.; Xie, Z.; Zhang, Q.; Luan, H.; et al. Freestanding 3D Mesostructures, Functional Devices, and Shape-Programmable Systems Based on Mechanically Induced Assembly with Shape Memory Polymers. *Adv. Mater.* **2019**, 31, 1805615.
18. Torres, J. M.; Stafford, C. M.; Vogt, B. D. Elastic Modulus of Amorphous Polymer Thin Films: Relationship to the Glass Transition Temperature. *ACS Nano* **2009**, *3*, 2677–2685.
19. Stafford, C. M.; Harrison, C.; Beers, K. L.; Karim, A.; Amis, E. J.; VanLandingham, M. R.; Kim, H.-C.; Volksen, W.; Miller, R. D.; Simonyi, E. E. A Buckling-Based Metrology for Measuring the Elastic Moduli of Polymeric Thin Films. *Nat. Mater.* **2004**, *3*, 545–550.
20. Yan, Z.; Zhang, F.; Wang, J.; Liu, F.; Guo, X.; Nan, K.; Lin, Q.; Gao, M.; Xiao, D.; Shi, Y.; et al. Controlled Mechanical Buckling for Origami-Inspired Construction of 3D Microstructures in Advanced Materials. *Adv. Func. Mater.* **2016**, *26*, 2629–2639.
21. Shan, S.; Kang, S. H.; Raney, J. R.; Wang, P.; Fang, L.; Candido, F.; Lewis, J. A.; Bertoldi, K. Multistable Architected Materials for Trapping Elastic Strain Energy. *Adv. Mater.* **2015**, *27*, 4296–4301.
22. Jeong, H. E.; Kwak, M. K.; Suh, K. Y. Stretchable, Adhesion-Tunable Dry Adhesive by Surface Wrinkling. *Langmuir* **2010**, *26*, 2223–2226.
23. Purtov, J.; Frensemeier, M.; Kroner, E. Switchable Adhesion in Vacuum Using Bio-Inspired Dry Adhesives. *ACS Appl. Mater. Inter.* **2015**, 7, 24127–24135.
24. Sydney Gladman, A.; Matsumoto, E. A.; Nuzzo, R. G.; Mahadevan, L.; Lewis, J. A. Biomimetic 4D Printing. *Nat. Mater.* **2016**, *15*, 413–418.
25. Cafferty, B. J.; Campbell, V. E.; Rothemund, P.; Preston, D. J.; Ainla, A.; Fulleringer, N.; Diaz, A. C.; Fuentes, A. E.; Sameoto, D.; Lewis, J. A.; et al. Fabricating 3D Structures by Combining 2D Printing and Relaxation of Strain. *Adv. Mater. Technol.* **2019**, *4*, 1800299.
26. Gao, C.; Kewalramani, S.; Valencia, D. M.; Li, H.; McCourt, J. M.; Olvera de la Cruz, M.; Bedzyk, M. J. Electrostatic Shape Control of a Charged Molecular Membrane from Ribbon to Scroll. *Proc. Natl. Acad. Sci. U.S.A.* **2019**, *116*, 22030–22036.
27. Robertson, J. M.; Torbati, A. H.; Rodriguez, E. D.; Mao, Y.; Baker, R. M.; Qi, H. J.; Mather, P. T. Mechanically Programmed Shape Change in Laminated Elastomeric Composites. Soft Matter 2015, 11, 5754–5764.
28. Wisinger, C. E.; Maynard, L. A.; Barone, J. R. Bending, curling, and twisting in polymeric bilayers. *Soft Matter* **2019**, *15*, 4541– 4547.
29. Wong, J.; Basu, A.; Wende, M.; Boechler, N.; Nelson, A. Mechano-Activated Objects with Multidirectional Shape Morphing Programmed via 3D Printing. *ACS Appl. Polym. Mater.* **2020**, *2*, 2504–2508.
30. Kunz, W.; Häckl, K. The Hype with Ionic Liquids as Solvents. *Chem. Phys. Lett.* **2016**, *661*, 6–12.
31. Barbee, M. H.; Mondal, K.; Deng, J. Z.; Bharambe, V.; Neumann, T. V.; Adams, J. J.; Boechler, N.; Dickey, M. D.; Craig, S. L. Mechanochromic Stretchable Electronics. *ACS Appl. Mater. Interfaces* **2018**, *10*, 29918–29924.
32. Lentink, D.; Dickson, W. B.; Leeuwen, J. L. van; Dickinson, M. H. Leading-Edge Vortices Elevate Lift of Autorotating Plant Seeds. *Science* **2009**, 324, 1438–1440.

33. O’Bryan, G.; Wong, B. M.; McElhanon, J. R. Stress Sensing in Polycaprolactone Films via an Embedded Photochromic Compound. *ACS Appl. Mater. Interfaces.* **2010**, *2*, 1594–1600.

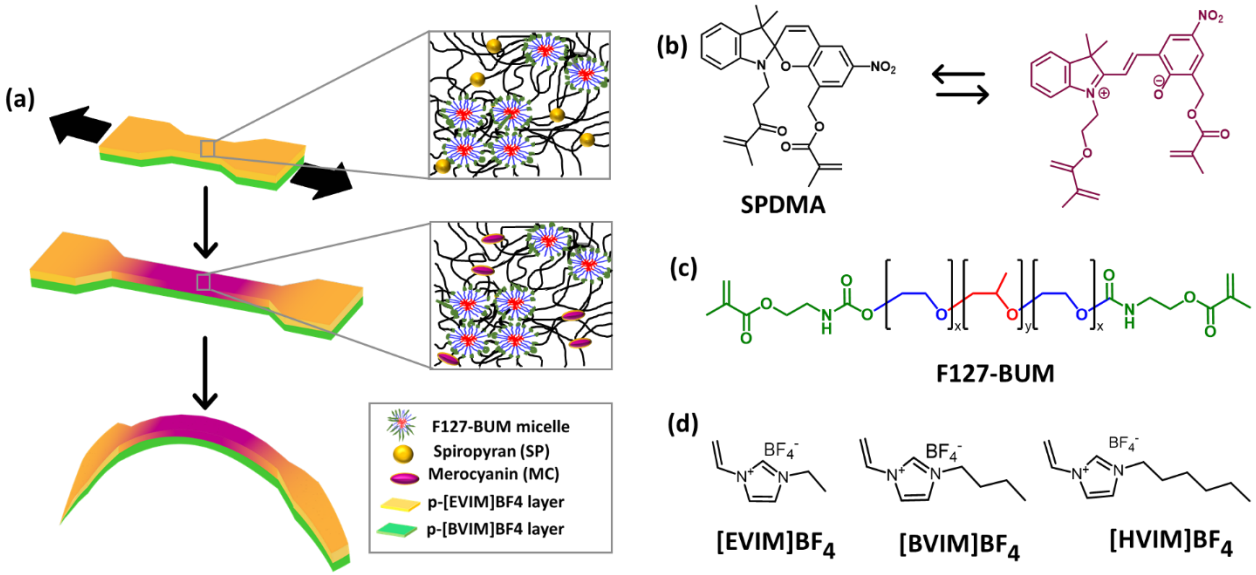

Figure 5.1: (a) Mechanical force used to simultaneously activate both the mechanochemical activation of (b) spiropyran into its merocyanine form, as well as the mechanoactivated shape change of 3D printed bilayer constructs. Ionic liquid gel inks were formed using (c) F127-BUM, which self-assembled to form micelles in the (d) polymerizable ionic liquids 1-ethyl-3-vinylimidazolium tetrafluoroborate ([EVIM]BF_4), 1-butyl-3-vinylimidazolium tetrafluoroborate ([BVIM]BF_4), or 1-hexyl-3-vinylimidazolium tetrafluoroborate ([HVIM]BF_4). DIW 3D printing afforded multimaterial constructs that could undergo a programmed autonomous shape response after pulling and releasing the printed object.

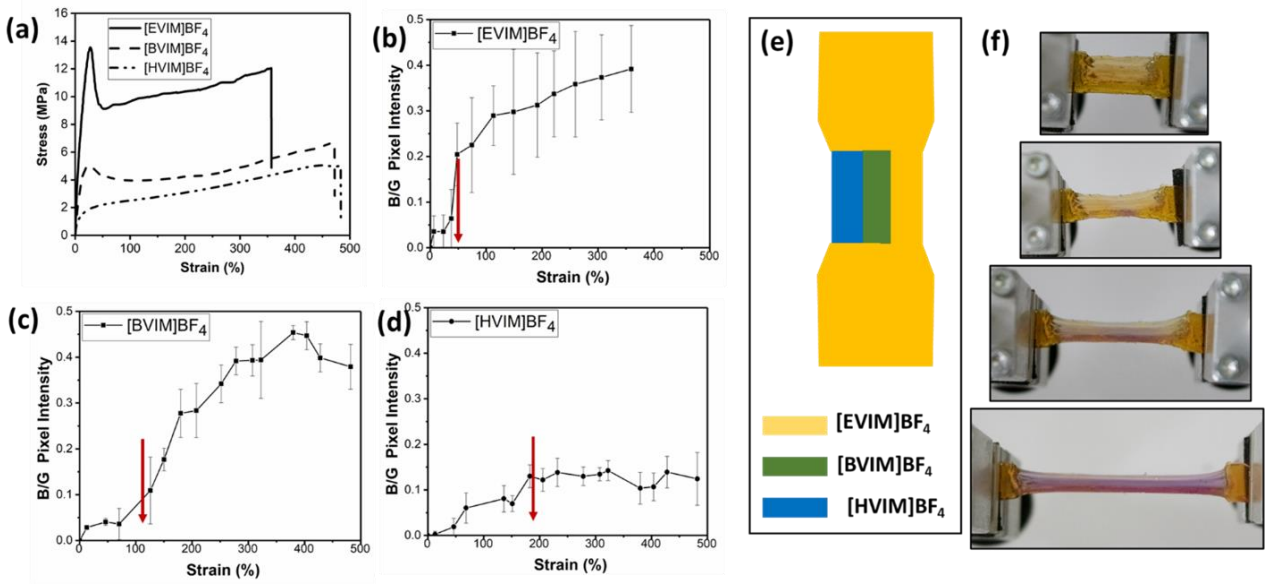

Figure 5.2: Mechanochemical activation of spiropyran in the three iongel samples. (a) stress-strain curves of all three iongels measured by casting into dogbones. Plots showing the onset of mechanochromism in (b) $[EVIM]BF_4$, (c)$[BVIM]BF_4$ and (d) $[HVIM]BF_4$ matrices calculated by the increase in B/G intensity of the samples when strained. (e) Cartoon of a single dogbone printed with three iongel inks. (f) Images shown are taken at 0%, 60%, 150% and 230% strain, showing the difference in onset of color with change in the polymer matrix.

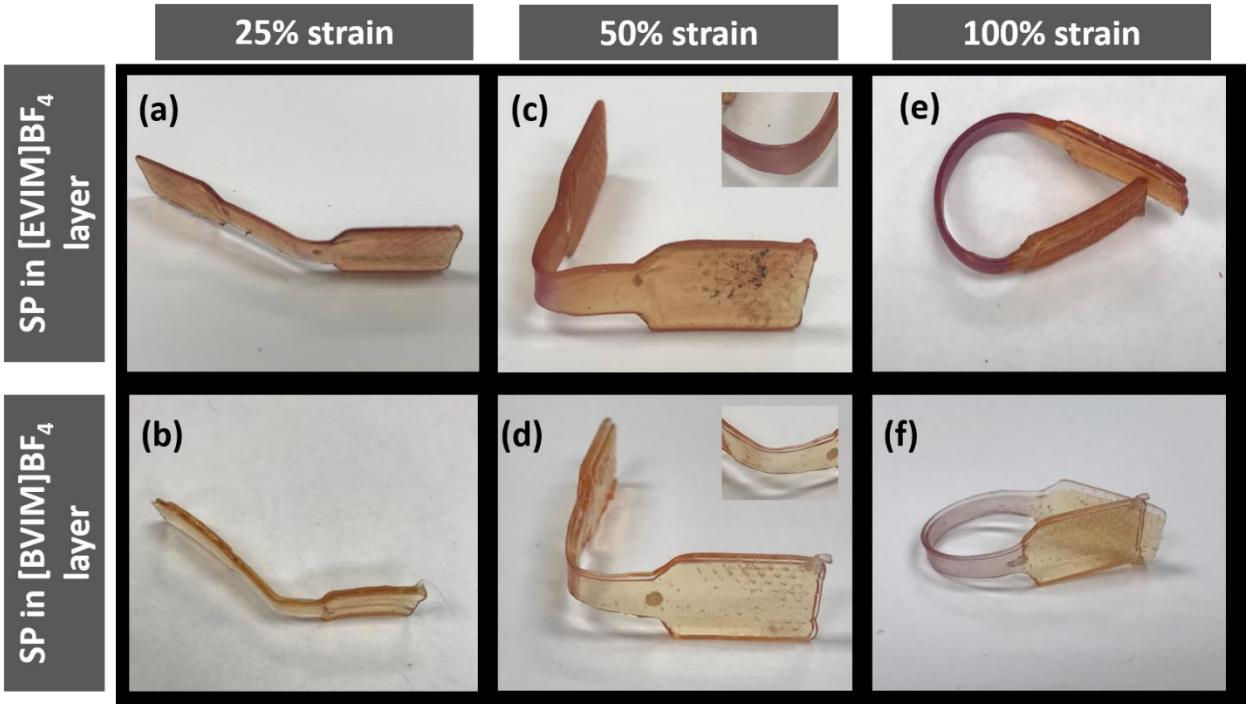

Figure 5.3: Images showing the onset of mechano-activated color and bending in 3D printed bilayer dogbones when incorporated in $[EVIM]BF_4$ and $[BVIM]BF_4$ under different strain conditions. (a-b) at 25% strain, no color is observed in either samples, (c-d) at 50% strain, $[EVIM]BF_4$ with SPDMA shows a purple coloration whereas $[BVIM]BF_4$ does not. At 100% strain, (e-f) both samples show purple color from the activation of SPDMA. The direction of bending is always towards the $[BVIM]BF_4$.

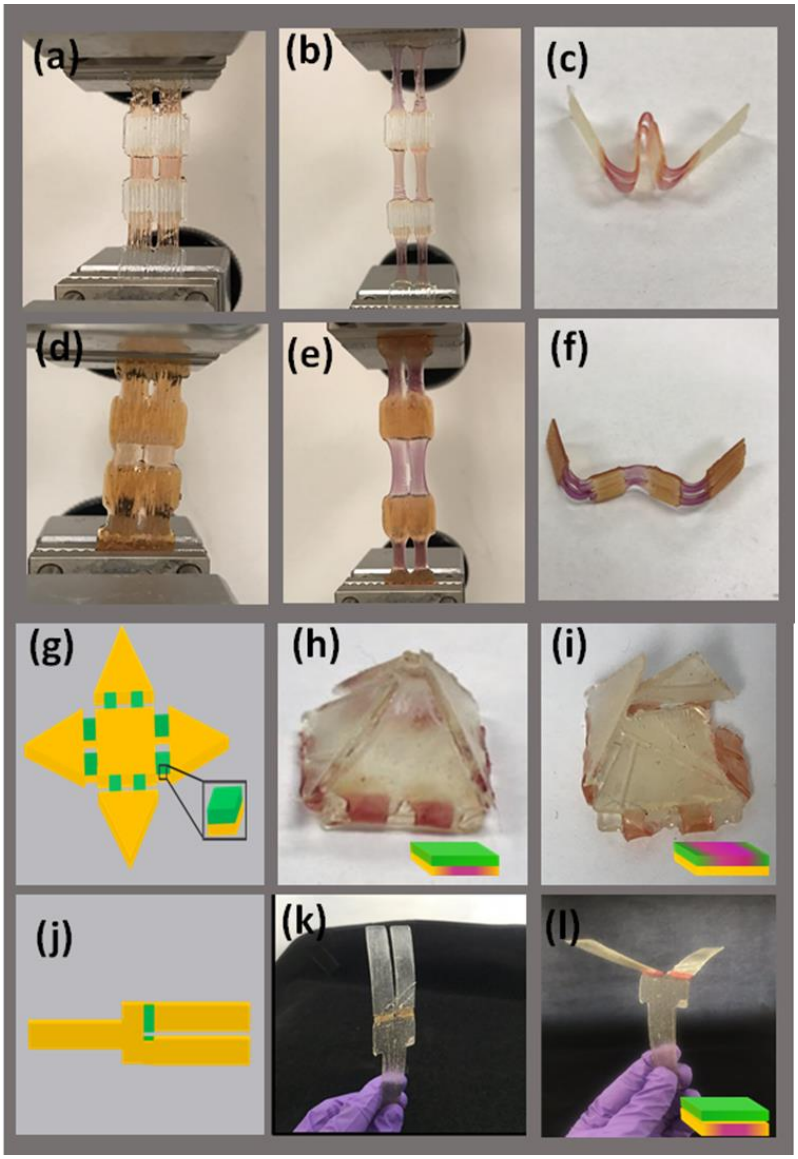

Figure 5.4: Examples of visual cues assisted mechano-activated transformation of planar constructs into 3D objects (a-c) when SPDMA is incorporated in the [BVIM]BF4 layer, color activation takes places at >100% strain which leads to the formation of a "W". However, when SPDMA is incorporated in the [EVIM]BF_4 matrix of the bilayer,(d-f), the onset of color activation takes place too early (40-60% strain) leading to a deformed 'W". (g) Cartoon example of a flat prism bilayer printed with SPDMA incorporated in (h) [EVIM]BF_4 and (i) [BVIM]BF_4. The former provides visual cue to form a prism with a square base while the latter leads to overstraining and crumpling of the structure. (j-k) Cartoon representation and picture of a 3D printed bilayer which could be transformed into (l) a propeller shape with the blades bending in opposite direction.

APPENDIX A

Catalytically Initiated Gel-in-Gel Printing of Composite Hydrogels

Synthesis of Graphene Oxide from Graphite. Graphite powder (3.5 g) were mixed into 120 ml concentrated sulphuric acid solution (98.5 %) which was cooled in an ice bath. Then, $NaNO_3$ (2.5 g) and $KMnO_4$ (11.6 g) were slowly added under vigorously stirring in sequence, so that the temperature was constantly maintained below 20 °C. The mixture was then stirred continuously at 35 °C for 8 h. After, 9.5 g of $KMnO_4$ were added to the solution, the reaction was left running continuously at 35 °C for other 12 h. The reaction was interrupted by pouring slowly the mixture into 600 ml of deionized water under stirring. Finally, 20 ml of 30% H_2O_2 were added and the mixture changed color into bright yellow, followed by bubbling. The mixture was filtered and washed with 1000 ml 5 % HCl aqueous solution and 200 ml ethanol. The solid powder was dried at 40 °C overnight, under vacuum. A Renishaw Raman confocal microscope at 514 nm was used to characterize the product, which showed characteristic D and G peaks at 1350 and 1600 cm^{-1} respectively. A stock solution was made by dispersing graphene oxide in deionized water at a concentration of 2 mg/ml, by sonicating it for two hours. TEM imaging done on a Phillips CM100 transmission electron microscope. A diluted solution of GO dispersed in water was dropped on carbon coated copper grid and drying under ambient condition before introducing into the TEM chamber.

Functionalization of Multi Walled Carbon nanotubes. MWCNT (300 mg) was dispersed in 40 mL of a mixture (3:1) of concentrated H_2SO_4 and concentrated HNO_3 and was sonicated for about 8 h in an ultrasonic bath at ~50 °C. Then the mixture was centrifuged and washed repeatedly with water until pH of the solution reached ~6.5. The black solution of the MWNTs in water was then filtered through a 0.47 μm pore size PVF2 membrane (hydrophilic), and the filtered material was dried in vacuum at 50 °C for 1 d. The acid functionalized carbon nanotubes (hereby referred as f-CNT) was characterized using a Bruker FT-IR spectrometer which showed peaks at 1715 cm^{-1} confirming the formation of -COOH groups due to oxidation during the acid treatment. A stock solution of 5mg/ml was made by sonicating the F-CNT in deionized water for several hours.

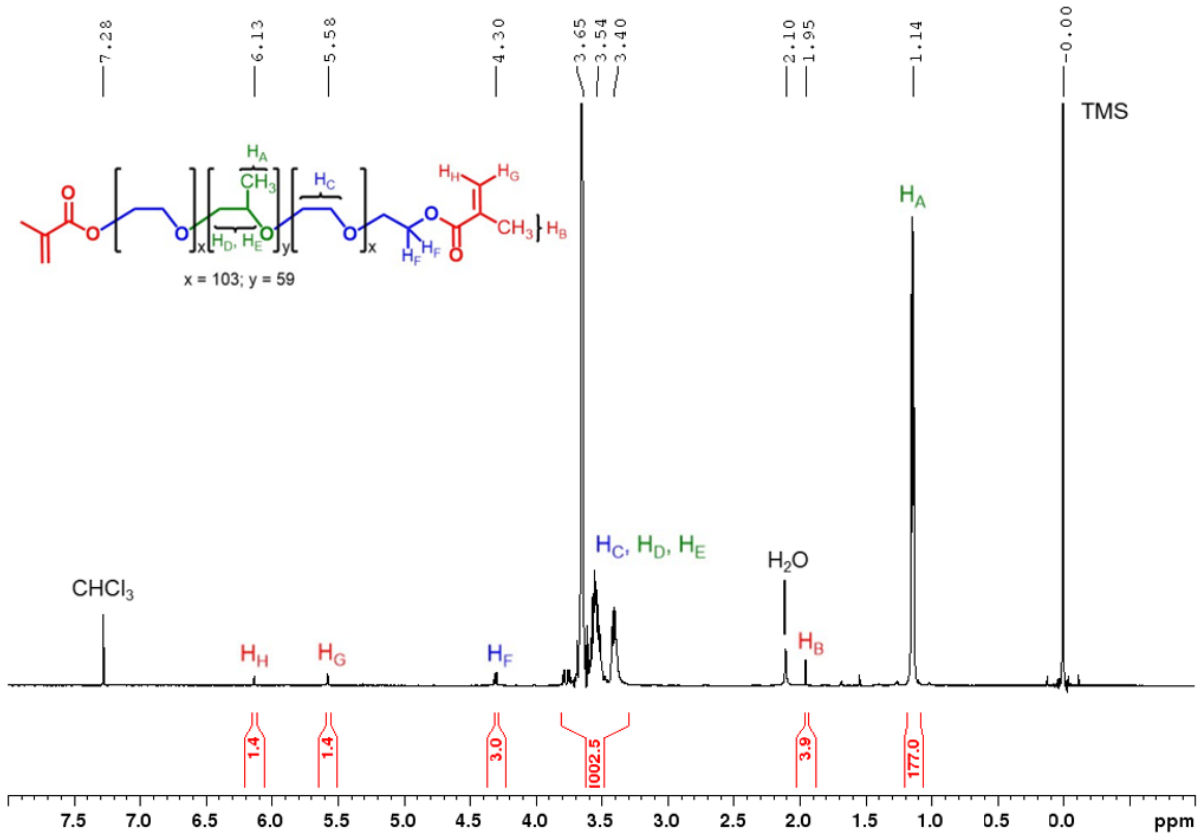

Figure A1: ^{1}H NMR spectrum of F127-DMA.

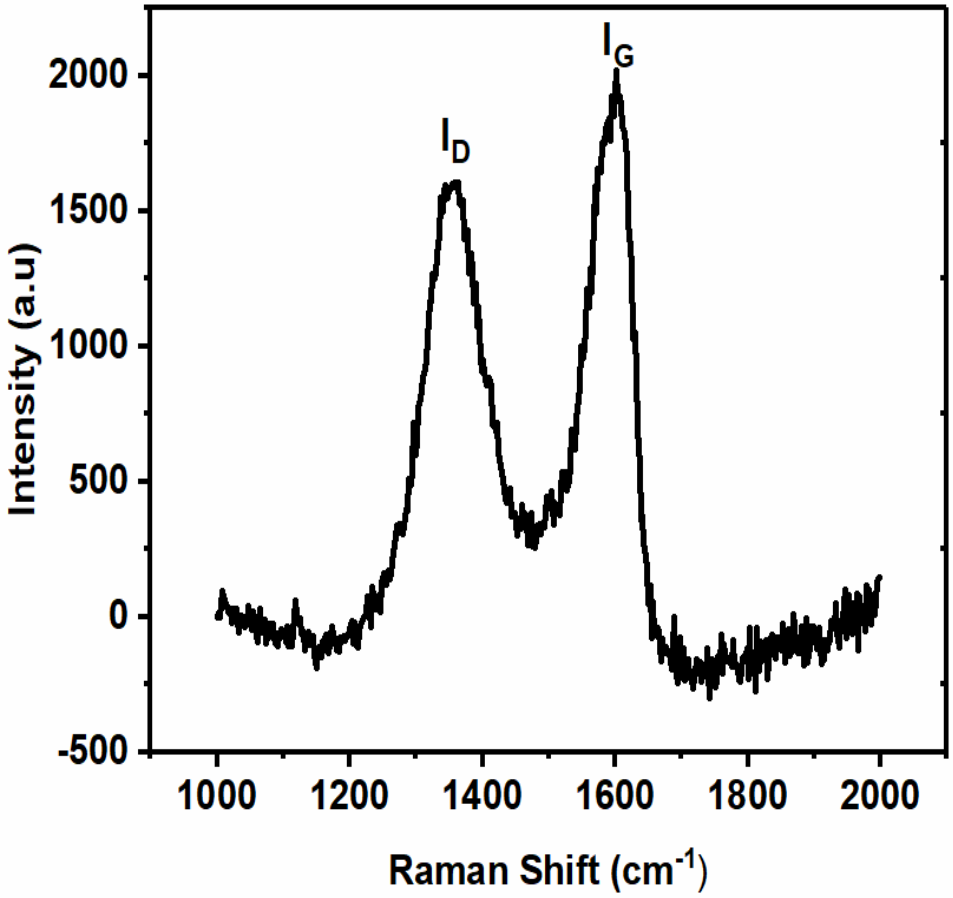

Figure A2: Raman spectra of GO showing characteristic D and G bands at 1350 cm^{-1} and 1600cm^{-1} respectively.

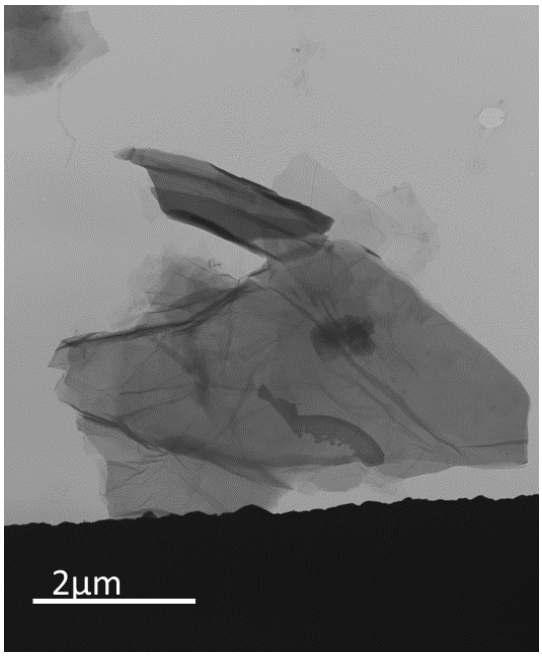

Figure A3: TEM image of exfoliated GO sheets.

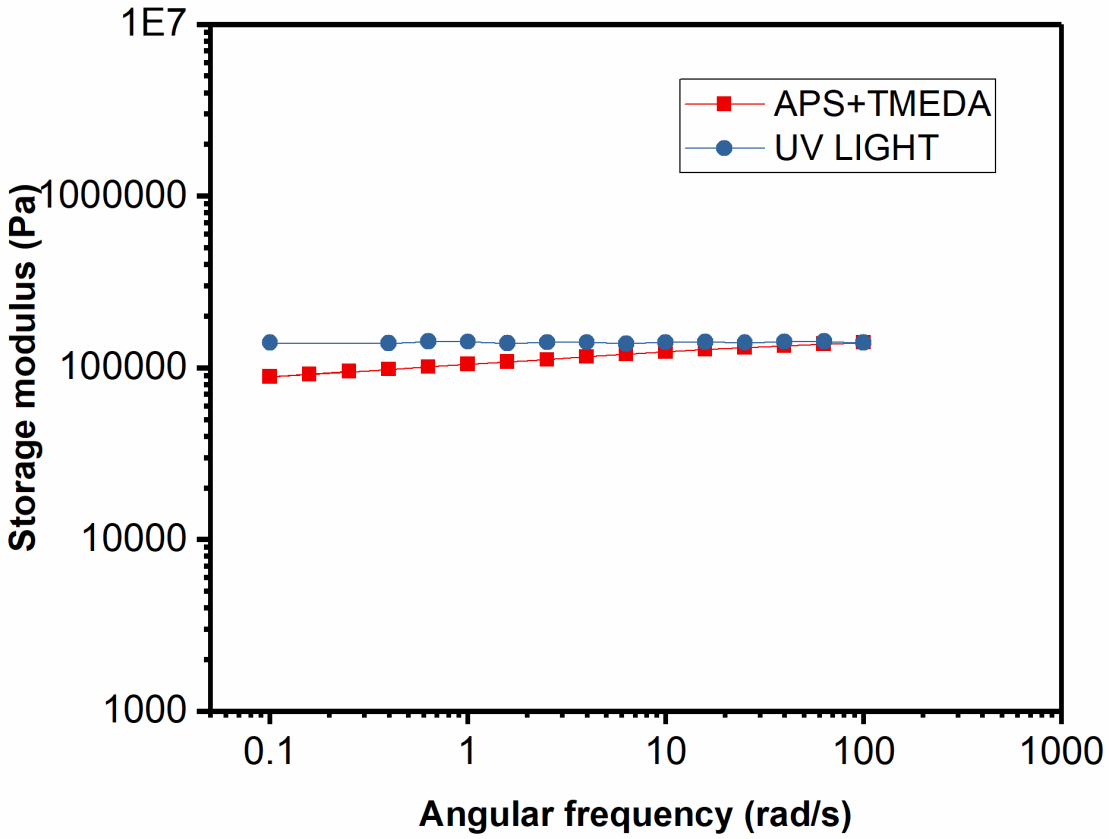

Figure A4: Frequency sweep data of 25% F127DMA after crosslinking with different curing systems.

APPENDIX B

Rheological Correlation and Effect of Additives on the 3D Printability of Hydrogels.

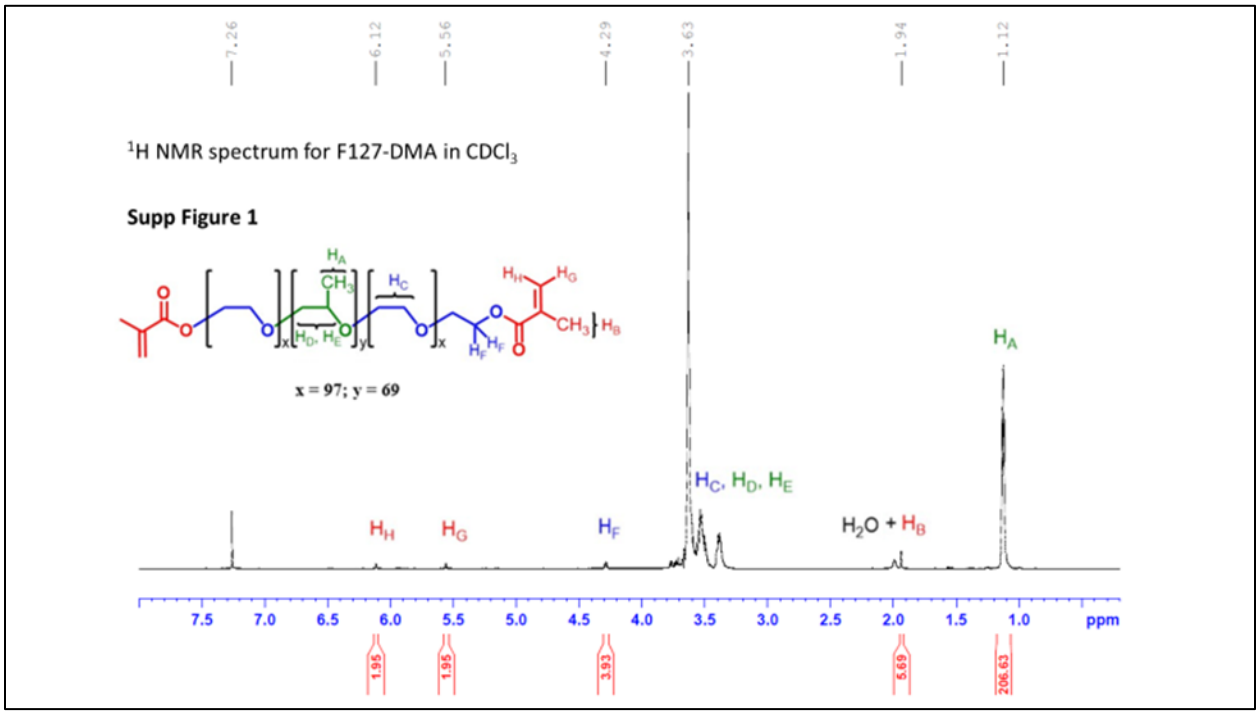

Figure B1: ^{1}H NMR spectrum of F127-DMA in $CDCl_3$.

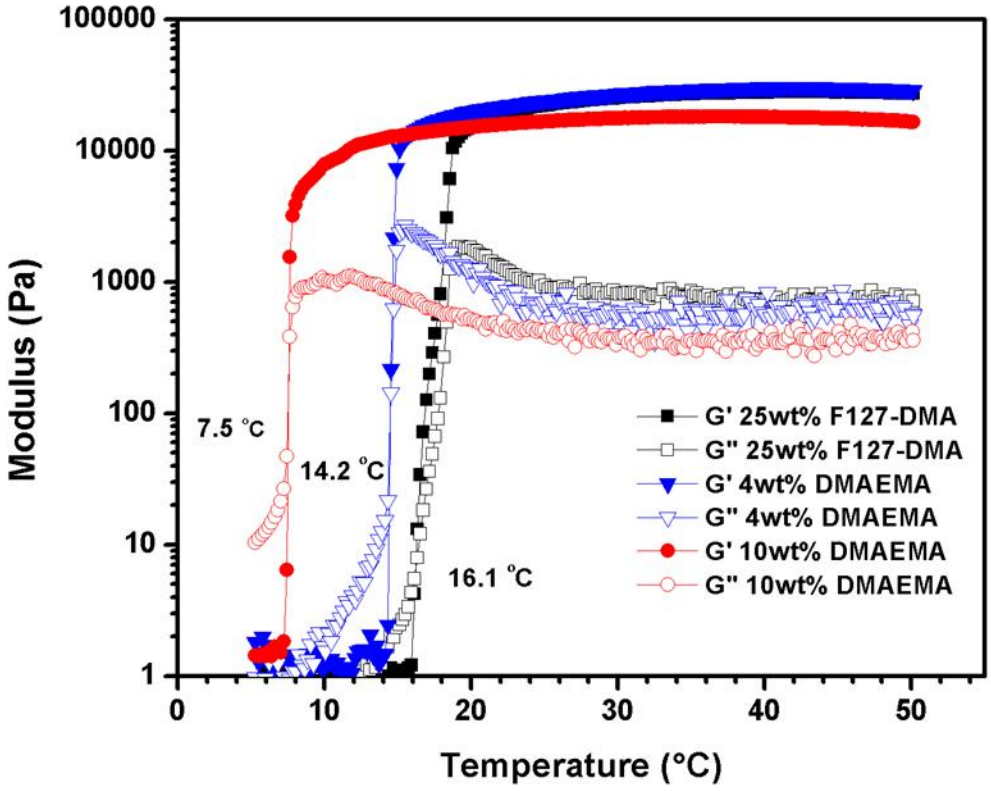

Figure B2: typical temperature ramp data of the hydrogel formulations with the gelation temperature given by the crossover of storage (G') and Loss (G") modulus.

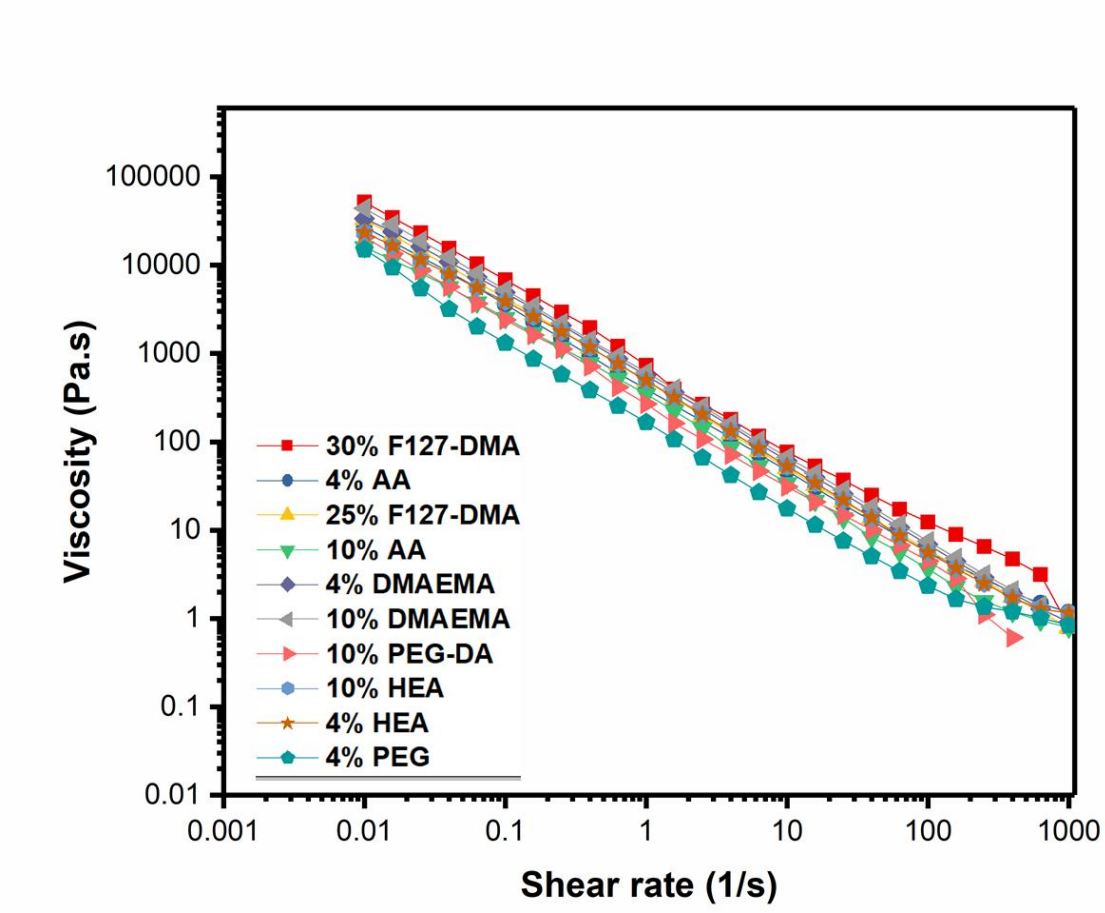

Figure B3: Viscosity vs. shear rate plot of different hydrogel ink formulations

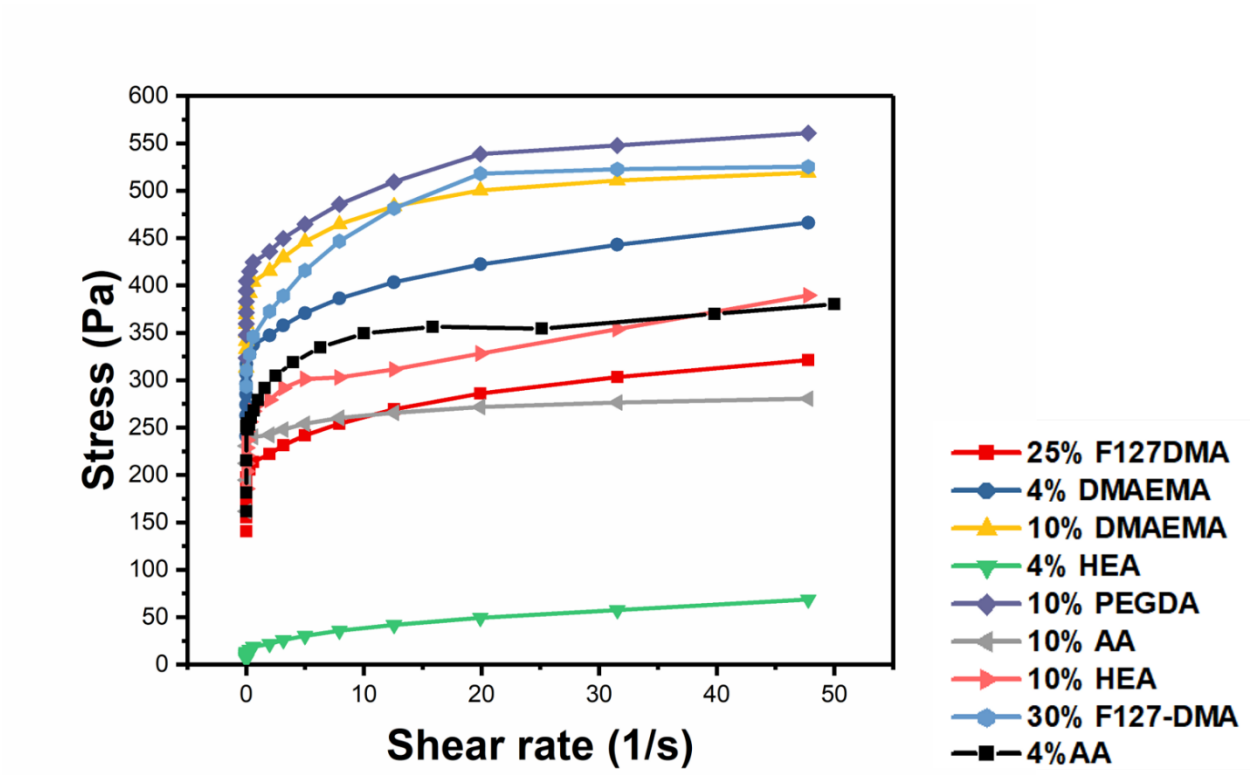

Figure B4: stress versus shear rate plots of different hydrogel formulations under increasing shear rates from 0 to 50 s^{-1}.

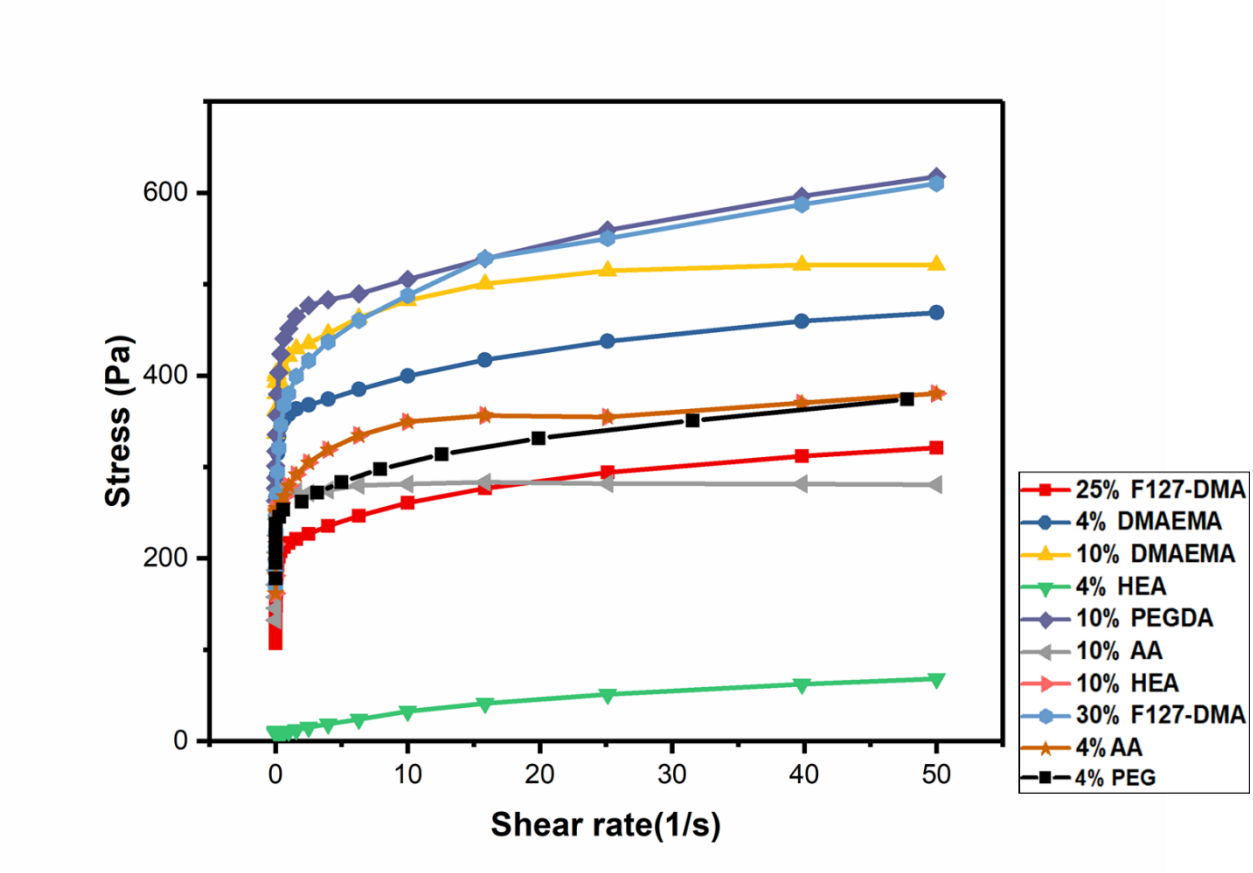

Figure B5: stress versus shear rate plots of different hydrogel formulations under decreasing shear rates from 50 to 0 s^{-1}.

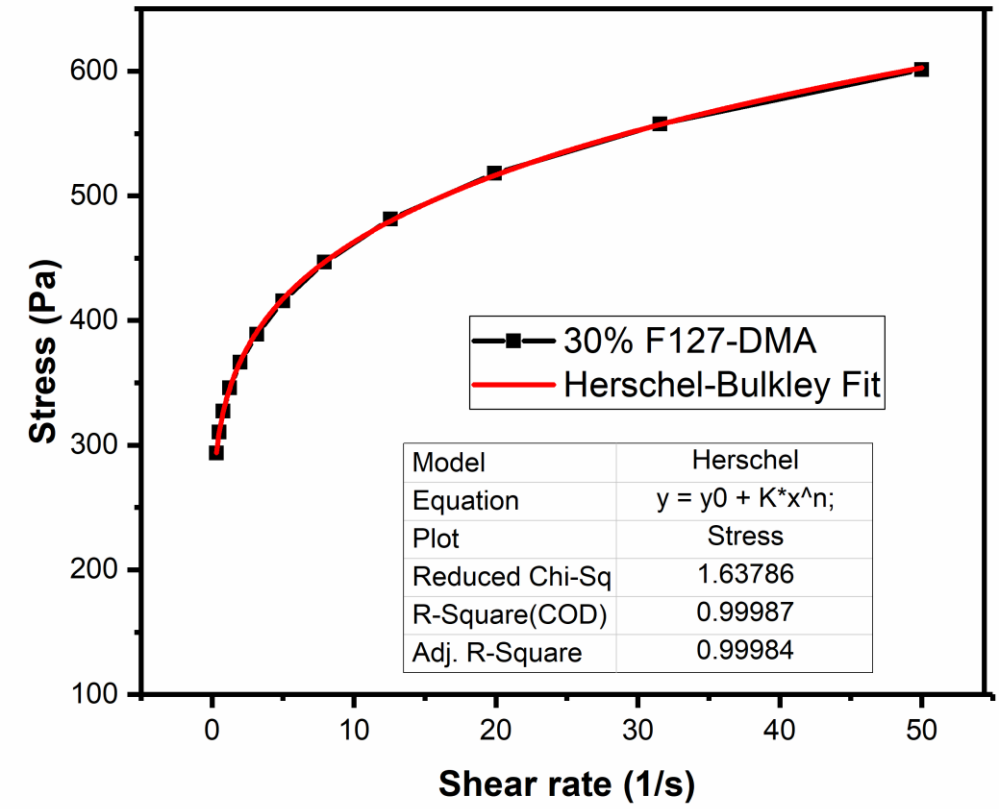

Figure B6: Herschel-Bulkley fit for 30% F127-DMA

Calculation of Viscosity of Hydrogel Inks:

Based on previous work by Chua *et.al*[39]. when the reference shear rate (γ_0) = 1 s^{-1}, the viscosity for Pluronic hydrogels could be determined by using the Power law equation for shear thinning fluids given by:

$$\eta = \eta_0 \dot{\gamma}^{n-1} \qquad (1)$$

Where η and η_0 are the apparent and zero-shear viscosities and $\dot{\gamma}$ is the shear rate. Thus equation (1) can be changed into a logarithmic expression:

$$\text{Log } \eta = \text{(n-1) Log } \dot{\gamma} \quad + \text{Log } \eta_o$$

A log-log plot of viscosity versus shear rate for each formulation would enable us to calculate its dynamic viscosity (supplementary information). The value of *n*, the Power Law index appearing in the expression, from the above equation enabled us to calculate the viscosities of the materials using the equation

$$\dot{\gamma} = \frac{(3n+1)*}{4n} 2V/_D \qquad (2)$$

Where V is the print speed and D is the nozzle diameter. Thus for 25 % F127-DMA, n= 0.0673, Putting that in equation (2) gives the shear rate as 467 s^{-1}, which corresponds to a viscosity value of 1.486 Pa.S. All the hydrogel ink viscosities were determined this way.

Diffusion tests

For each formulation, three tensile specimens were prepared then cut in half. The resulting six specimens were then subjected to one of two conditions; dried under vacuum immediately after preparation (non-swollen) or immersed in water until reaching equilibrium swelling then dried under vacuum (swollen). The non-swollen samples were massed, dried under vacuum for 48 hours, then massed again. The masses of the swollen samples were recorded prior to swelling, followed by immersion in a large excess of deionized water for 96 hours at 21°C. During the 96-

hour immersion, the water was replaced with fresh deionized water every 12 hours. After four days of immersion, the equilibrium swelling masses were recorded, then the specimens were dried under vacuum for 48 hours.

The final dried mass of each specimen was subtracted from its initial mass, then divided by its initial mass to determine the % mass loss after drying. The % mass loss of the swollen samples was compared to the % mass loss of the non- swollen samples to prove that the polymerized additives are covalently bound to the hydrogel network. The swelling ratios are represented as (swollen mass – dried mass) / dried mass.

For the controls, formulations with 4wt% and 10wt% poly(acrylic acid) (PAA) were tested. All of the PAA was able to diffuse out of the crosslinked F127-DMA network, as it was not covalently bound.

Additive (wt%)	% Water in formulation	Swelling ratio	% mass loss (non-swollen)	% mass loss (swollen)
None	75	6.14 ± 0.04	70.50 ± 0.7	73.24 ± 1.3
AA (4)	71	4.91 ± 0.01	67.78 ± 1.0	70.98 ± 0.2
HEA (4)	71	6.55 ± 0.02	68.10 ± 0.8	69.23 ± 0.2
DMAEMA (4)	71	10.28 ± 0.04	71.52 ± 0.3	74.54 ± 0.2
PEG-DA(4)	71	5.13 ± 0.01	64.58 ± 1.3	68.31 ± 0.2
PAA (4)	71	4.95 ± 0.04	68.90 ± 1.0	73.00 ± 0.3
AA (10)	65	3.00 ± 0.00	59.90 ± 0.4	61.45 ± 2.1
HEA (10)	65	5.92 ± 0.01	56.67 ± 2.0	58.49 ± 1.4
DMAEMA (10)	65	9.79 ± 0.06	62.19 ± 0.3	65.57 ± 3.2
PEG-DA (10)	65	3.59 ± 0.02	62.46 ± 1.1	62.61 ± 1.0
PAA (10)	65	4.57 ± 0.01	61.62 ± 0.2	70.97 ± 0.2

Table B1: Summary of swelling ratio and diffusion tests of 25wt% F127-DMA formulations. (N = 3)

APPENDIX C

Mechanochromic Composite Elastomers for Additive Manufacturing and Low Strain Mechanophore Activation

General Procedures:

1. **Synthetic Procedures:** Lab general solvents (dichloromethane, chloroform, hexane, ethyl acetate, acetone, xylene, tetrahydrofuran, ethanol) were purchased from VMR or Sigma Aldrich. Tween 20 and polyvinyl alcohol (Mowiol 18-88) were purchased from Sigma Aldrich. Sylgard®184 was purchased from Ellsworth Adhesives, Germantown, WI. Dragon Skin® 30 was purchased from Smooth-On. Flash chromatography was performed on CombiFlash®200 auto-column system from Teledyne ISCO.

A. Synthesis of Spiropyran

Spiropyran was synthesized according to a previously reported procedure[1].

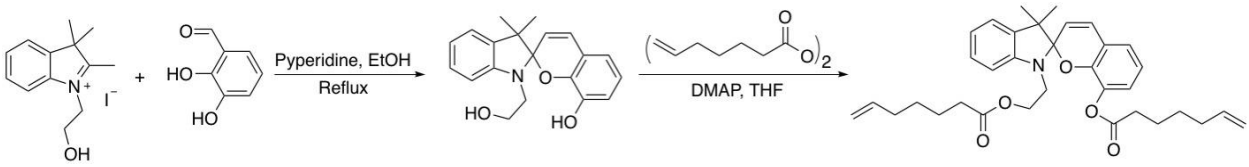

Figure C1: Scheme S1 - Synthetic scheme of spiropyran-diene.

2. **Molecular Characterizations:** Spiropyran was characterized on ^{1}H NMR spectra were collected on a 400 MHz Varian INOVA spectrometer and ^{13}C NMR spectra were collected on a 500 MHz Varian UNITY spectrometer.

3. **Tensile Testing**: Uniaxial tensile tests were performed on all specimens on a TA Instruments RSA III Dynamic Mechanical Analyzer (Force resolution: 1nm, strain resolution: 1nm) at Duke University's Shared Material Instrument Facility (SMIF). Composite materials were hand extruded. Dragon Skin films were cut to the approximate dimensions of the extruded material. To

avoid slipping and to prevent force concentrating at clamp site, two pieces of thin PDMS film were placed between the specimen and clamp on both sides of the specimen.

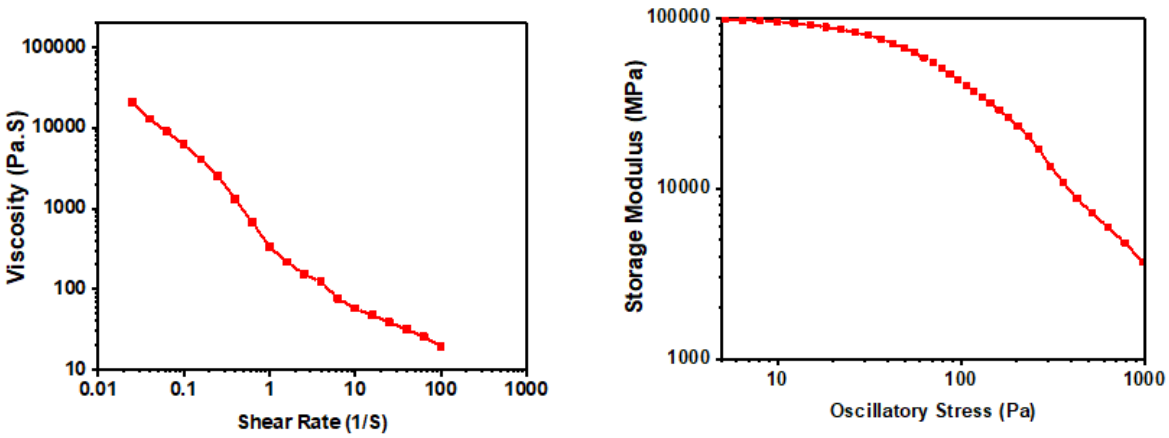

Figure C2: Rheometrical characterization of mechanochromic ink (a) Viscosity versus shear rate experiment to demonstrate shear thinning nature of the ink. (b) Oscillatory stress ramp experiment demonstrating the yield stress behavior.

Determining Mechanochromic Onset:

We first attempted to determine SP activation by taking images with a Canon EOS Rebel XSi camera at random intervals during a continuous quasi-static uniaxial tensile experiment. The image was white balanced with a color card before being imported in Fiji/ImageJ. A region of interest (ROI) was selected and its approximate position was maintained across all images and color channels. The results from the experiment suggested strain-dependent diffraction (Figure – C2). This was confirmed by repeating the procedure in analyzing color onset in composite materials without SP (Figure – C3).

"Zero-Percent" Strain Test:

The previously described experiment was modified to reduce diffraction interference. Instead of continuously straining the specimens until failure, the was stretched to the strain of interest and an image was captured with Canon EOS Rebel XSi. This image was used to confirm strains. The specimen was immediately returned to zero percent strain and another image was taken (Figures C4-C6) . An ROI was selected from the image taken at zero-percent strain and

maintained across all color channels and zero strain images. Color ratios were measured from these ROIs with the method described above. The strains measured from the previous image correspond to the B/G measured in zero-strain image that followed (Figure C7). This modified experiment produced data more similar to previously measured mechanochromic onset data from our group[1-3].

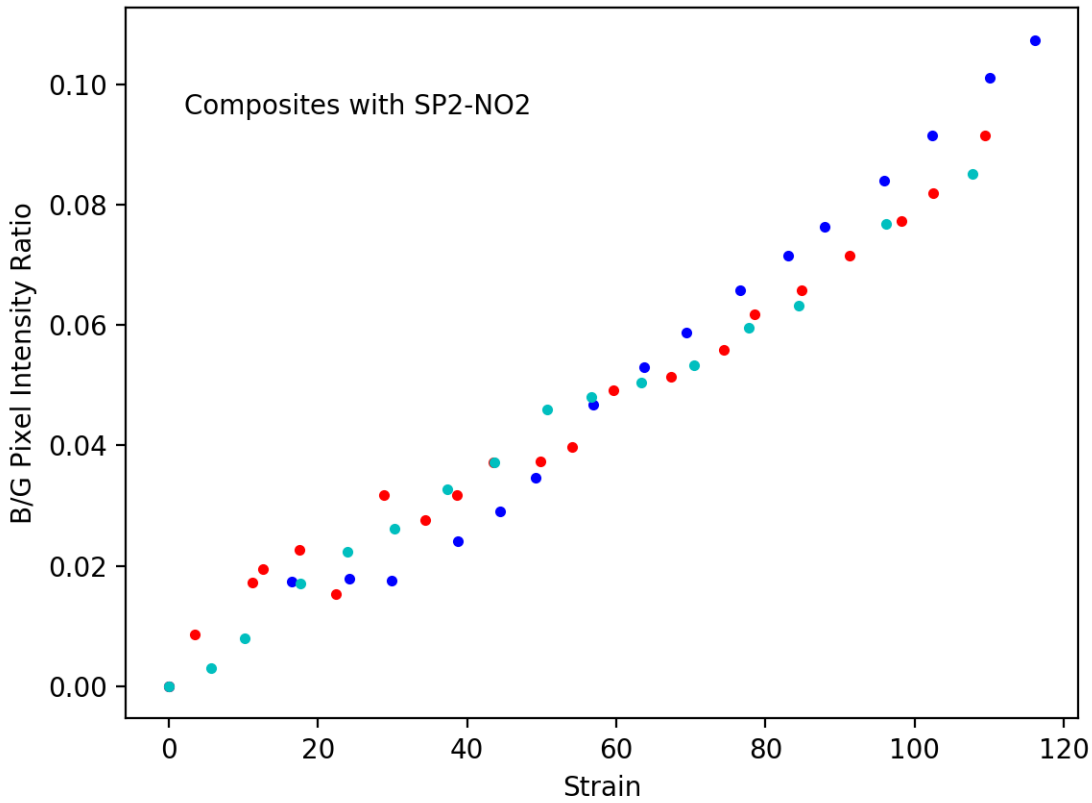

Figure C3: Results from continuous uniaxial tension tensile experiment of extruded composite materials containing SP. The ratio of the intensities of the blue channel to the green channels are plotted above.

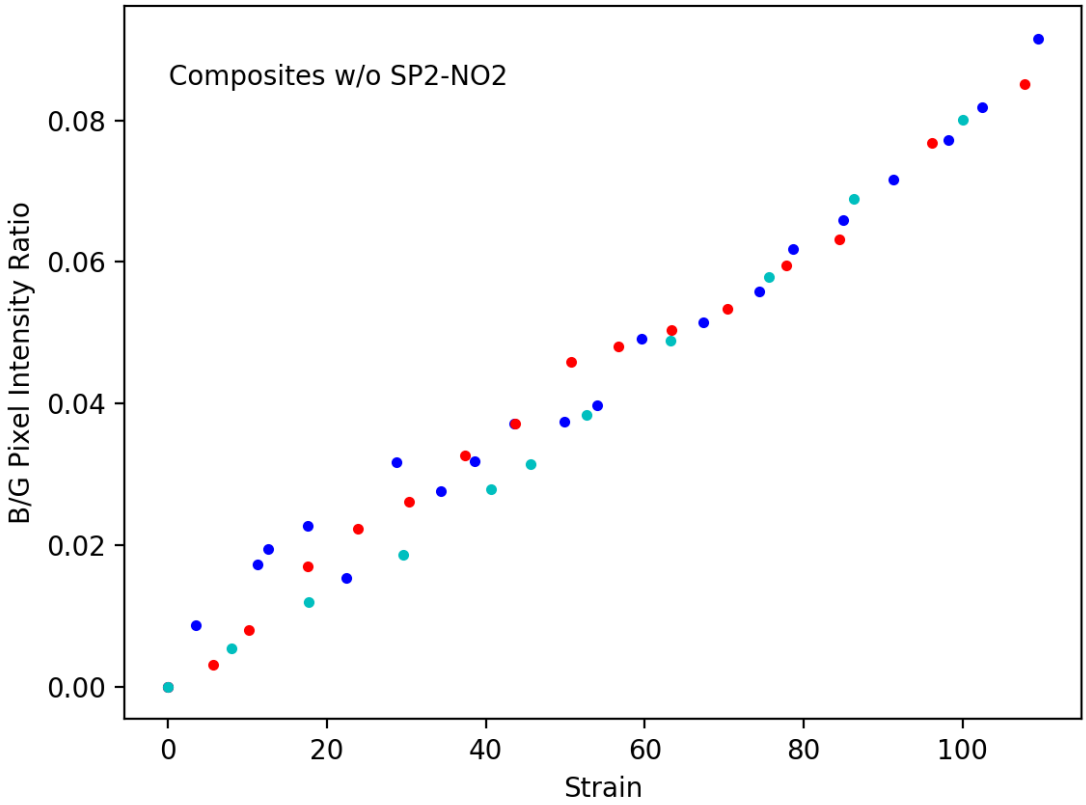

Figure C4: Three extruded composite material without mechanophore. Images were taken at random intervals during continuous quasi-static uniaxial tensile test.

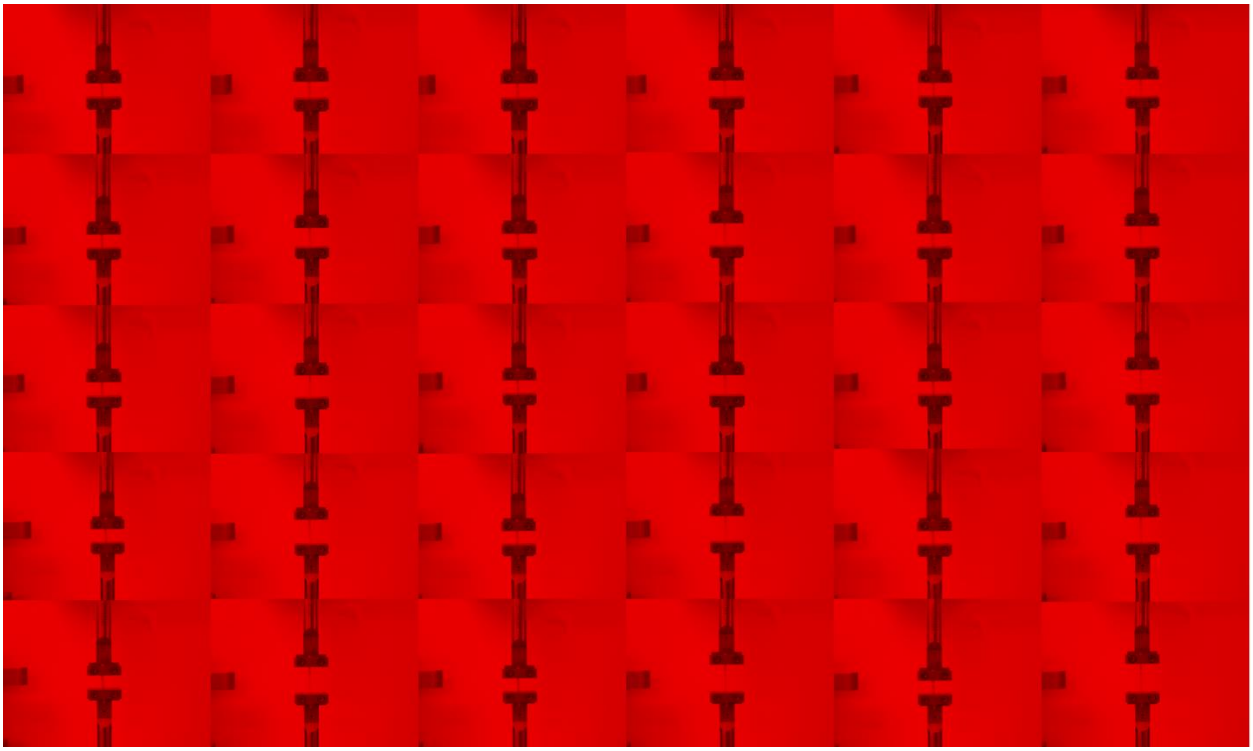

Figure C5: Representative image montage of extruded composite material during the zero-strain experiment in the red channel.

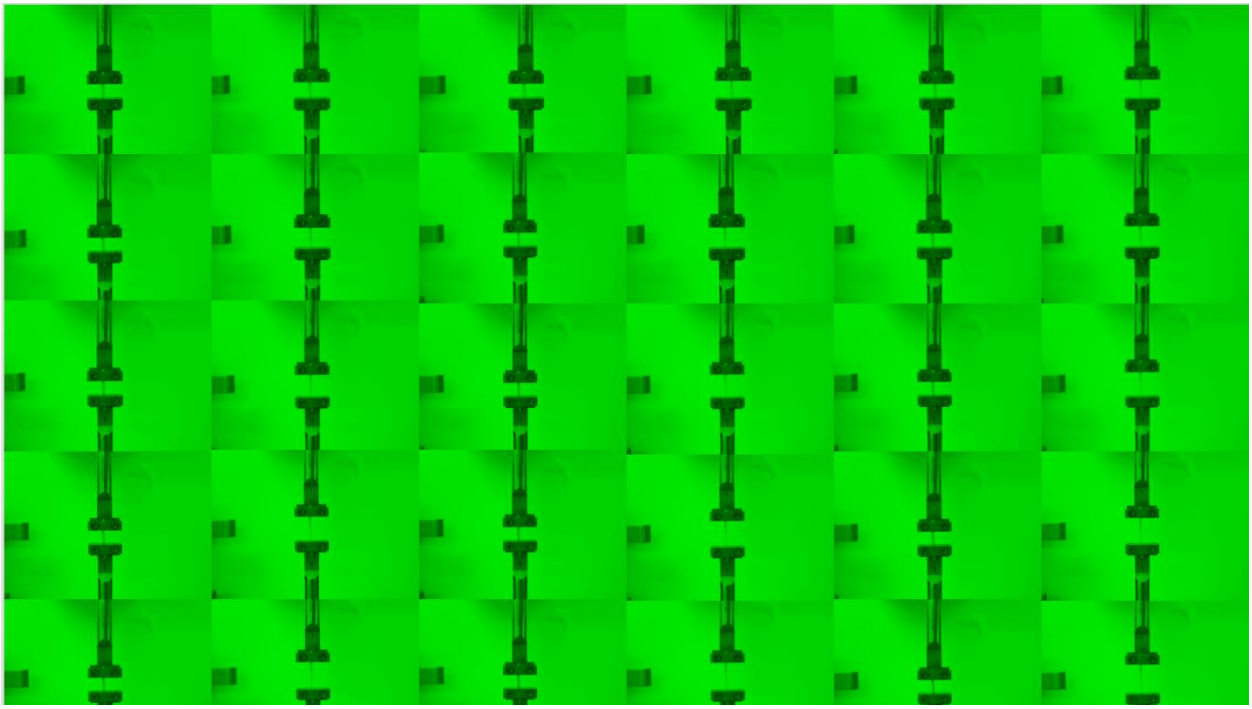

Figure C6: Representative image montage of extruded composite material during the zero-strain experiment in the green channel.

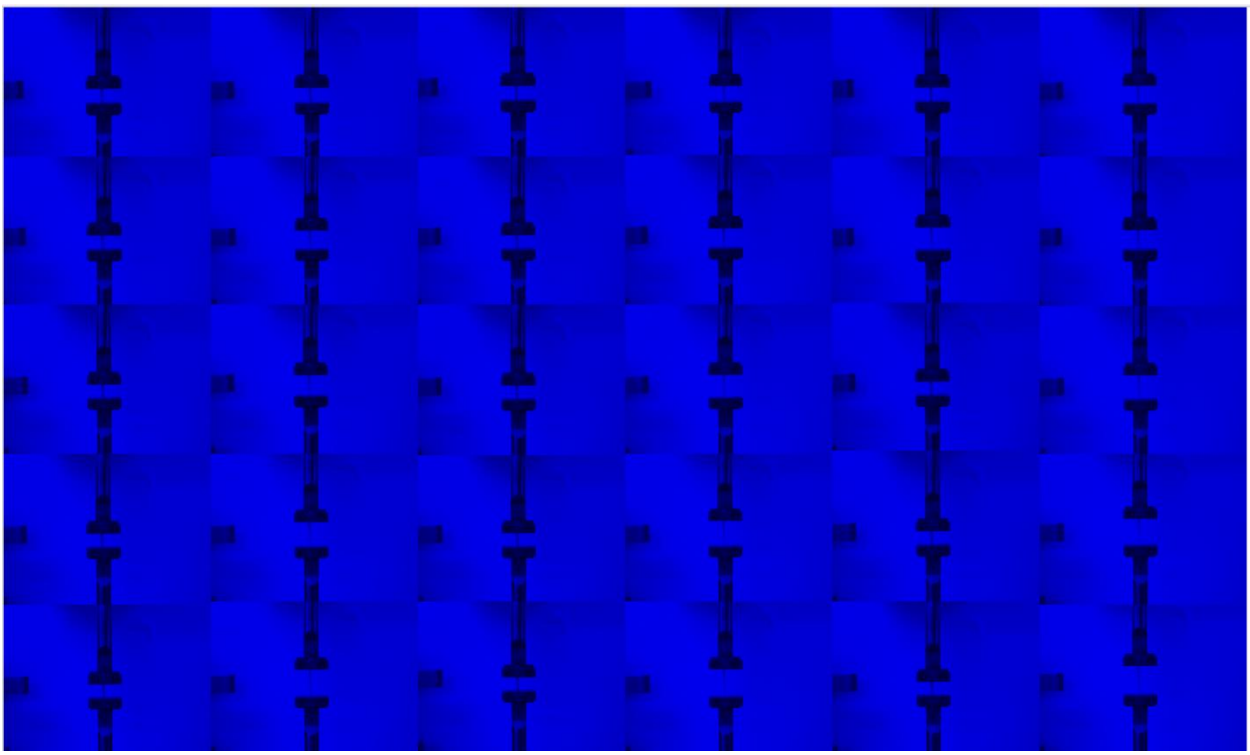

Figure C7: Representative image montage of extruded composite material during the zero-strain experiment in the blue channel.

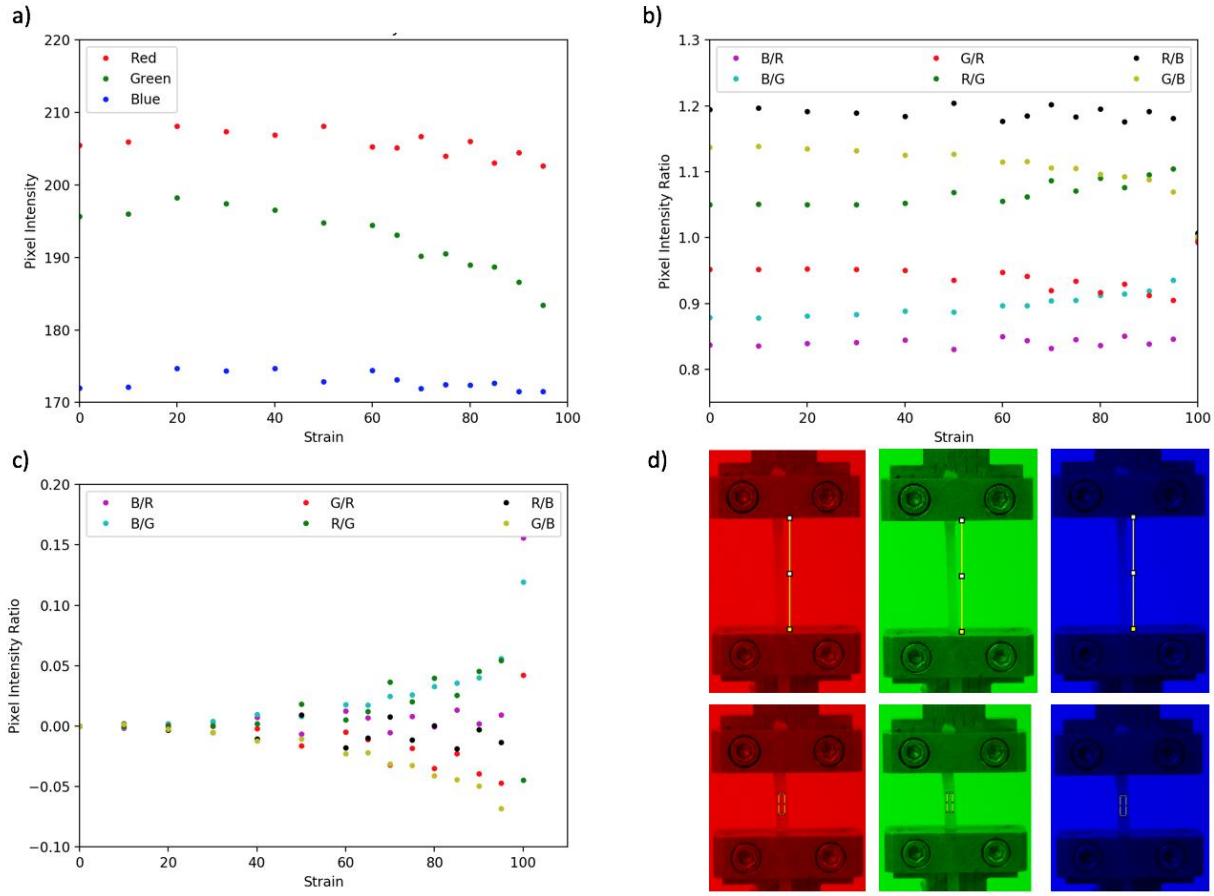

Figure C8: Change in channels as a function of strain. (a) Raw pixel intensities at red, green and blue channels; (b) All possible pixel intensity ratios; (c) All normalized pixel intensity ratios (e.g. $B/G_{ratio} - B/G_{initial}$) (d) Representative image of ImageJ analysis. Strains were determined by the pixel length of strained composite and intensities were taken from rectangular ROI of the corresponding zero-percent strain in red, green and blue channels.

Strain	*R*	*G*	*B*
0	205.486	195.646	172.022
10	205.941	196.006	172.102
20	208.120	198.212	174.683
30	207.357	197.388	174.338
40	206.895	196.572	174.726
50	208.119	194.753	172.857
60	205.262	194.451	174.427
65	205.148	193.104	173.129
70	206.671	190.164	171.927
75	204.000	190.520	172.435
80	206.005	188.973	172.391
85	203.040	188.728	172.685
90	204.423	186.591	171.529
95	202.624	183.400	171.520
100	226.180	224.928	224.562

Table C1: Representative red (R), green (G) and blue (B) pixel intensities at various strains.

Strain	*B/R*	*B/G*	*G/R*	*R/G*	*R/B*	*G/B*
0	0.837147	0.879251	0.952114	1.05029	1.19453	1.13733
10	0.835686	0.878045	0.951758	1.05069	1.19662	1.13889
20	0.839338	0.881294	0.952393	1.04999	1.19142	1.13470
30	0.840763	0.883225	0.951923	1.05050	1.18940	1.13221
40	0.844515	0.888865	0.950105	1.05252	1.18411	1.12503
50	0.830568	0.887570	0.935777	1.06863	1.20400	1.12667
60	0.849777	0.897023	0.947331	1.05560	1.17678	1.11480
65	0.843922	0.896558	0.941291	1.06237	1.18494	1.11538
70	0.831887	0.904099	0.920129	1.08680	1.20209	1.10607
75	0.845270	0.905076	0.933922	1.07075	1.18305	1.10488
80	0.836829	0.912252	0.917322	1.09013	1.19499	1.09619
85	0.850497	0.914994	0.929511	1.07583	1.17578	1.09290
90	0.839089	0.919278	0.912769	1.09557	1.19177	1.08781
95	0.846494	0.935224	0.905125	1.10482	1.18134	1.06926
100	0.992846	0.998373	0.994465	1.00557	1.00721	1.00163

Table C2: All pixel intensity ratios from representative specimen at various strains.

Strain	*D B/R*	*D B/G*	*D G/R*	*D R/G*	*D R/B*	*D G/B*
0	0.000000	0.000000	0.000000	0.00000	0.00000	0.00000
10	-0.001461	-0.001207	-0.000355	0.00039	0.00209	0.00156
20	0.002191	0.002042	0.000279	-0.00031	-0.00312	-0.00264
30	0.003615	0.003974	-0.000190	0.00021	-0.00514	-0.00512
40	0.007368	0.009614	-0.002008	0.00222	-0.01042	-0.01230
50	-0.006579	0.008319	-0.016336	0.01834	0.00946	-0.01066
60	0.012630	0.017772	-0.004783	0.00530	-0.01775	-0.02253
65	0.006775	0.017307	-0.010822	0.01208	-0.00959	-0.02195
70	-0.005260	0.024847	-0.031984	0.03651	0.00755	-0.03126
75	0.008123	0.025824	-0.018192	0.02046	-0.01148	-0.03245
80	-0.000318	0.033001	-0.034791	0.03983	0.00045	-0.04114
85	0.013350	0.035743	-0.022602	0.02554	-0.01875	-0.04443
90	0.001942	0.040027	-0.039344	0.04527	-0.00276	-0.04952
95	0.009347	0.055972	-0.046989	0.05453	-0.01319	-0.06807
100	0.155699	0.119122	0.042351	-0.04473	-0.18733	-0.13570

Table C3: All normalized pixel intensity ratio (e.g. $B/R_{ratio} - B/R_{initial}$) for a representative specimen.

Strain	*Test 1*	*Test 2*	*Test 3*	*Test 4*	*Test 5*	*Average*
0	0.00000	0.00000	0.00000	0.00000	0.00000	0.00000
10	-0.00121	0.00345	-0.00085	-0.00398	0.00057	-0.00040
20	0.00204	0.00228	-0.00222	-0.00010	-0.00200	0.00000
30	0.00397	0.00901	-0.00120	0.00064	-0.00154	0.00218
40	0.00961	0.00886	0.00304	0.00176	0.00008	0.00467
50	0.00832	0.01251	0.00522	0.00141	0.00242	0.00598
60	0.01777	0.01811	0.01452	0.00279	0.00155	0.01095
65	0.01731	0.02204	0.01875	0.01151	0.00597	0.01512
70	0.02485	0.02102	0.02191	0.01452	0.00538	0.01754
75	0.02582	0.03171	0.02664	0.01944	0.02747	0.02622
80	0.03300	0.03320	0.04799	0.02186	0.01465	0.03014
85	0.03574	0.03923	0.05015	0.02361	0.01955	0.03366
90	0.04003	0.04420	0.04697	0.02178	0.01855	0.03431

Table C4: Normalized B/G pixel intensity ratios for all tested specimens.

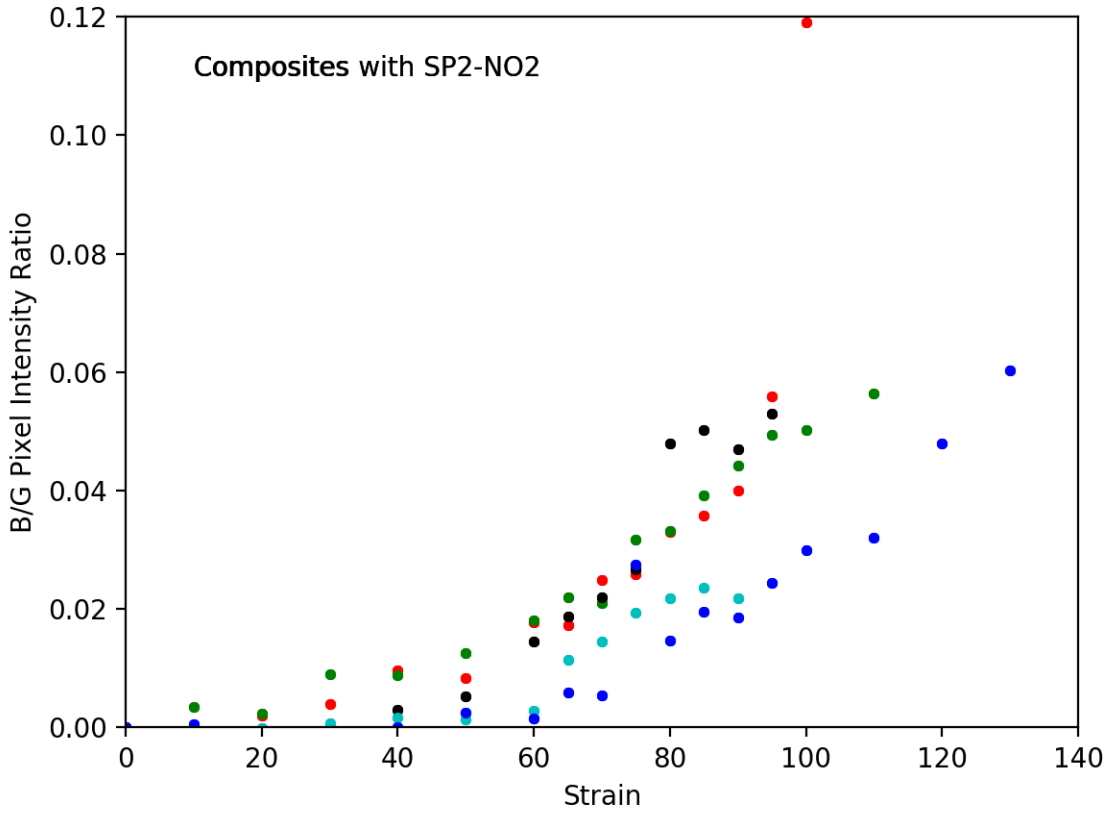

Figure C9: Figure of normalized B/G pixel intensity ratio for all tested specimens

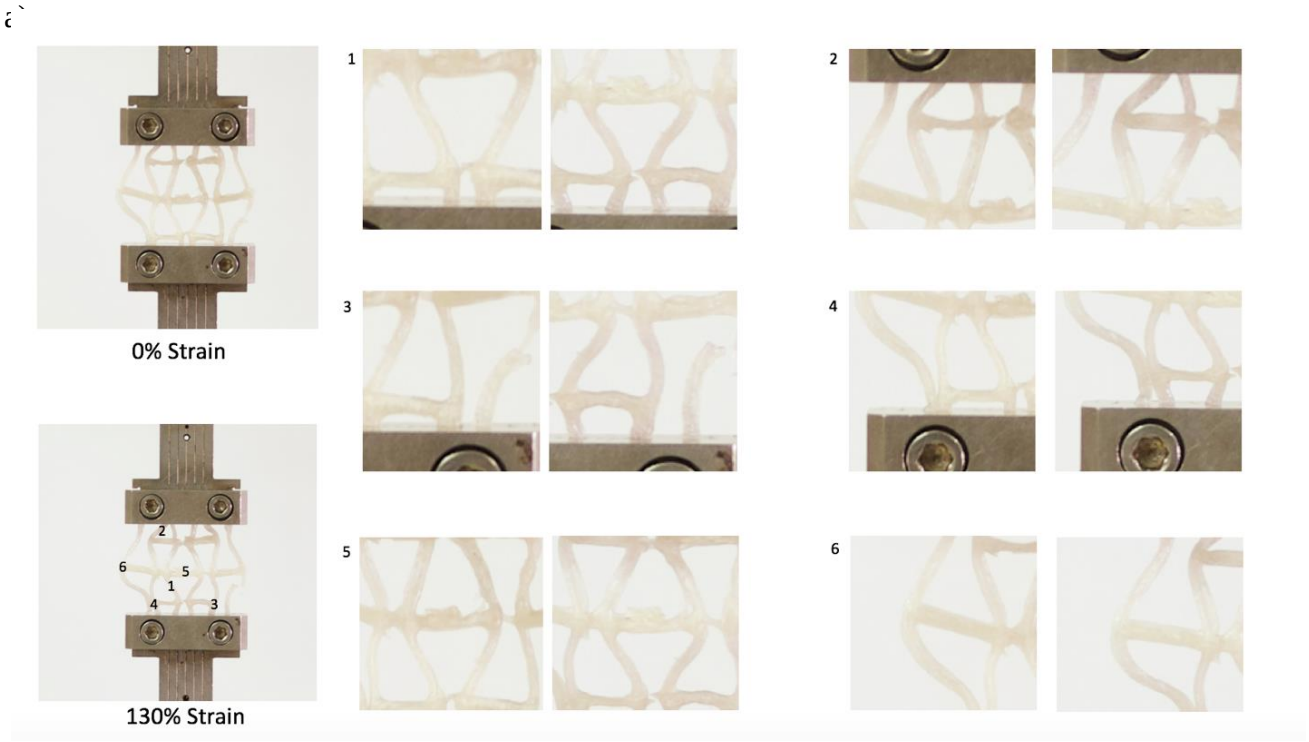

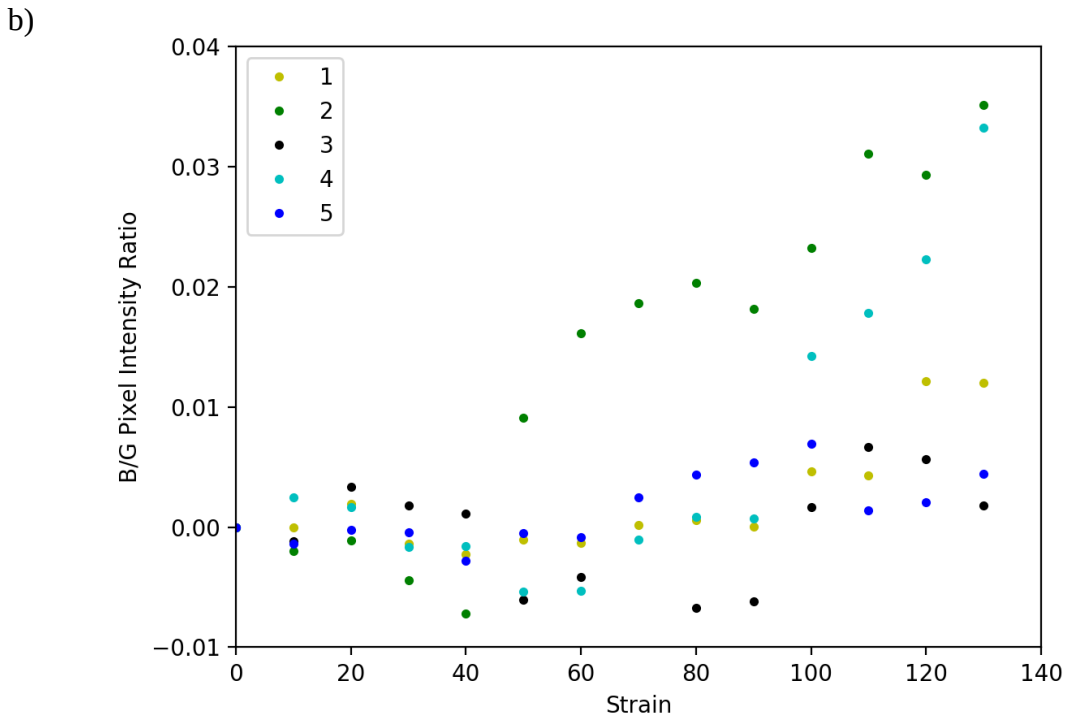

Figure C10: 3D printed mesh like structures showing activation under tensile forces. (a) pictures of regionalized activation in mesh structures. (b) B/G Pixel intensity Ratio of areas selected above. Mechanochromic activation appears to be most significant in areas close to the clamp.

APPENDIX D

Dual mechano-activated multi-material 4D printing of shape morphing objects

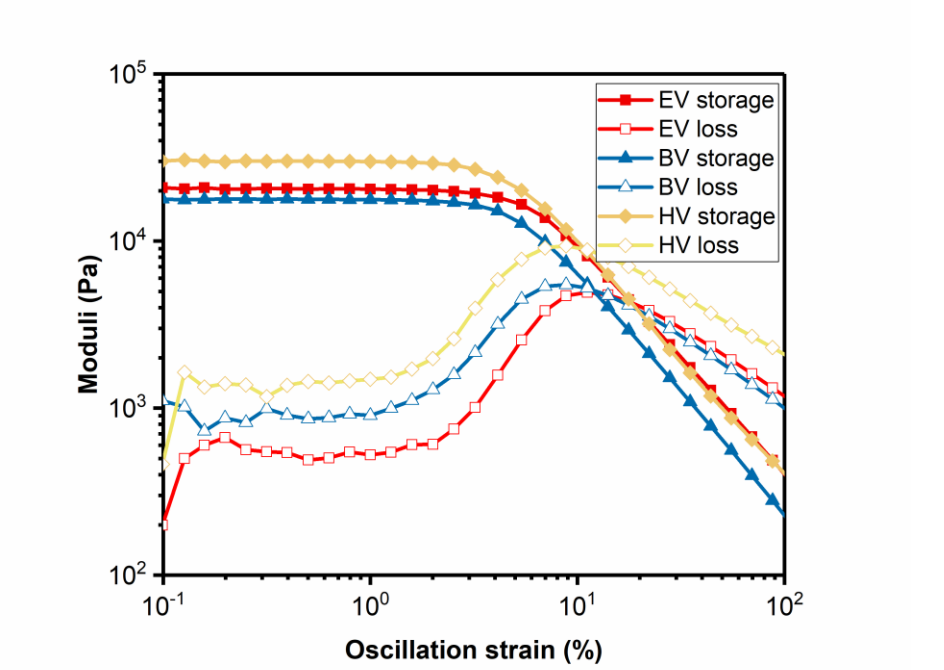

Figure D1: Oscillatory shear stress experiment for [EVIM]BF_4, [BVIM]BF_4 and [HVIM]BF_4 iongels

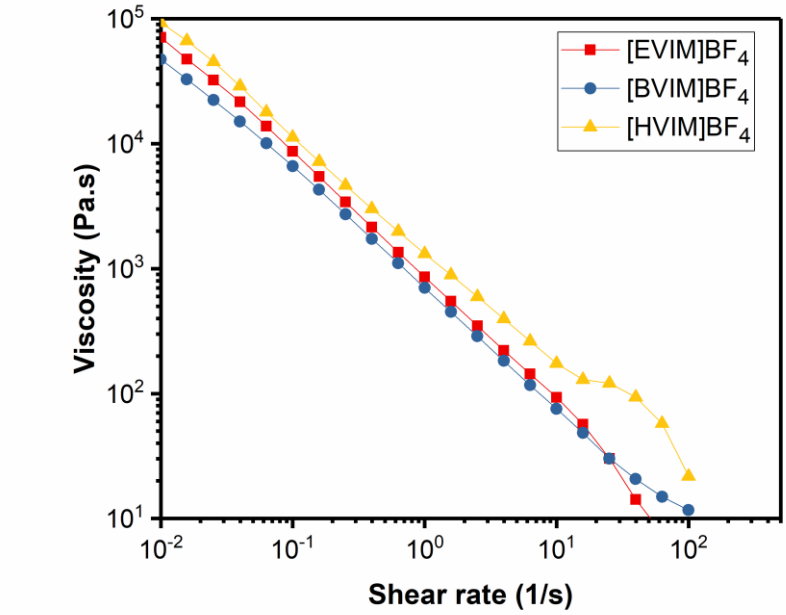

Figure D2: Viscosity vs. shear rate for $[EVIM]BF_4$, $[BVIM]BF_4$ and $[HVIM]BF_4$ iongels

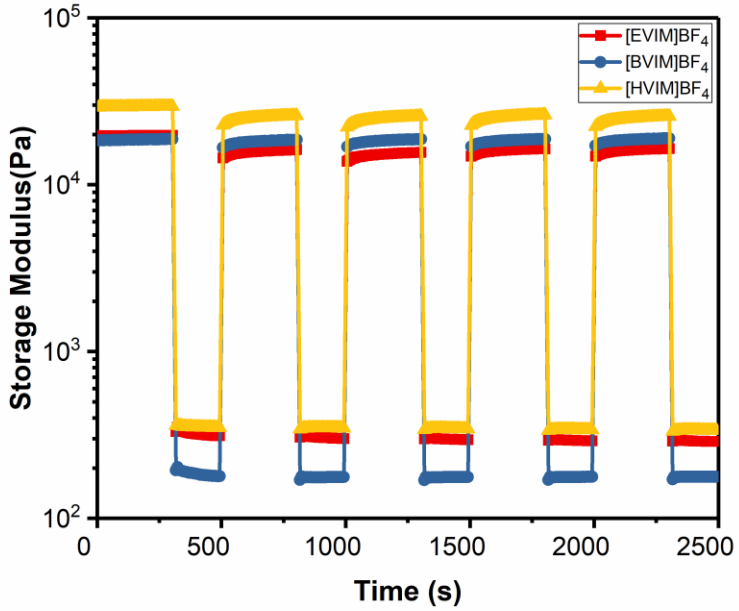

Figure D3: Cyclic strain experiments for [EVIM]BF_4, [BVIM]BF_4 and [HVIM]BF_4 iongels

NAME	Concentration of F127-BUM (Wt %)	Concentration of F127 (Wt %)	YOUNG'S MODULUS (MPa)	TOUGHNESS (J/m3)*10^3	ELONGATION (%)	ACTIVATION (%)
[EVIM]BF_4	10	20	490.75	3.07	350	50
	20	10	530.66	3.15		
	30	0	579.10	3.76		
[BVIM]BF_4	10	20	98.02	2.62	450	130
	20	10	106.55	2.77		
	30	0	102.65	2.86		
[HVIM]BF_4	17	20	44.54	0.86	480	180
	27	10	34.65	0.89		
	37	0	71.44	1.67		

Table D1: Mechanical properties under quasi-static uniaxial tensile strain of all iongel formulations

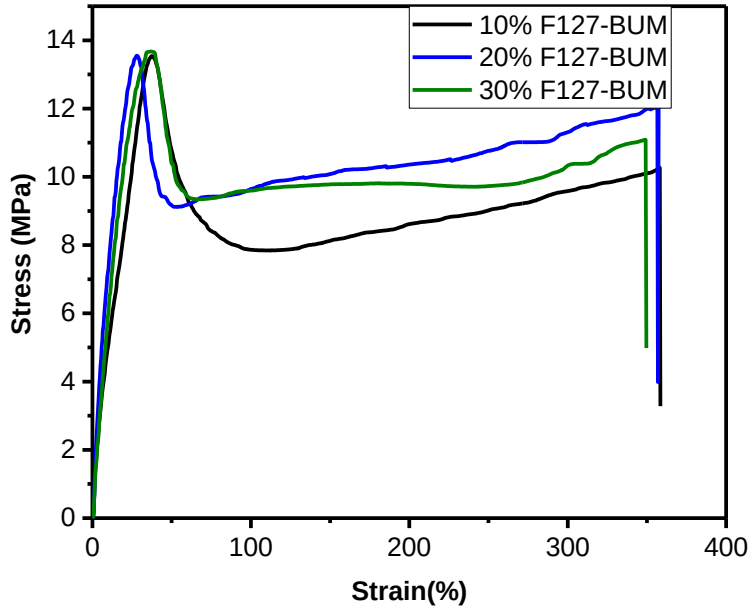

Figure D4: Mechanical properties of [EVIM]BF_4 iongels with different crosslinker concentrations

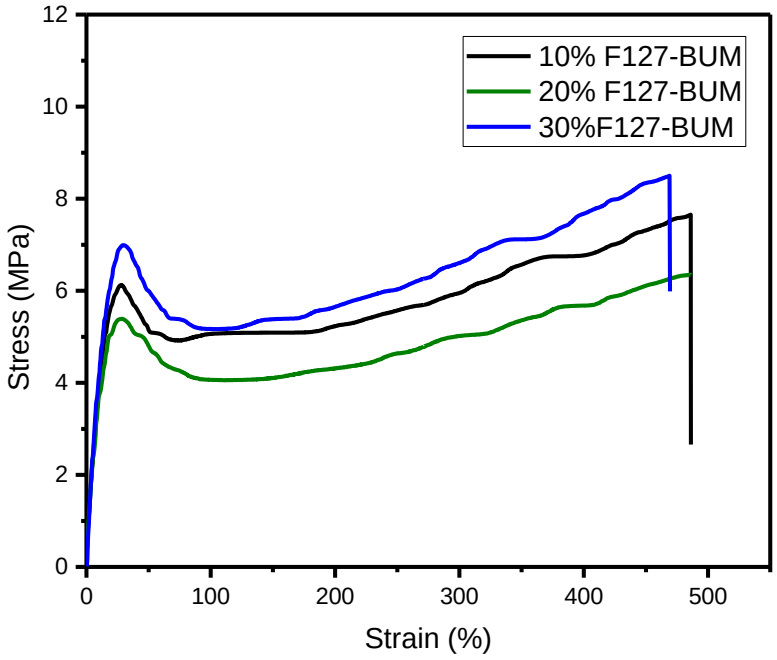

Figure D5: Mechanical properties of [BVIM]BF_4 iongels with different crosslinker concentrations

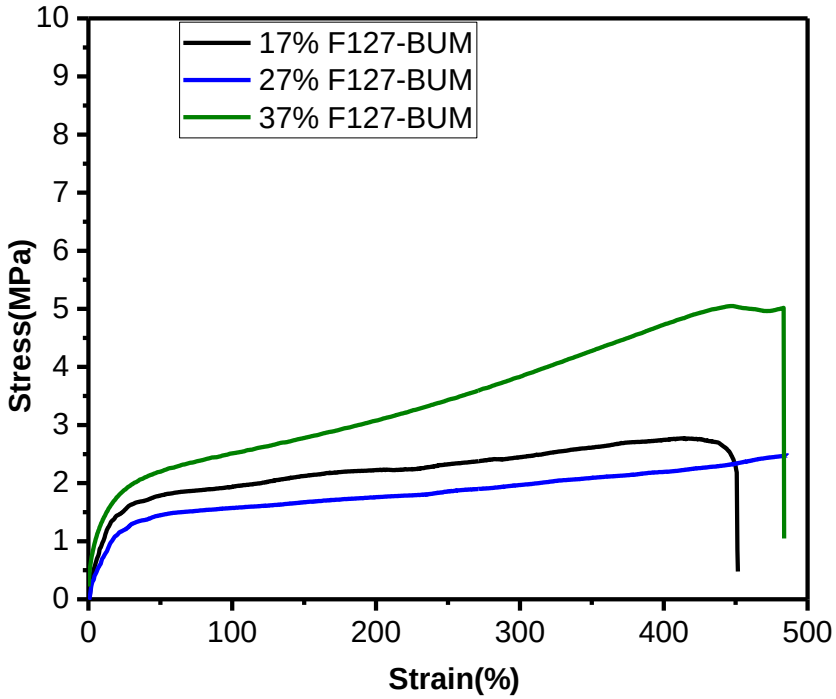

Figure D6: Mechanical properties of [HVIM]BF_4 iongels with different crosslinker concentrations

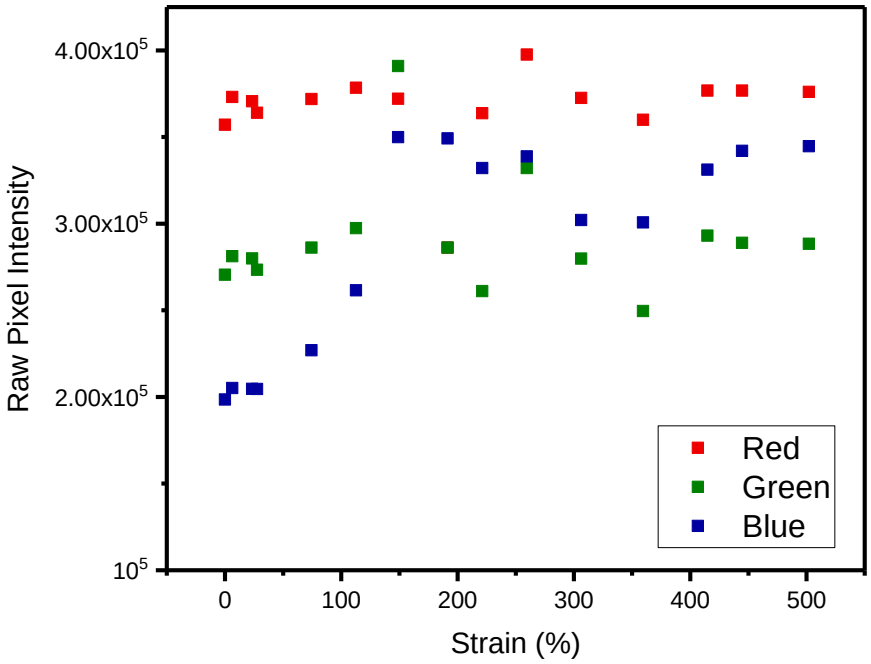

Figure D7: Change in raw pixel intensity in red, green and blue color channels as a function of strain.

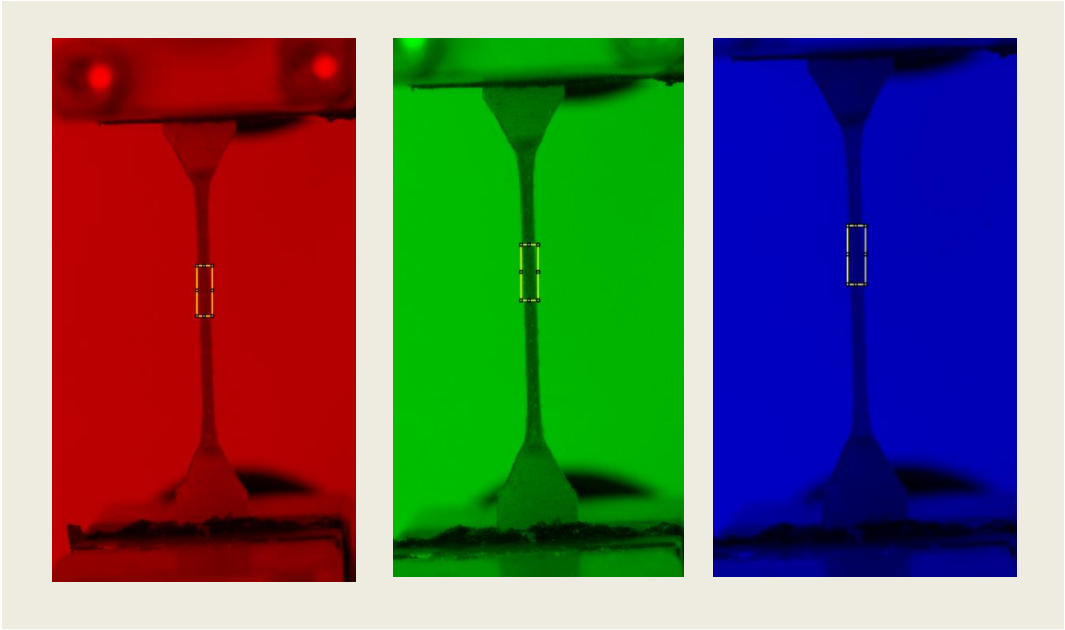

Figure D8: Representative images of samples split into red, green and blue channels when processed via ImageJ software.

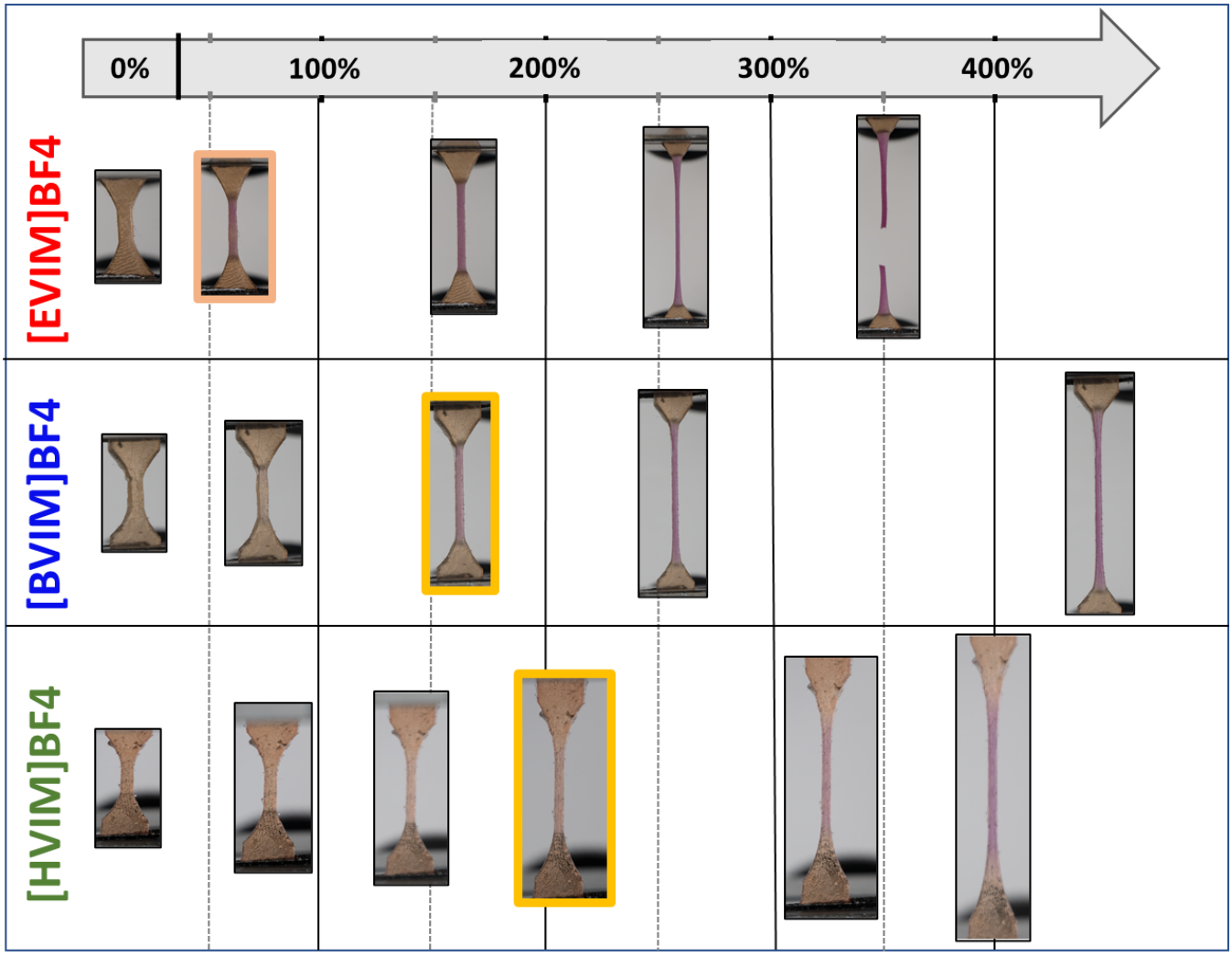

Figure D9: Onset of color activation in mechanophores embedded in iongel networks

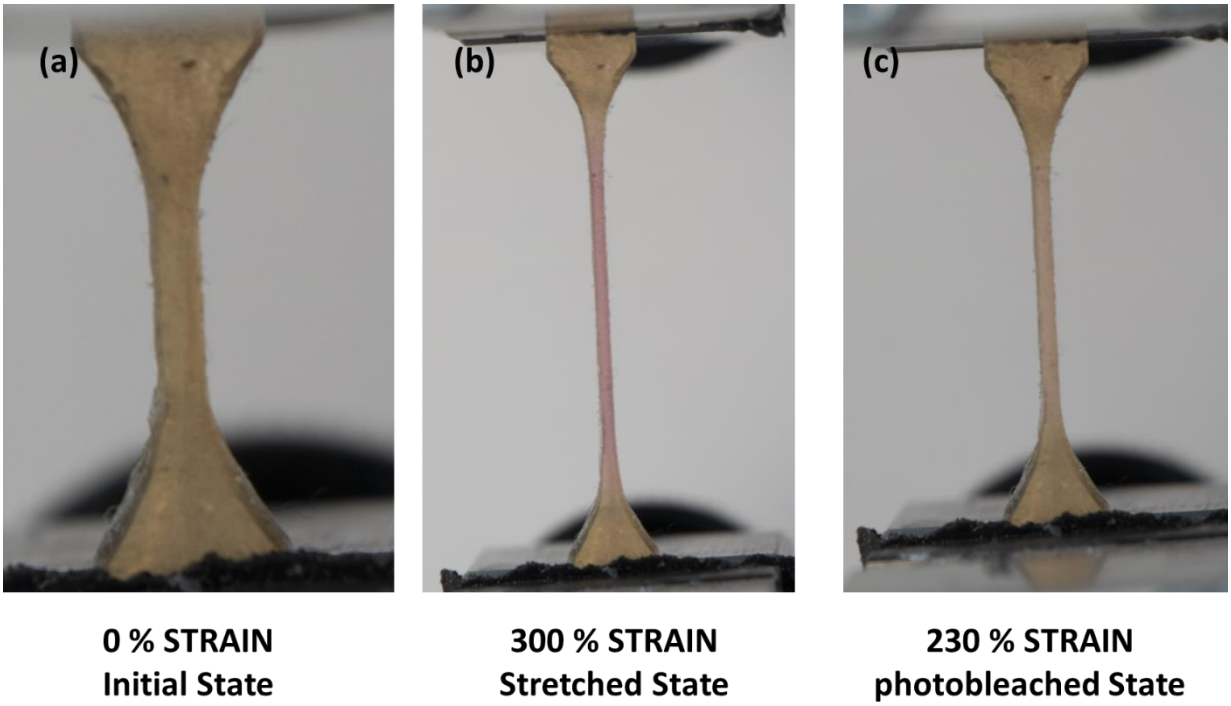

Figure D10: exemplary photos of [HVIM]BF4 iongel in different states showing the reusability of the gels for stress detection(a) original state before stretching (b) stretched to 300% strain, with mechanochromic response (c) photo-bleached and recovered state.

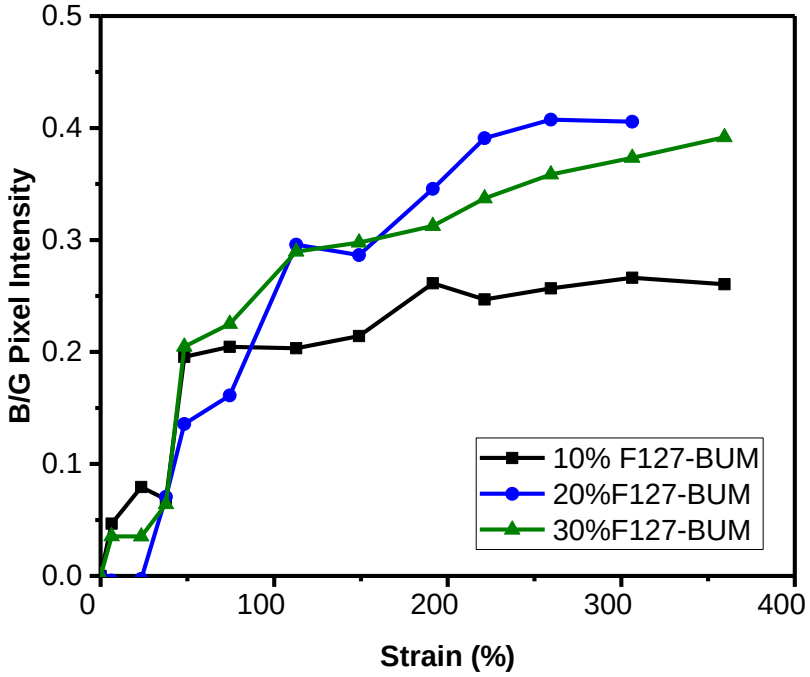

Figure D11: Onset of mechanochromic activation with varioation in concentration of primary crosslinker in [EVIM]BF_4

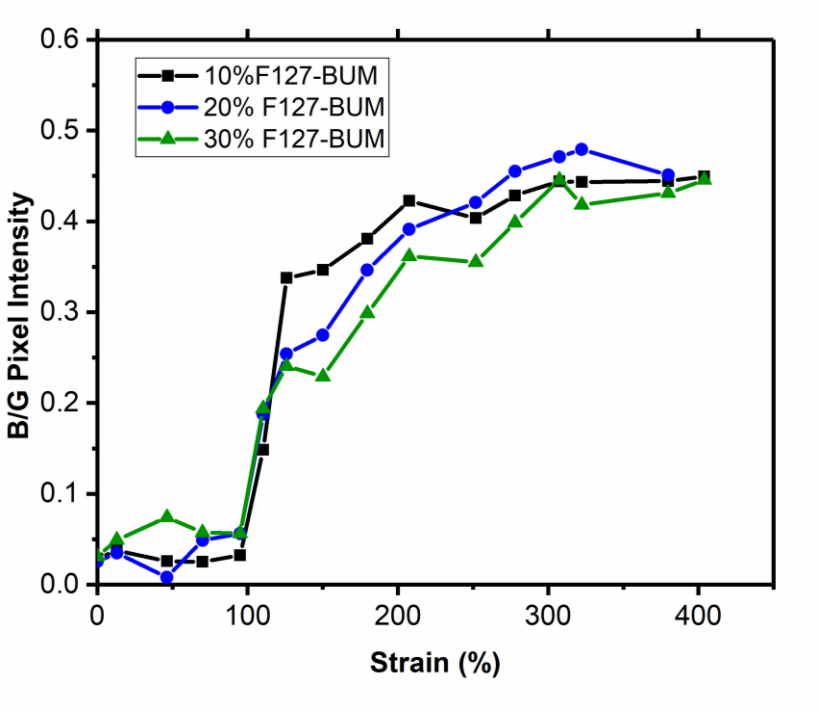

Figure D12: Onset of mechanochromic activation with varioation in concentration of primary crosslinker in [BVIM]BF_4

25%	50%	100%
35°	111.2°	167.23°

Figure D13: Bending angle when dogbone bilayers are stretched to different amounts of tensile strain

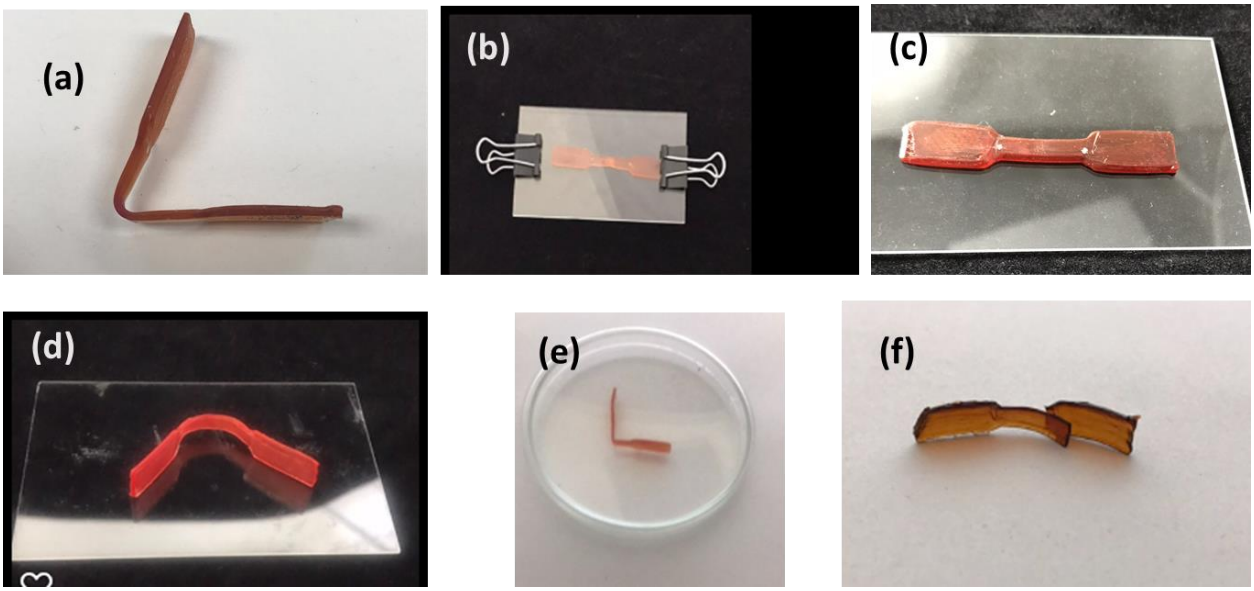

Figure D14: Thermal recovery experiment in [EVIM]BF_4/[BVIM]BF_4 bilayers: intial 'bent' sample(a) was sandwiched between two glass slides and heated for 12 h(b). After cooling to room temperature, original shape and dimension was recovered(c). A similar sample when kept at room

temperature did not undergo shape recovery(d). Intial ‘bent sample when heated in a petri-dish underwent decomposition (e) and turned brown and brittle to touch (f).

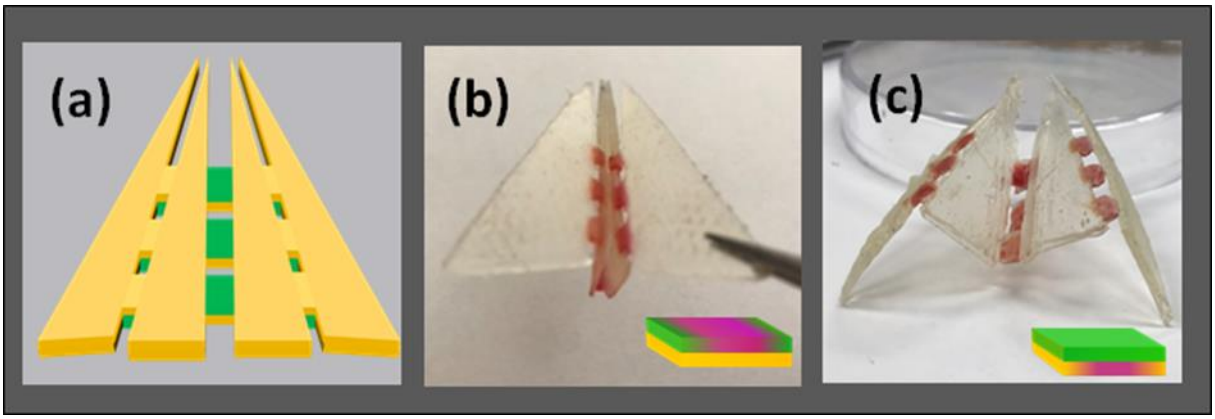

Figure D15: Design of a planar bilayer which can morph into an airplane structure. (a) cartoon representation of the structure showing different composition of bilayers at the hinges.(b) When SPDMA was incorporated in the [BVIM]BF4 layer, the structure folded into an airplane shape, while under-straining it in (c) led to a crumpled structure.

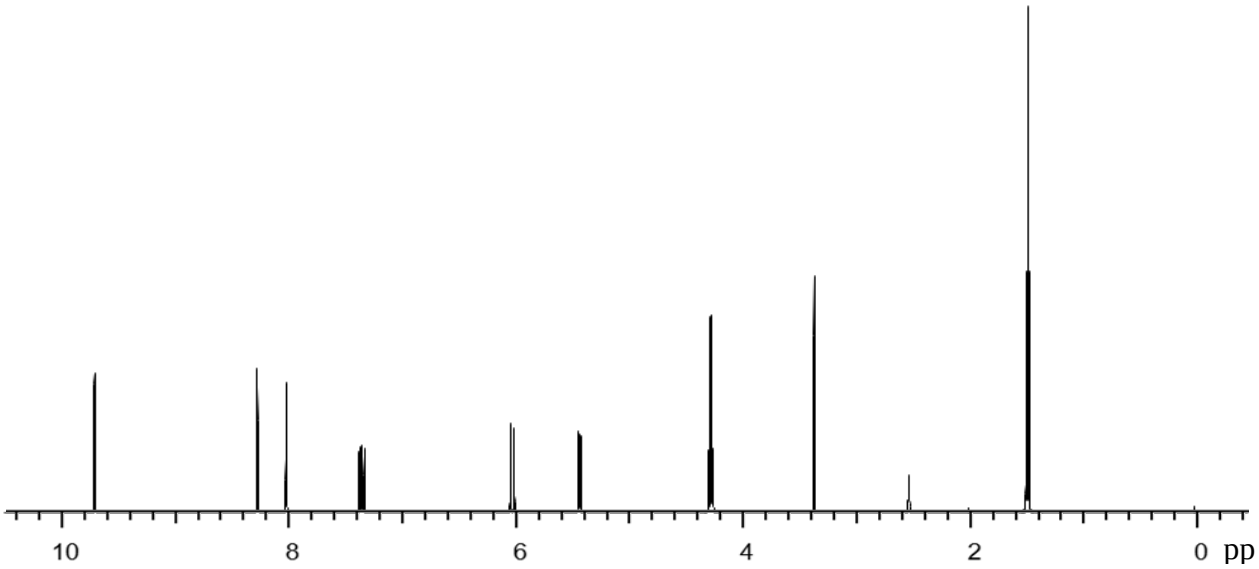

Figure D16: Synthesis of [EVIM]Br: ^{1}H NMR (500 MHz, DMSO-d_6) δ 9.67 (s, 1 H); 8.26 (t, 1 H); 8.00 (t, 1 H); 7.33 (q, 1 H); 6.00 (dd, 1 H); 5.41 (dd, 1 H); 4.25 (q, 2 H); 1.45 (t, 3 H).

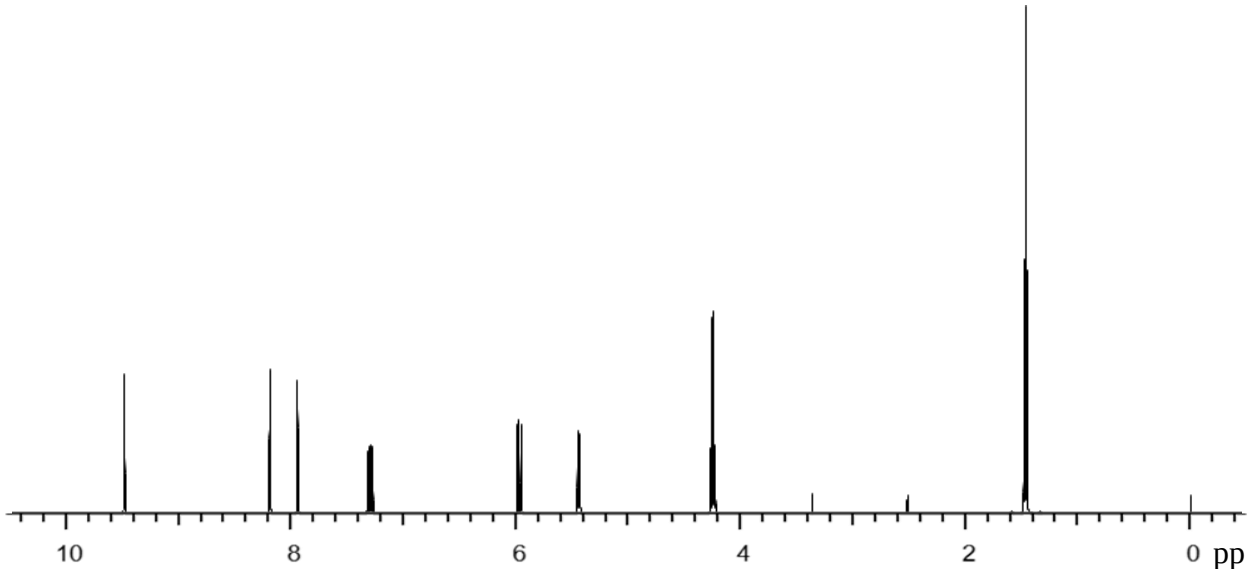

Figure D17: Synthesis of [EVIM]BF_4: ^{1}H NMR (500 MHz, DMSO-d_6) δ 9.45 (s, 1 H); 8.16 (t, 1 H); 7.91 (t, 1 H); 7.27 (q, 1 H); 5.94 (dd, 1 H); 5.41 (dd, 1 H); 4.23 (q, 2 H); 1.45 (t, 3 H).

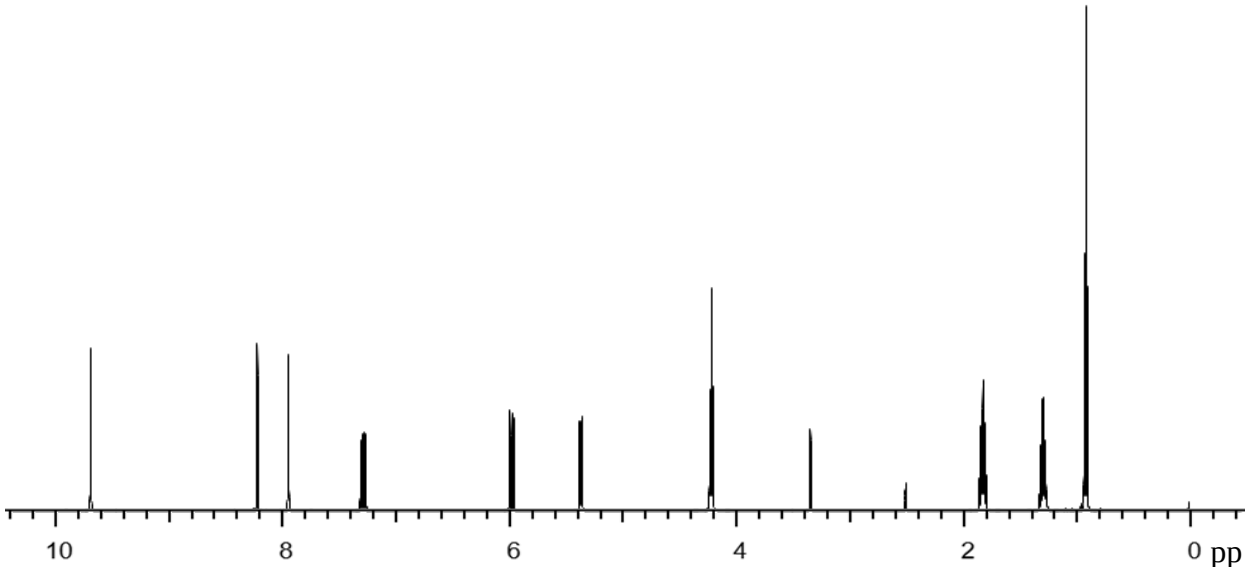

Figure D18: Synthesis of [BVIM]Br: ^{1}H NMR (500 MHz, DMSO-d_6) δ 9.80 (s, 1 H); 8.30 (t, 1 H); 8.03 (t, 1 H); 7.36 (q, 1 H); 6.03 (dd, 1 H); 5.41 (dd, 1 H); 4.24 (t, 2 H); 1.81 (quintet, 2 H); 1.27 (sextet, 2 H); 0.89 (t, 3 H).

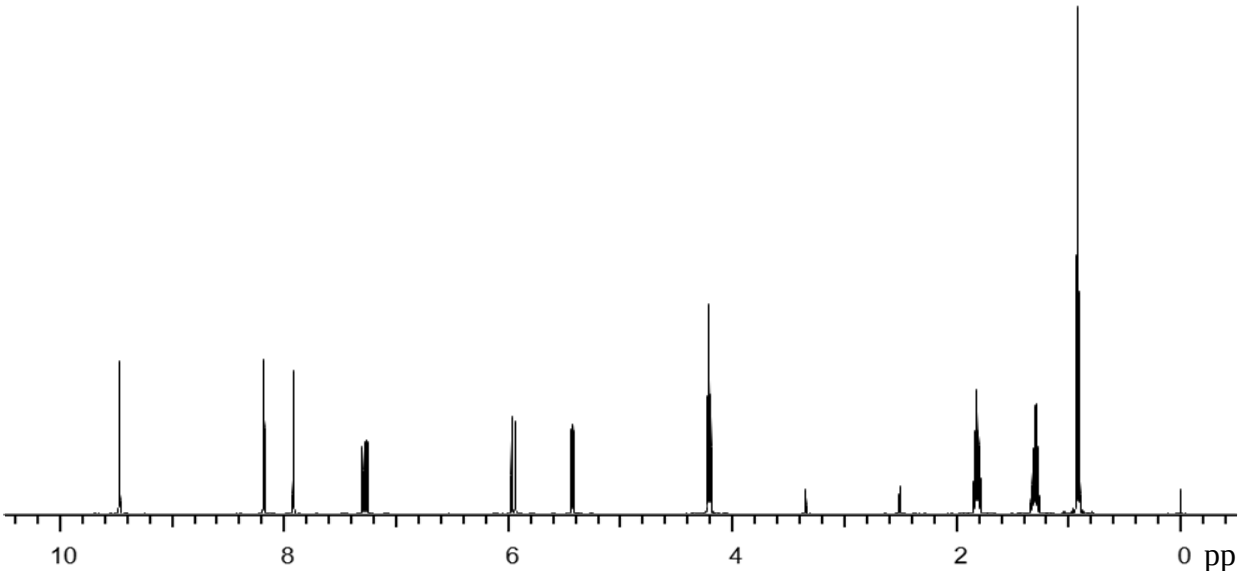

Figure D19: Synthesis of [BVIM]BF_4: ^{1}H NMR (500 MHz, DMSO-d_6) δ 9.46 (s, 1 H); 8.18 (t, 1 H); 7.91 (t, 1 H); 7.27 (q, 1 H); 5.95 (dd, 1 H); 5.42 (dd, 1 H); 4.20 (t, 2 H); 1.81 (quintet, 2 H); 1.29 (sextet, 2 H); 0.91 (t, 3 H).

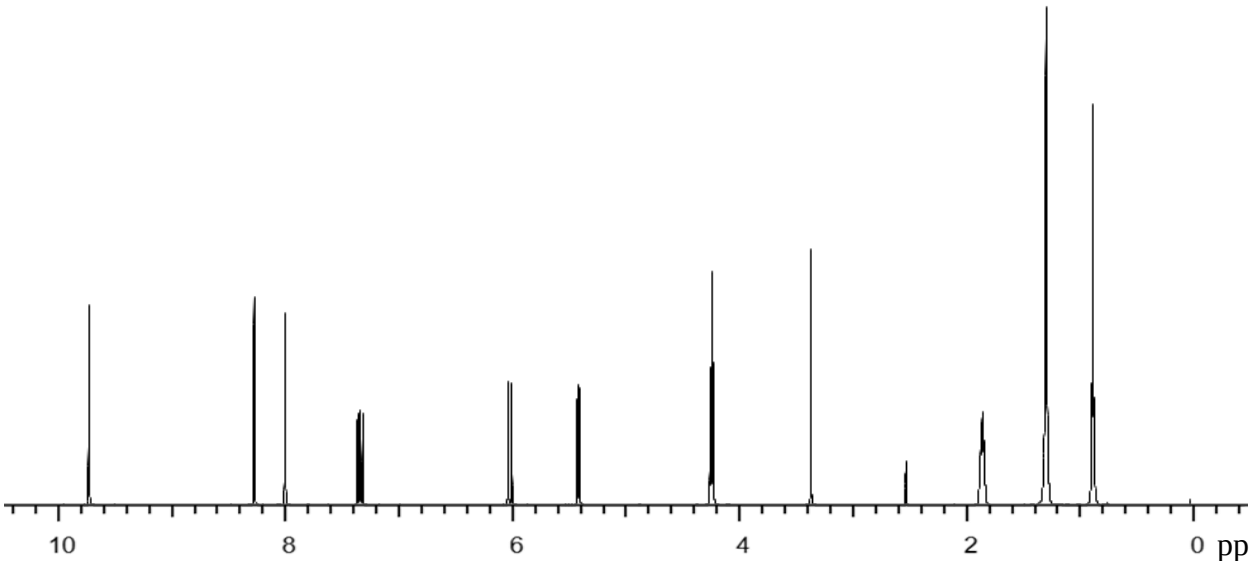

Figure D18: Synthesis of [HVIM]Br: ^{1}H NMR (500 MHz, DMSO-d_6) δ 9.76 (s, 1 H); 8.29 (t, 1 H); 8.01 (t, 1 H); 7.35 (q, 1 H); 6.02 (dd, 1 H); 5.41 (dd, 1 H); 4.22 (t, 2 H); 1.82 (quintet, 2 H); 1.26 (m, 6 H); 0.84 (t, 3 H).

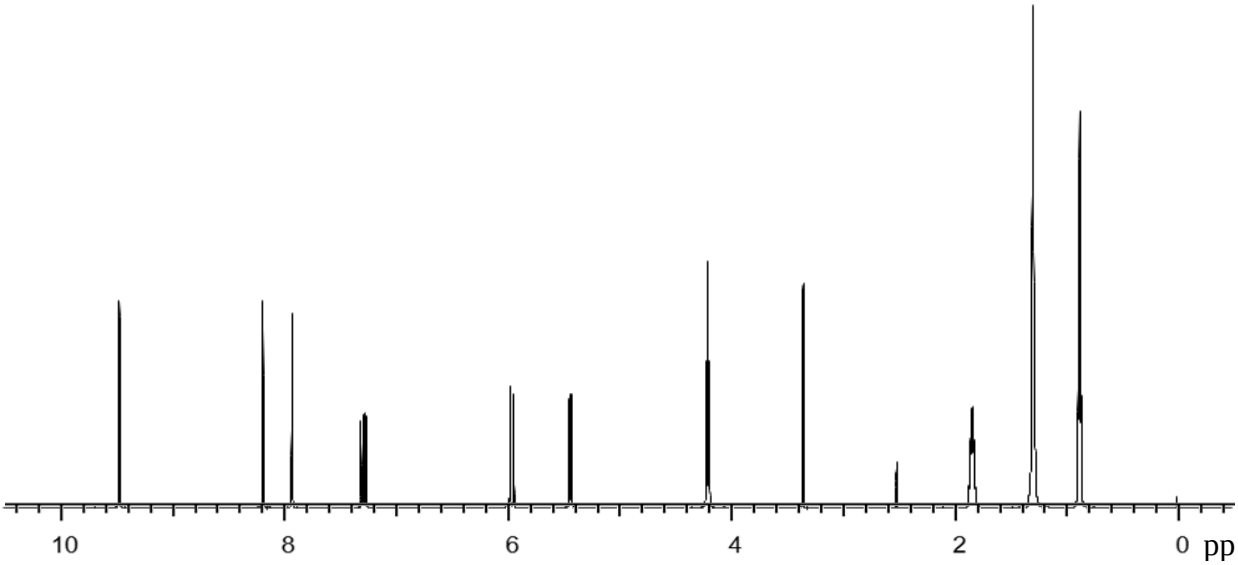

Figure D20: Synthesis of [HVIM]BF_4: ^{1}H NMR (500 MHz, DMSO-d_6) δ 9.46 (s, 1 H); 8.18 (t, 1 H); 7.92 (t, 1 H); 7.28 (q, 1 H); 5.95 (dd, 1 H); 5.42 (dd, 1 H); 4.19 (t, 2 H); 1.82 (quintet, 2 H); 1.27 (m, 6 H); 0.86 (t, 3 H).